Small Antennas Radiation Performance Optimization in Mobile Communications

Von der Fakultät für Ingenieurwissenschaften der
Universität Duisburg-Essen
zur Erlangung des akademischen Grades eines

Doktors der Ingenieurwissenschaften (Dr.-Ing.)

genehmigte Dissertation

von
Dipl.-Ing. CelestinTamgue Famdie
aus
Mbo/Kamerun

Referent:	Prof. Dr.-Ing. Klaus Solbach
Korreferent:	Prof. Dr.-Ing. Heinz Chaloupka
Tag der mündlichen Prüfung:	30. Oktober 2007

Abstract

WIRELESS COMMUNICATIONS have undergone a drastic development in the past decade and have also been an important motivator for small antenna research. Introduction of new communications systems with wider system bands, evolution from single-band to multiband standard and a significant decrease in average of the terminal size are on the roadmap of the industry. All this combined with strict limitation due to the protection of mobile devices users from radiation exposure has created needs for adequate antenna solutions and better understanding of small antennas on small complex platforms. As answer to these great challenges, a purposeful investigation of a new concept for small antennas development on small platforms is proposed in this thesis.

The performance of a small antenna mounted on a small conductive object, such as the chassis of a mobile phone is strongly affected by the size and shape of the object as well as the position of the small antenna on it. For a better understanding of the radiation properties of the radiating system constituted by a small antenna and the conductive chassis of a mobile phone device, this thesis conceptually considers the small antenna and the conductive chassis as two distinctive entities and separately investigates the radiation properties of the metal chassis. The idea here is that from the knowledge of the chassis radiation properties, one easily identifies the optimal location of the small antenna on the chassis and achieves a design of the small antenna to optimally meet some given requirements. Investigation of the conductive chassis radiation properties is based on the theory of characteristic modes.

In fact, the theory of characteristic modes is a powerful analytical concept comparable to what modal analysis represents for waveguide circuits. At a frequency of interest this concept provides an insight on the contribution of different characteristic modes in the overall chassis radiation properties, which inexorably leads to the knowledge of the dominant characteristic mode. Resonant characteristic modes which dominates the radiation properties at their respective frequencies assign their radiation properties expressed in terms of resonance frequency and radiation quality factor to the conductive chassis.

In the frame of this work, a numerical evaluation of characteristic modes on the surface of conductive chassis of mobile phones is proposed. This has been made possible through

the solution of the resulting generalized eigenvalue problem representing the radiating system and leading to characteristic modes. For the resolution of the resulting generalized eigenvalue problem, an algorithm based on the QZ-decomposition is conceived and a corresponding software is developed. As application, results on the radiation properties as well as optimal location of the small antenna (considered as an exciter or coupler) to achieve an effective coupling with the chassis is presented for generic bar-type and folder-type phones. For the latter two cases of operation have been distinguished: the closed and open states.

A simplified version of the theory of characteristic modes for the analysis of chassis radiation properties is presented in this thesis. It is based on the far-field radiation properties of a small radiator in free-space. The radiation vector is approximated by moments of different orders depending on the shape of the chassis. This practical approach operates by post-processing output data from standard commercial electromagnetic softwares. The purposeful utilization and the tuning of chassis modes for the design of multiband radiation characteristics on generic bar-type and folder-type geometries is demonstrated.

Acknowledgments

THIS work is the result of my activities in the former company Siemens Mobile and later BenQ Mobile, where I spent more than two and half years. Its theoretical and experimental aspects required the assistance of academical experts and this initiated and led to a cooperation with the department of Microwave and RF-Technology of the University of Duisburg-Essen.
Such an achievement is the fruit of combined efforts of people at different levels, whose contributions have directly or indirectly, negatively or positively affected this work. It is not appropriate to provide details about people from the first category.
Nevertheless I'll like to use this opportunity to express my deepest gratitude to my mother and to the memory of my late father for being who they are and for the great job they did in supporting my education. This work shows that your efforts have not been vain !

The first and foremost person from the second category is my supervisor Dr. Werner L. Schröder. He was the one who hooked me in the area of small antennas and guided my first steps in the difficult and fascinating world of research. His enlightening advice, generous support and unconditional availability have accompagnied me all along from the early stage of this work based on the multipole analysis approach to the more general approach based on the theory of characteristic modes. In many ways, he has been a wonderful supervisor. It was also he who constantly introduced me to others researchers in the field of antennas.

In this respect, I am deeply grateful to Prof. Dr.-Ing. Klaus Solbach who also supervised this work, for the great interest shown, for his unconditional support and availability, purposeful advice and for several discussions we had all along the whole process leading to the results achieved.

My sincere and particular thanks to Prof. Dr.-Ing. Heinz Chaloupka for his interest to this work, for his fast and prompt reaction as second instructor (Korreferent).

My deepest gratitude goes first to students who within their master thesis and internships

considerably contributed to this project, to my collegues in RF/Antenna Teams in Siemens Mobile in Bocholt as well as in BenQ Mobile in Kamp-Lintfort and in the department of Microwave and RF-Technology of the University of Duisburg-Essen for the great working atmosphere and for their availability to help.

Contents

List of Tables

List of Figures

Chapter 1

Introduction

Background

Mobile phones have undergone a rapid evolution within the past decade from "pure" phones to multistandard, multiband communication devices. Coverage of the four GSM bands, UMTS and the $2.4\,\mathrm{GHz}$ ISM bands is already a standard requirement. Newly allocate 3G spectrum and additional bands for use with e.g. DVB-H, WLAN, GPS are on the industry roadmap. At the same time a dramatic reduction of the size of mobile terminals has taken place. Miniaturisation leaves ever less space for the antenna, a fact which is in conflict with well known fundamental limits on bandwidth as a function of antenna volume.

Up to now a mobile terminal antenna can be designed based on two opposite basic design concepts. The first one tries to isolate the antenna from the terminal so that current excited on the conductive chassis is minimized [2], whereas the second tries to utilize or even maximize radiation from the current excited on the chassis terminal. The theoretical maximum bandwidth and efficiency of the antenna element isolated from the chassis depends only on its dimensions [3], [4], [5]. Currently, however, the size allowed for the antenna e.g. in mobile phones is too small for an isolated antenna to have a sufficient operation bandwidth for most communication systems, especially around $1\,\mathrm{GHz}$ and below. When a small antenna is used to excite strong radiating currents on the chassis, it is possible to obtain much larger operation bandwidths. This has made the use of currently very compact internal antennas possible. Typically, the bandwidth of a small antenna mounted on a mobile terminal is several times larger than that of the same antenna on a large or infinite ground plane. This ties the antenna performance strongly to the mechanical design of the whole terminal. As a significant part of the radiation comes from the chassis currents, the lossy tissues of a human's head and hand in the near-field, which often cover most of a small terminal, can be expected to have a strong performance degrading effect on the

combination of an antenna and a chassis.
Multiband mobile phone antenna design is increasingly challenging. To achieve efficient radiation, optimum use of the available length or volume, respectively, of a device must be made. This implies a shift away from a traditional design paradigm which focuses on the antenna element while the chassis is surrendered to the arbitrariness of the mechanical design. A more adequat view loomed in recent years when increased attention was given to the interaction between an antenna element and the "ground plane" [6]-[7]. A further step was made in [8], [9] where for the first time electromagnetic analysis of the chassis was recognized as an important topic on its own. The logical completion of the indicated change in perspective is the adoption of a new design paradigm which focuses on the utilisation and tuning of radiating chassis modes while the antenna element is understood mainly as a chassis modes exciter. Considering the combination of performance in terms of radiation efficiency, bandwidth, Specific Absorption Rate (SAR) and the esthetic which mostly defines the geometry of the handheld devices, the design and positioning of the antenna element on the plateform are challenges that require the knowledge of the radiation properties of the chassis separately. Recently [6], the effect of the chassis or circuit board length on the bandwidth has been investigated for Bar-Type (monoblock) phones in the range of $80\,\mathrm{mm}$-$150\,\mathrm{mm}$. The dependency of the bandwidth for a $900\,\mathrm{MHz}$ patch was clearly noticed and the investigation has revealed a maximum bandwidth at a length of $130\,\mathrm{mm}$. Inspection of these observations obviously suggests that not only the nominal antenna element (exciter) contributes to the overall radiation properties but also the chassis and raises the problem of coupling between both entities. In [10] the performance of the mobile devices antenna-chassis is investigated based on an approximate decomposition of the waves on the structure in two resonant wavemodes: the antenna element wavemodes and the chassis wavemodes. An equivalent circuit model is used to analyse the coupling mechanism between both entities where the chassis and antenna element wavemodes are considered as low- and high-Q resonator respectively. This approach suffers from the fact that one looms the contribution of the antenna element and the chassis in the radiation properties.

Objectives of the Work

This work proposes a novel approach of the problem. The problem which has so far mainly been discussed in terms of equivalent circuits is handled on a field theoretical level. To provide an insight into the coupling mechanism between antenna and chassis, we separately consider chassis and antenna element as two distinctive entities and investigate the radiation properties of the chassis on its own. From this point of view, an optimal design and location of the antenna element can be obtained through the knowledge of the radiation properties

of the chassis. In [11] chassis radiation properties are investigated by post-processing output data from standard CEM software. This method is based on a simplified analysis of the far-field radiation properties of a small radiator. The effect of variation of the length and width on the chassis resonance frequency have been studied. In [12] [13] the theory of characteristic modes [14] is used to numericaly analyse the radiation properties of the chassis.

This thesis focuses on the investigation of radiation properties of mobile phone chassis solely, independently on their form factors by making use of the theory of characteristic modes. An arbitrary current distribution on the chassis is understood as a linear combination of characteristic current and expanded as such. Obtained expansion coefficients further analysed, provide knowledge on the chassis eigenradiation properties as well as on the optimization of the coupling mechanism between the external exciting field and the chassis wavemodes. An algorithm for the numerical evaluation of characteristic (currents) modes is elaborated. This analysis provides enough information on the radiation properties of the chassis which are used for the investigation of an optimal placement and design of the exciter. Application examples are presented for Bar-Type (Monoblock) and Folder-Type mobile phones widely spread on the market.

Chapter 2

Analysis and Design Methods for Mobile Phones Antennas

2.1 Optimization Criterion

2.1.1 Total Radiated Power (TRP)

The Total Radiated Power or TRP introduced by the Cellular Telecommunication and Internet Association (CTIA) in its certification program is the sum of all power radiated by the antenna, regardless of direction or polarization. If the antenna were enclosed in a perfectly absorbing sphere, the TRP would be the power that would be absorbed by that sphere. The TRP is related to the maximum available power P_{avail} fed into the antenna from the power amplifier by

$$TRP = (1 - |s_{11}|^2) \cdot \eta_{\text{rad}} \cdot P_{\text{avail}} \tag{2.1}$$

where s_{11} is the antenna reflection factor and η_{rad} the radiation efficiency of the antenna. Considering $U(\theta, \phi)$ the radiation intensity at each angle in Watts/steradian the TRP is expressed as

$$TRP = \int_0^{\pi} \int_0^{2\pi} U(\theta, \phi) \sin(\theta) \, \mathrm{d}\phi \, \mathrm{d}\theta \tag{2.2}$$

2.1.2 Considered Cases

Related to handheld devices in mobile communication, the definition above includes two cases.

- Free-Space
  In this case, the characteristics of the Antenna Under Test (AUT) are measured under

free-space conditions

- Simulated-Use
  In this case, the AUT is placed against a Standard Anthropomorphic Model (SAM) head phantom.

2.2 Specific Absorption Rate (SAR)

To protect a mobile phone user from electromagnetic iradiation exposure, safety guidelines have been set by regulatory agencies. A dosimetric parameter for the evaluation of the iradiation is the *specific absorption rate*, which shows up to be an important parameter in the design specifications of handheld devices in mobile communication.
It is a measure to quantify the microwave energy absorbed by unit of tissue and defined as

$$SAR = \sigma_{\text{eff}} \frac{|E|^2_{\text{rms}}}{\rho} \tag{2.3}$$

where σ_{eff} represents the effective conductivity of the tissue (S/m), $|E|_{\text{rms}}$ is the root-mean-square (rms) value of the induced electric field strength (V/m), and ρ is the tissue mass density (kg/m^3). The SAR is expressed in units of watts per kilogram (W/kg) and denotes the time rate of RF energy absorption at a given location inside the tissue.

The determination of the SAR in human tissues can be in general performed by experimental and numerical techniques. Both techniques have been subjects of intensive studies. Descriptions on measurement setups and methods are proposed in [15] [16] [17] and on numerical dosimetry in [18].

2.2.1 Total Communication Power (TCP)

The Telephone Communication Power (TCP) is the power leaving a closed surface, which surrounds the phone and the head phantom when these are located far from other objects. It is the maximum available power P_{avail}, fed into the mobile phone's antenna from the power amplifier,
minus the fraction of the power reflected due to an actual mismatch at the antenna port,

$$P_{\text{ref}} = |s_{11}|^2 P_{\text{avail}} \tag{2.4}$$

where s_{11} is the antenna reflection factor
minus the power P_{diss}, dissipated as heat in the antenna and expressed as follows

$$P_{\text{diss}} = (1 - \eta_{\text{rad}})(P_{\text{avail}} - P_{\text{ref}}) = (1 - \eta_{\text{rad}})(1 - |s_{11}|^2)P_{\text{avail}} \tag{2.5}$$

where η_{rad} is the radiation efficiency
minus the power $P_{\text{user,abs}}$ which is absorbed in the user's head and hand and expressed as

$$\begin{aligned} P_{\text{user,abs}} &= (1-\eta_{\text{user}})(P_{\text{avail}} - P_{\text{ref}} - P_{\text{diss}}) \\ &= (1-\eta_{\text{user}})\eta_{\text{rad}}(1-|s_{11}|^2)P_{\text{avail}} \end{aligned} \tag{2.6}$$

Finaly the Total Communication Power is expressed as follows by making use of the previous equations.

$$\begin{aligned} P_{\text{tcp}} &= P_{\text{avail}} - P_{\text{ref}} - P_{\text{diss}} - P_{\text{user,abs}} \\ &= (1-|s_{11}|^2)\cdot\eta_{\text{user}}\cdot\eta_{\text{rad}}P_{\text{avail}} \end{aligned} \tag{2.7}$$

2.2.2 Optimization Criterion

In the scope of this work the optimization criterion considered is to maximize the ratio

$$\frac{P_{\text{tcp}}}{P_{\text{avail}}} = (1-|s_{11}|^2)\cdot\eta_{\text{user}}\cdot\eta_{\text{rad}} \tag{2.8}$$

which leads to the maximization of individual components on the right-hand side of (2.8) under the condition that $P_{\text{avail}} = Const.$
Maximization of the radiation efficiency

- η_{rad}

requires the reduction of the part of the available power converted into heat. This implies the development of shielding methods to avoid heat conversion inside the mobile phone. This is not handled in the frame of this work, but could be a topic for future research.
Maximization of

- η_{user}

is nothing else as to minimize the SAR. This problem can be solved by driving the radiated energy delivered by the mobile phone away from the head. This means at the same time a very poor reception of the signal arriving from the head's side. SAR minimization is is not handled in the frame of this work.
Maximization of

- $1-|s_{11}|^2$

clearly means the minimization of the reflection factor s_{11}. At $900\,\mathrm{MHz}$ it has been observed that the radiation losses due to the antenna element wavemode represent typically less than 10% of the total power. This clearly means that the antenna element works mainly as an element, that couples the chassis resonant modes [10]. The Printed Circuit Board radiates and influences the total radiated power. A minimization of the reflection factor s_{11} can be achieved by optimal coupling between the antenna element and the chassis or PCB. The coupling is determined by the design and location of the antenna element on the chassis. Analysis of the coupling mechanism between the antenna element and the mobile phone chassis is of high interest and has recently been treated in [10] by making use of the Equivalent Circuit Model.
This work handles that problem from a field theoretical point of view by taking advantage of the theory of characteristic modes. Below, a short summary of the equivalent circuit model is given as well as guidelines on the theory of characteristic modes.

2.3 Equivalent Circuit Model

The structure of the antenna–chassis combination is divided into two significant parts: the antenna element and the chassis. It is considered that currents flowing on the chassis are induced through electromagnetic coupling from the antenna element, which is in turn excited by its feed. In this approach, the antenna element is considered to be self-resonant and the length of the chassis is assumed to be closed to some multiple of half wavelength and a simple lumped-component equivalent circuit model of the antenna–chassis combination, is that of coupled parallel and series resonators as proposed in Fig. 2.1 This approach

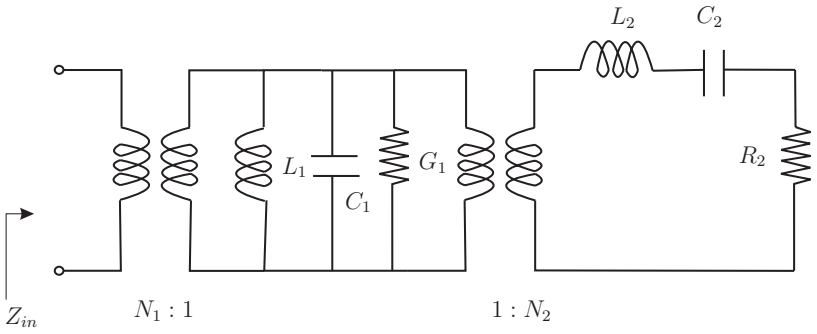

Figure 2.1: Circuit Model of the Combination of a Single-resonant antenna element and Chassis.

then assigns large and small values to Q_1 and Q_2 respectively, radiation quality factors of

the chassis and antenna element for simulations. The drawback here is that one unclearly recognizes the contribution from each part in the overall radiation properties, a mechanical change in the geometry of the chassis can't really be evaluated.

2.4 Theory of Characteristic Modes

As already mentioned, the theory of characteristic modes for conducting bodies is a powerful analytical concept for the design of small antennas, similar to what modal analysis means for the design of waveguide circuits. This theory was introduced by Robert Garbacz in [19] and further elaborated by Roger Harrington in [14].

2.4.1 Operator Equation

An impressed external electric field $\boldsymbol{E}^{\mathrm{ex}}$ on a conducting body with surface S, induces on the conducting surface a current $\boldsymbol{J}_{\mathrm{s}}$ which generates a field $\boldsymbol{E}^{s}$.
Expression of the generated field is obtained as specified in B.7

$$\boldsymbol{E}^{s}(\boldsymbol{J}_{\mathrm{s}}) = \frac{1}{j\omega\epsilon} \int\limits_{V} \boldsymbol{J}_{\mathrm{s}}(\boldsymbol{r}') \cdot \left[\nabla'\nabla' + k^2\right] G(\boldsymbol{r}, \boldsymbol{r}') \, \mathrm{d}v$$

On the surface of the conducting body according to the boundary conditions, the tangential component of the electric field vanishes (assuming no magnetic current on the surface). i.e.

$$\left(\boldsymbol{E}^{\mathrm{ex}} + \boldsymbol{E}^{s}\right)_{tan} = 0$$

Denoting by $\boldsymbol{E}^{\mathrm{ex}}_{\mathrm{tan}}$ the tangential component of $\boldsymbol{E}^{\mathrm{ex}}$ and rewritten with the operator $\widehat{\mathbf{L}}$ the above relation one obtains

$$\widehat{\mathbf{L}}_{tan}(\boldsymbol{J}_{\mathrm{s}}) - \boldsymbol{E}^{\mathrm{ex}}_{\mathrm{tan}} = 0 \tag{2.9}$$

For simplification purposes we denote $\widehat{\mathbf{L}}_{tan} = \widehat{\mathbf{Z}}$ and

$$\widehat{\mathbf{Z}} = \widehat{\mathbf{R}} + \mathrm{j}\widehat{\mathbf{X}}$$

where $\widehat{\mathbf{R}} = \frac{1}{2}\left(\widehat{\mathbf{Z}} + \widehat{\mathbf{Z}}^{*}\right)$ and $\widehat{\mathbf{X}} = \frac{1}{2j}\left(\widehat{\mathbf{Z}} - \widehat{\mathbf{Z}}^{*}\right)$ are Hermitian operators.

2.4.2 Characteristic Modes Problem Formulation

The characteristic modes theory focuses on the operator $\widehat{\mathbf{Z}}$ for its representation and description of the system. Resolution of (2.9) will provide a solution $\boldsymbol{J}_{\mathrm{s}}$ as reponse to the

effect $\boldsymbol{E}_{\tan}^{\mathrm{ex}}$ on the system. Characteristic modes can be understood as natural and inherent system responses and a solution such as $\boldsymbol{J}_{\mathrm{s}}$ to a given effect is only a combination of these natural responses.
To arrives at those characteristic modes the following eigenvalue problem is formulated in [14]

$$\widehat{\mathbf{Z}}(\boldsymbol{J}_{\mathrm{s},n}) = \nu_n \widehat{\mathbf{M}}(\boldsymbol{J}_{\mathrm{s},n}) \tag{2.10}$$

where ν_n , $\boldsymbol{J}_{\mathrm{s},n}$ are eigenvalues and eigenfunctions respectively, and a weight operator $\widehat{\mathbf{M}}$ to be chosen. Observe that the choice $\widehat{\mathbf{M}} = 0$ leads to homogeneous solutions and $\widehat{\mathbf{M}} = \widehat{\mathbf{I}}$ (where $\widehat{\mathbf{I}}$ is the identity operator) provides eigenvalues and eigenfunctions of the system under study. To obtain real and orthogonal eigenfunctions the choice $\widehat{\mathbf{M}} = \widehat{\mathbf{R}}$ should be made.
In fact, (2.10) further developed, leads to

$$\begin{aligned} (\widehat{\mathbf{R}} + \mathrm{j}\widehat{\mathbf{X}})(\boldsymbol{J}_{\mathrm{s},n}) &= \nu_n \widehat{\mathbf{R}}(\boldsymbol{J}_{\mathrm{s},n}) \\ \widehat{\mathbf{X}}(\boldsymbol{J}_{\mathrm{s},n}) &= \lambda_n \widehat{\mathbf{R}}(\boldsymbol{J}_{\mathrm{s},n}) \end{aligned} \tag{2.11}$$

where $\nu_n = 1 + \mathrm{j}\lambda_n$.
$\widehat{\mathbf{X}}$ and $\widehat{\mathbf{R}}$ are real and symmetric operators hence from the properties of Hermitian operators mentioned in section B.2 it can be easily established that (2.11) yields real eigenfunctions and eigenvalues.

2.4.3 Modal Orthogonality Relations

Orthogonality relations exist between eigenfunctions (eigenmodes) solutions of (2.11)
Let's consider ($\boldsymbol{J}_{\mathrm{s},n}$, λ_n) and ($\boldsymbol{J}_{\mathrm{s},m}$, λ_m) two distinctive couples solution of equation (2.11) with $\lambda_n \neq \lambda_m$.
$\widehat{\mathbf{X}}$ has the property of been Hermitian, this leads to

$$\begin{aligned} \langle \boldsymbol{J}_{\mathrm{s},m}, \widehat{\mathbf{X}}(\boldsymbol{J}_{\mathrm{s},n}) \rangle &= \langle \widehat{\mathbf{X}}(\boldsymbol{J}_{\mathrm{s},m}), \boldsymbol{J}_{\mathrm{s},n} \rangle \\ \langle \boldsymbol{J}_{\mathrm{s},m}, \lambda_n \widehat{\mathbf{R}}(\boldsymbol{J}_{\mathrm{s},n}) \rangle &= \langle \lambda_m \widehat{\mathbf{R}}(\boldsymbol{J}_{\mathrm{s},m}), \boldsymbol{J}_{\mathrm{s},n} \rangle \\ (\lambda_n - \lambda_m) \langle \boldsymbol{J}_{\mathrm{s},m}, \widehat{\mathbf{R}}(\boldsymbol{J}_{\mathrm{s},n}) \rangle &= 0 \end{aligned} \tag{2.12}$$

In (2.12) ($\lambda_n \neq \lambda_m$) leads to the orthogonality relation

$$\langle \boldsymbol{J}_{\mathrm{s},m}, \widehat{\mathbf{R}}(\boldsymbol{J}_{\mathrm{s},n}) \rangle = 0 \tag{2.13}$$

With the same procedure as above, one also arrives at another orthogonality relation

$$\langle \boldsymbol{J}_{\mathrm{s},m}, \widehat{\mathbf{X}}(\boldsymbol{J}_{\mathrm{s},n}) \rangle = 0 \tag{2.14}$$

From a combination of (2.13) and (2.14), it can be deduced that

$$\langle \boldsymbol{J}_{\mathrm{s},m}, \widehat{\mathbf{Z}}(\boldsymbol{J}_{\mathrm{s},n})\rangle = 0 \tag{2.15}$$

Since the $\boldsymbol{J}_{\mathrm{s},n}$s are real, the above orthogonality relations are also valid for the inner product.

$$\langle \boldsymbol{J}_{\mathrm{s},m}{}^{*}, \widehat{\mathbf{R}}(\boldsymbol{J}_{\mathrm{s},n})\rangle = 0 \tag{2.16}$$

$$\langle \boldsymbol{J}_{\mathrm{s},m}{}^{*}, \widehat{\mathbf{X}}(\boldsymbol{J}_{\mathrm{s},n})\rangle = 0 \tag{2.17}$$

$$\langle \boldsymbol{J}_{\mathrm{s},m}{}^{*}, \widehat{\mathbf{Z}}(\boldsymbol{J}_{\mathrm{s},n})\rangle = 0 \tag{2.18}$$

2.4.4 Modal Development

As already specified above (2.4.2), a current induced by impinging waves on the surface of a conducting body can be written as a superposition of characteristic modes,

$$\boldsymbol{J}_{\mathrm{s}} = \sum_{m} \alpha_m \boldsymbol{J}_{\mathrm{s},m} \tag{2.19}$$

where α_n are coefficients to be determined. Inserting (2.19) in (2.9) and making use of the linearity of the operator gives

$$\sum_{m} \alpha_m \widehat{\mathbf{Z}}(\boldsymbol{J}_{\mathrm{s},m}) - \boldsymbol{E}^{\mathrm{ex}}_{\tan} = 0 \tag{2.20}$$

Taking the inner product of (2.20) with $\boldsymbol{J}_{\mathrm{s},n}$ where $m \in \{1, 2 \cdots\}$ gives

$$\sum_{m} \alpha_m \langle \boldsymbol{J}_{\mathrm{s},n}, \widehat{\mathbf{Z}}(\boldsymbol{J}_{\mathrm{s},m})\rangle = \langle \boldsymbol{J}_{\mathrm{s},n}, \boldsymbol{E}^{\mathrm{ex}}_{\tan}\rangle \tag{2.21}$$

By making use of the orthogonality relations (2.15), the previous equation (2.21) reduces to

$$\alpha_n (1 + j\lambda_n) \langle \boldsymbol{J}_{\mathrm{s},n}, \widehat{\mathbf{R}}(\boldsymbol{J}_{\mathrm{s},n})\rangle = \langle \boldsymbol{J}_{\mathrm{s},n}, \boldsymbol{E}^{\mathrm{ex}}_{\tan}\rangle \tag{2.22}$$

where $\langle \boldsymbol{J}_{\mathrm{s},m}, \widehat{\mathbf{Z}}(\boldsymbol{J}_{\mathrm{s},n})\rangle = (1 + j\lambda_n)\langle \boldsymbol{J}_{\mathrm{s},m}, \widehat{\mathbf{R}}(\boldsymbol{J}_{\mathrm{s},n})\rangle$ was applied.
The coefficient α_n can now be obtained from (2.22) and its substitution into (2.19) yields the following expression for the induced current,

$$\boldsymbol{J}_{\mathrm{s}} = \sum_{m} \frac{\langle \boldsymbol{J}_{\mathrm{s},m}, \boldsymbol{E}^{\mathrm{ex}}_{\tan}\rangle}{(1 + j\lambda_m)\langle \boldsymbol{J}_{\mathrm{s},m}, \widehat{\mathbf{R}}(\boldsymbol{J}_{\mathrm{s},m})\rangle} \boldsymbol{J}_{\mathrm{s},m} \tag{2.23}$$

where the cross-product $\langle \boldsymbol{J}_{\mathrm{s},m}, \boldsymbol{E}^{\mathrm{ex}}_{\tan} \rangle$ is called the *modal excitation coefficient*.
Normalization of the eigenfunctions $\boldsymbol{J}_{\mathrm{s},m}$ gives $\langle \boldsymbol{J}_{\mathrm{s},m}, \widehat{\mathbf{R}}(\boldsymbol{J}_{\mathrm{s},m}) \rangle = 1$ and simplifies the expression in (2.23) to

$$\boldsymbol{J}_{\mathrm{s}} = \sum_{m} \frac{\langle \boldsymbol{J}_{\mathrm{s},m}, \boldsymbol{E}^{\mathrm{ex}}_{\tan} \rangle}{1 + j\lambda_m} \boldsymbol{J}_{\mathrm{s},m} \tag{2.24}$$

2.4.5 Theory of Characteristic Modes for System Analysis

In this section, a step further is done refering to the work proposed in [14]. An elaboration of the usefulness of the theory of characteristic modes for system analysis is performed.

- Poynting theorem

$$\begin{aligned} -\frac{1}{2} \int_V (\boldsymbol{E} \cdot \boldsymbol{J}_s{}^* + \boldsymbol{H}^* \cdot \boldsymbol{M}_s)\, \mathrm{d}v = \frac{1}{2} \oint_S \boldsymbol{E} \times \boldsymbol{H}^* \cdot \mathrm{d}\boldsymbol{s} \\ + \frac{\sigma}{2} \int_V |\boldsymbol{E}|^2 \,\mathrm{d}v + \frac{\omega}{2} \int_V \left(\epsilon'' |\boldsymbol{E}|^2 + \mu'' |\boldsymbol{H}|^2\right) \mathrm{d}v \\ + \mathrm{j}\frac{\omega}{2} \int_V \left(\epsilon' |\boldsymbol{E}|^2 - \mu' |\boldsymbol{H}|^2\right) \mathrm{d}v \end{aligned} \tag{2.25}$$

where S is a closed surface enclosing the volume V, $\varepsilon = \varepsilon' - \mathrm{j}\varepsilon''$ and $\mu = \mu' - \mathrm{j}\mu''$ are respectively, complex permittivity and permeability to allow loss.
The Poynting theorem states that the power delivered by the sources is equal to the sum of the power radiated through the surface, the power dissipated to heat in the volume, and the reactive energy stored in the volume and the flow of reactive energy per unit in time.
Applying the above theorem in the abscence of magnetic source in free space to the eigen-currents $\boldsymbol{J}_{\mathrm{s},n}$ and $\boldsymbol{J}_{\mathrm{s},m}$, we obtain the following cross-product

$$\langle \boldsymbol{J}_{\mathrm{s},m}{}^*, \widehat{\mathbf{Z}}(\boldsymbol{J}_{\mathrm{s},n}) \rangle = \oint_S \boldsymbol{E}_m \times \boldsymbol{H}_n{}^* \cdot \mathrm{d}\boldsymbol{s} + \mathrm{j}\omega \int_V (\mu \boldsymbol{H}_m \cdot \boldsymbol{H}_n{}^* - \epsilon \boldsymbol{E}_m \cdot \boldsymbol{E}_n{}^*)\, \mathrm{d}v \tag{2.26}$$

Using the orthogonality relation (2.15), the following result can be obtained from the above equation (2.26)

$$\oint_S \boldsymbol{E}_m \times \boldsymbol{H}_n{}^* \cdot \mathrm{d}\boldsymbol{s} + \mathrm{j}\omega \int_V (\mu \boldsymbol{H}_m \cdot \boldsymbol{H}_n{}^* - \epsilon \boldsymbol{E}_m \cdot \boldsymbol{E}_n{}^*)\, \mathrm{d}v = 2(1 + j\lambda_n)\delta_{nm} P_n \tag{2.27}$$

where $P_n = \frac{1}{2}\langle \boldsymbol{J}_{\mathrm{s},n}, \widehat{\mathbf{R}}(\boldsymbol{J}_{\mathrm{s},n})\rangle$ represents the power radiated by the n^{th} characteristic modes and

$$\delta_{mn} = \begin{cases} 1 & \text{for } m = n \\ 0 & \text{for } m \neq n \end{cases} \tag{2.28}$$

In the far-field region, the following relation between the magnetic and electric fields is valid, where $\boldsymbol{r}$ denotes the unit radial vector and $\eta = \sqrt{\frac{\mu}{\epsilon}}$

$$\boldsymbol{E}_n = \eta \boldsymbol{H}_n \times \boldsymbol{r} \tag{2.29}$$

In the far-field conditions a summation of (2.27) with its conjugate with m and n interchanged gives

$$\frac{1}{\eta} \oint_S \boldsymbol{E}_n \cdot \boldsymbol{E}_m{}^* \, \mathrm{d}s = \delta_{mn} P_n \tag{2.30}$$

Substituting (2.29) in (2.30), the following relation between characteristic magnetic fields in the far-field region is obtained.

$$\eta \oint_S \boldsymbol{H}_n \cdot \boldsymbol{H}_m{}^* \, \mathrm{d}s = \delta_{mn} P_n \tag{2.31}$$

(2.30) and (2.31) clearly shows that characteristic electric and magnetic far-fields are orthogonal which obviously implies the orthogonality of the charateristic patterns.
Subtraction of (2.27) from its conjugate yields

$$\omega \int_V \left(\mu \boldsymbol{H}_m \cdot \boldsymbol{H}_n{}^* - \epsilon \boldsymbol{E}_m \cdot \boldsymbol{E}_n{}^*\right) \mathrm{d}v = 2\lambda_n \delta_{nm} P_n \tag{2.32}$$

From equation (2.32) a system analysis can be performed.

- Capacitive modes
  In the above equation (2.32) the choice $m = n$ and $\lambda_n < 0$ leads to

  $$\int_V |\boldsymbol{H}_n|^2 \, \mathrm{d}v < \int_V |\boldsymbol{E}_n|^2 \, \mathrm{d}v$$

  which shows that the stored electric energy in the volume V predominates over the stored magnetic energy. We therefore call the associated modes *capacitive modes*.

- Inductive modes
  In the above equation (2.32) chosing $m = n$ and $\lambda_n > 0$ leads to

$$\int_V |\boldsymbol{H}_n|^2 \, \mathrm{d}v > \int_V |\boldsymbol{E}_n|^2 \, \mathrm{d}v$$

  which shows that the stored magnetic energy in the volume V predominates over the stored electric energy. We therefore call the associated modes *inductive modes*.

- Externally resonant modes
  In the above equation (2.32) chosing $m = n$ and $\lambda_n = 0$ leads to

$$\int_V |\boldsymbol{H}_n|^2 \, \mathrm{d}v = \int_V |\boldsymbol{E}_n|^2 \, \mathrm{d}v$$

  which corresponds to the case of resonance and the associated modes are called *externally resonant modes*. Modes corresponding to $|\lambda_n| = \infty$ are responsible for the resonance of the internal cavity of the conducting surface and do not enter into radiation and scattering problems.

Chapter 3

Numerical Analysis of Characteristic Modes

The analysis of characteristic modes amounts to the solution of a generalized real eigenvalues problem based on the knowledge of the impedance matrix $\boldsymbol{Z}$ which is related to the linear operator $\widehat{\mathbf{Z}}$. The problem first described with operators $\widehat{\mathbf{R}} = \mathrm{Re}\{\widehat{\mathbf{Z}}\}$ and $\widehat{\mathbf{X}} = \mathrm{Im}\{\widehat{\mathbf{Z}}\}$ should be converted into a matrix equation.

3.1 Derivation of the Matrix Equation

The transformation of the linear-operator equation

$$\widehat{\mathbf{X}}(\boldsymbol{J}_{\mathrm{s},n}) = \lambda_n \widehat{\mathbf{R}}(\boldsymbol{J}_{\mathrm{s},n}) \tag{3.1}$$

to matrix equation is achieved by making use of the method of moments (MoM) [20] which is attractive in the sense that it avoids any artificial termination of the computational volume (absorbing boundary conditions) which might result in non-physical solutions. The surface current density $\boldsymbol{J}_{\mathrm{s},n}$ representing here the unknown parameter in the linear-operator equation is first expanded in a linear combination of basis functions $\{\boldsymbol{B}_j, j = 1, 2 \ldots N\}$ as

$$\boldsymbol{J}_{\mathrm{s},n} = \sum_{j=1}^{N} I_j \boldsymbol{B}_j \tag{3.2}$$

where the expansion coefficients I_j should be determined. Replacing (3.2) in (3.1) and taking the inner product of the resulting equation with the set of weighting functions $\{\boldsymbol{W}_i, i = 1, 2 \ldots N\}$ yields the set of following equations where the linearity of $\widehat{\mathbf{X}}$ and

$\widehat{\mathbf{R}}$ has been used.

$$\sum_{j=1}^{N} I_j \langle \widehat{\mathbf{X}} \boldsymbol{B}_j, \boldsymbol{W}_i \rangle = \lambda_n \sum_{j=1}^{N} I_j \langle \widehat{\mathbf{R}} \boldsymbol{B}_j, \boldsymbol{W}_i \rangle, \; i = 1, 2 \ldots N \tag{3.3}$$

Written in the matrix notation, (3.3) gives

$$\boldsymbol{X}\boldsymbol{I}_n = \lambda_n \boldsymbol{R}\boldsymbol{I}_n \tag{3.4}$$

where $X_{ij} = \langle \boldsymbol{W}_i, \widehat{\mathbf{X}} \boldsymbol{B}_j \rangle$, $R_{ij} = \langle \boldsymbol{W}_i, \widehat{\mathbf{R}} \boldsymbol{B}_j \rangle$ and I_j denote respectively, the coefficients of matrices $\boldsymbol{X}$, $\boldsymbol{R}$ and the column matrix $\boldsymbol{I}_n$.

Obviously the solution of the matrix equation (3.4) depends on the choice of basis and weighting functions. The choice of $\{\boldsymbol{B}_j\}$ and $\{\boldsymbol{W}_i\}$ may be conditioned by factors such as, the accuracy of the desired solution, the ease of evalution of matrix elements the size of the matrix that can be inverted and the realization of a well-conditioned matrix. For the specific choice $\{\boldsymbol{B}_j = \boldsymbol{W}_j\}$ known as *Galerkin's method* [21, 22], the matrices $\boldsymbol{X}$ and $\boldsymbol{R}$ are symmetric. This provides a similarity with (3.1) since the operators $\widehat{\mathbf{X}}$ and $\widehat{\mathbf{R}}$ are also symmetric and should lead to much more accurate approximation. Another advantage is the reduction of the solutions computation time, since symmetric matrices are much easier to handle. Its drawback lies in the evaluation of the coefficients R_{ij} and X_{ij} which appears to be difficult to perform and time consuming.

Another choice of basis and weighting functions requires that equation (3.1) be satisfied at discrete points in the region of interest. This procedure is known as *point-matching method* and corresponds to chosing the weighting functions as dirac $\boldsymbol{W}_j(\boldsymbol{r}) = \delta(\boldsymbol{r} - \boldsymbol{r}_j)$ where $\boldsymbol{r}_j$ represents the test point. This method takes advantage from the properties of the δ-function to easily evaluate the coefficients R_{ij} and X_{ij}. However the matrices $\boldsymbol{R}$ and $\boldsymbol{X}$ are not symmetric which means a biased description of the problem we are dealing with and might consequently lead to unaccurate solutions.

3.2 Numerical Approach for the Resolution of Eq. (3.4)

The problem here is to determine the eigenvalues (λ_n) and the corresponding eigenvectors ($\boldsymbol{I}_n$) as defined in (3.4). Equation (3.4) is a well-known mathematical problem and is the so-called *generalized eigenvalue problem*. It has been subjects of many publications in mathematics in the past years. The approach proposed here for the resolution of the generalized eigenvalues problem articulates on two points:

- the reduction of the generalized eigenvalues problem to elementary generalized eigenvalues problems of order one or two which are much easier to solve

- the resolution of the elementary generalized eigenvalues problems which provides the desired solutions

The first point, which stipulates to split the problem into elementary problems is sustained by the decomposition theorem (A.1.1) and its corollary as mentioned in the Appendix.
In fact, from corollary (A.1.1) the matrices pair $(\boldsymbol{X}, \boldsymbol{R})$ can be reduced into triangular block form as follows:

$$\boldsymbol{U}^H \cdot (\boldsymbol{X}, \boldsymbol{R}) \cdot \boldsymbol{V} = \left(\begin{bmatrix} \boldsymbol{X}_{11} & \boldsymbol{X}_{12} \\ 0 & \boldsymbol{X}_{22} \end{bmatrix}, \begin{bmatrix} \boldsymbol{R}_{11} & \boldsymbol{R}_{12} \\ 0 & \boldsymbol{R}_{22} \end{bmatrix} \right) \tag{3.5}$$

and

$$\lambda(\boldsymbol{X}, \boldsymbol{R}) = \lambda(\boldsymbol{X}_{11}, \boldsymbol{R}_{11}) \cup \lambda(\boldsymbol{X}_{22}, \boldsymbol{R}_{22}) \tag{3.6}$$

where $\lambda(\boldsymbol{X}, \boldsymbol{R})$ denotes the set of all eigenvalues for the pair $(\boldsymbol{X}, \boldsymbol{R})$.
Eq. (3.6) clearly shows that the initial problem Eq. (3.4) has been split into two smaller problems, which represents the main idea to arrive at the desired solutions.

The key idea implemented here for computing the generalized eigenvalues and eigenvectors is based on the above meaningful decomposition. In this context a useful application of the above decomposition shows that the generalized eigenvalues can be easily obtained. Namely, by chosing a decomposition which provides matrices on the diagonals $\boldsymbol{X}_{11}, \boldsymbol{R}_{11}, \boldsymbol{X}_{22}, \boldsymbol{R}_{22}$ with dimensions less or equal to two. If matrix blocks on the diagonal are not with dimensions less or equal to two, subsequent decompositions can be applied for further reduction.

A decomposition which provides matrix blocks on the diagonal with dimensions less or equal to two do exist. Theorem (A.1.2) stipulates nothing else as the existence of such a decomposition.

As it can be observed from theorem (A.1.2), such a decomposition depends on the existence of the transformation matrices. Some mathematical algorithms specialized for such problems have been developed. A well-known algorithm for this purpose is the so called $\boldsymbol{QZ}$-algorithm. Details on this algorithm are given in section A.1.1, where the decomposition amounts to the computation of the transformation matrices $\boldsymbol{Q}$ and $\boldsymbol{Z}$.
For an appropriate resolution of our problem which is to find a decomposition of the matrices pair $(\boldsymbol{X}, \boldsymbol{R})$ such that matrices block on the diagonal are of dimensions less or equal to two, two versions of the $\boldsymbol{QZ}$-algorithm have been applied:

- The $\boldsymbol{QR}$-algorithm

and

- The algorithm for Reduction to Hessenberg-triangular form

The algorithm for Reduction to Hessenberg-triangular form is proposed in the Appendix in the section A.1.2.
This algorithm is implemented in the LAPACK routine DGGHRD.
The reduction to Hessenberg-triangular form implemented is solely based on Givens rotations. An example of an $n \times n$ *Givens elementary rotation* is presented in section A.1.1 which generates a zero at the position (i, j) in the transformed matrix. The Reduction to Hessenberg-triangular is necessary to avoid excessive fill-in in the triangular $\boldsymbol{R}$ matrix. This unfortunately means that this algorithm performs poorly on large matrices. In [23] an alternative is proposed by approching the Hessenberg-triangular form in two stages. In the first stage, the matrix $\boldsymbol{X}$ is reduced to block upper Hessenberg form using a straightforward block version of the above algorithm. The second stage consists of changing the unwanted subdiagonal elements to the bottom right corner of the matrix $\boldsymbol{X}$. Extensive numerical experiments in [23] show that this alternative outperforms the LAPACK routine DGGHRD by a factor 2-3.

3.3 Algorithm for the Resolution of the Generalized Eigenvalues Problem

The resolution of the generalized eigenvalues problem involves many steps. Let compute the generalized eigenvalues of a matrix pair $(\boldsymbol{A}, \boldsymbol{B})$, the following steps could be performed:

3.3.1 Balancing

Balancing is a processing step, which often has positive effects on the performance and accuracy of numerical methods for computing eigenvalues and therefore has obtained early attention in the development of linear algebra [24, 25] Balancing usually consists of two stages.

In the first stage, the matrices are permuted in in order to make them look closer to (block) upper triangular form. Permutation matrices $\boldsymbol{P}_1$ and $\boldsymbol{P}_2$ are constructed such that

$$\boldsymbol{P}_1(\boldsymbol{A}, \boldsymbol{B})\boldsymbol{P}_2 = (\boldsymbol{A}', \boldsymbol{B}') = \left(\begin{bmatrix} \boldsymbol{A}'_{11} & \boldsymbol{A}'_{12} & \boldsymbol{A}'_{13} \\ 0 & \boldsymbol{A}'_{22} & \boldsymbol{A}'_{23} \\ 0 & 0 & \boldsymbol{A}'_{33} \end{bmatrix}, \begin{bmatrix} \boldsymbol{B}'_{11} & \boldsymbol{B}'_{12} & \boldsymbol{B}'_{13} \\ 0 & \boldsymbol{B}'_{22} & \boldsymbol{B}'_{23} \\ 0 & 0 & \boldsymbol{B}'_{33} \end{bmatrix} \right)$$

where $\boldsymbol{A}'_{11}, \boldsymbol{B}'_{11} \in \mathbb{R}^{(n-i_l)\times(n-i_l)}$, and $\boldsymbol{A}'_{33}, \boldsymbol{B}'_{33} \in \mathbb{R}^{(n-i_h)\times(n-i_h)}$ are upper triangular matrices. Obvious benefits from this are that the so called *isolated eigenvalues* can be read

off without any roundoff error and that the order of the eigenvalue problem is reduced to $i_h - i_l + 1$.

The second stage consists of a diagonal similarity transformation (scaling), which aims at equilibrating the row and column norms of matrices. Diagonal matrices $\boldsymbol{D}_1$ and $\boldsymbol{D}_2$ are constructed so that the matrix pair

$$\begin{aligned}\boldsymbol{D}_1(\boldsymbol{A}', \boldsymbol{B}')\boldsymbol{D}_2 &= (\boldsymbol{A}'', \boldsymbol{B}'') \\ &= \begin{bmatrix} \boldsymbol{I} & 0 & 0 \\ 0 & \boldsymbol{D}_1' & 0 \\ 0 & 0 & \boldsymbol{I} \end{bmatrix} \left(\begin{bmatrix} \boldsymbol{A}_{11}' & \boldsymbol{A}_{12}' & \boldsymbol{A}_{13}' \\ 0 & \boldsymbol{A}_{22}' & \boldsymbol{A}_{23}' \\ 0 & 0 & \boldsymbol{A}_{33}' \end{bmatrix}, \begin{bmatrix} \boldsymbol{B}_{11}' & \boldsymbol{B}_{12}' & \boldsymbol{B}_{13}' \\ 0 & \boldsymbol{B}_{22}' & \boldsymbol{B}_{23}' \\ 0 & 0 & \boldsymbol{B}_{33}' \end{bmatrix} \right) \begin{bmatrix} \boldsymbol{I} & 0 & 0 \\ 0 & \boldsymbol{D}_2' & 0 \\ 0 & 0 & \boldsymbol{I} \end{bmatrix} \end{aligned} \tag{3.7}$$

is nearly balanced. A matrix is called *balanced* in a vector norm $\|\cdot\|$ if its rows and columns norms are equal. Such a matrix pair is well conditioned and can improve the accuracy of later processing in some cases. These operations and their inverses are implemented in LAPACK [26] under the routines DGGBAL and DGGBAK respectively. It is assumed that after performing this step the matrices are rewritten into $(\boldsymbol{A}, \boldsymbol{B})$

3.3.2 Reduction of B to an Upper Triangular Matrix

This step is easily done by applying the $\boldsymbol{QR}$ decomposition to the matrix $\boldsymbol{B}$. It is in principle similar to the $\boldsymbol{QZ}$ but the coefficients of the elementary orthogonal matrices are obtained upon a polynomial. $\boldsymbol{Q}$ is an orthogonal matrix obtained as the product of elementary orthogonal matrices reducing sequentially $\boldsymbol{B}$ to the upper triangular matrix $\boldsymbol{R}$, such that $\boldsymbol{B} = \boldsymbol{QR}$. For the tranformation of the matrix pair $(\boldsymbol{A}, \boldsymbol{B})$ one obtains

$$\boldsymbol{Q}^T \cdot (\boldsymbol{A}, \boldsymbol{B}) = (\boldsymbol{Q}^T\boldsymbol{A}, \boldsymbol{R})$$

After performing this step the matrices are rewritten into $(\boldsymbol{A}, \boldsymbol{B})$

3.3.3 Reduction of the Matrix Pair to Upper Hessenberg-triangular Form

This reduction amounts to the determination of $\boldsymbol{Q}$ and $\boldsymbol{Z}$, two orthogonal matrices. The procedure has been explained in the appendix in section A.1.1. The matrix pair is reduced by elementary orthogonal transformations applied on the left as well as to the right side.

$$\boldsymbol{Q}^T(\boldsymbol{A}, \boldsymbol{B})\boldsymbol{Z} = (\boldsymbol{S}, \boldsymbol{T}) \tag{3.8}$$

where $\boldsymbol{S}$ is an upper Hessenberg matrix and $\boldsymbol{T}$ a triangular matrix. With this transformation, the generalized eigenvalues problem of order n is reduced to small generalized eigenvalues of order one or two by identification of the diagonal blocks. The algorithm for this reduction is implemented in the LAPACK routine DGGHRD.

3.3.4 Generalized Eigenvalues Determination

Refering to (A.2) of the corollary A.1.1 the determination of the eigenvalues returns to directly compute the eigenvalues if the diagonal blocks are of order one or to the computation of the eigenvalues of diagonals (2×2) blocks. This is simple, since the (2×2) diagonal blocks in $\boldsymbol{B}$ are triangular. The algorithm for this reduction is implemented in the LAPACK routine DHGEQZ.

3.3.5 Generalized Eigenvectors Determination

For each of the eigenvalues λ_n previously obtained, the homogeneous equation system

$$(\boldsymbol{A} - \lambda_n \boldsymbol{B})\boldsymbol{x}_n = 0$$

is solved and $\boldsymbol{x}_n$ is obtained as the corresponding eigenvector.

3.3.6 Unbalancing

The solutions of the initial problem are obtained by applying the inverse of the balancing operation introduced in the first step in section (3.3.1). This operation is performed by the LAPACK routine DGGBAK.

3.4 C/C++ Programming of the Generalized Eigenvalues Problem Algorithm and Test

3.4.1 Programming

For confidentiality reasons the source code will not be presented in the scope of this work. The generalized eigenvalues solver program is structured following the steps presented in section 3.3 and makes use of routines available in the LAPACK library.

3.4.2 Test Example

In this example, the Numerical Electromagnetic Code (NEC2) software is the electromagnetic simulation environment exploited to derive the impedance matrix. NEC2 is based on the method of moments (MoM) and works with the *point matching* principle as indicated in section 3.1.

A $1\,\mathrm{m}$ wire with $1\,\mathrm{mm}$ radius and 45 equidistant *meshing points* is irradiated with plane waves at $300\,\mathrm{MHz}$ polarized in such a way that the electrical field has the same direction

as the wire. The impedance matrix $\boldsymbol{Z}$ is drawn from NEC2 and its real and imaginary part $\boldsymbol{R}$ and $\boldsymbol{X}$ respectively, are submitted to the eigenvalue solver. As results, the amplitudes of the first 4 right eigenvectors are represented with respect to the discretized wire.

The following table presents the eigenvectors as shown in Fig. 3.1 and Fig. 3.2 and their corresponding eigenvalues. The eigenvalue closest to zero, $\lambda_1 = 0.631$ corresponds to the

Eigenvectors	(a)	(b)	(c)	(d)
Eigenvalues	$\lambda_0 = 3.26$	$\lambda_1 = 0.631$	$\lambda_2 = -59.4$	$\lambda_3 = -1.73e+03$

Table 3.1: First (a), second (b), third (c) and fourth (d) right eigenvector as represented in Figures 3.1 and 3.2 and their corresponding eigenvalues.

eigenvector with distribution similar to that of a λ-resonance. This is in fact not surprising since the excitation frequency was chosen as $300\,\mathrm{MHz}$.
It should be specified that performing the same simulation at $150\,\mathrm{MHz}$ yields an approximately zero eigenvalue for the eigensolution corresponding actually to (a). The eigenvalue $\lambda_0 = 3.26$ corresponds to (a) the eigenvector with distribution close to that of a $\lambda/2$-resonance current density.

The eigenvalues λ_2 and λ_3 correspond to eigensolutions with distribution close to that of

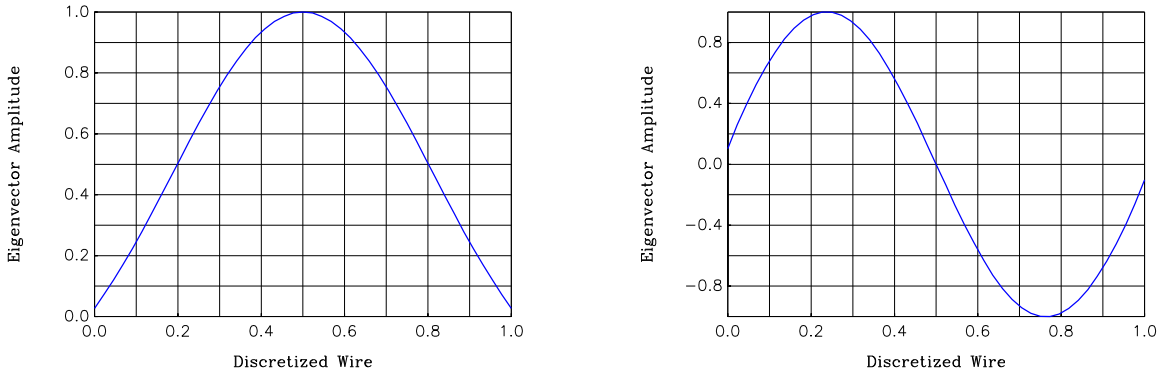

(a) (b)

Figure 3.1: First (a) and second (b) right eigenvector amplitudes on the discretized wire.

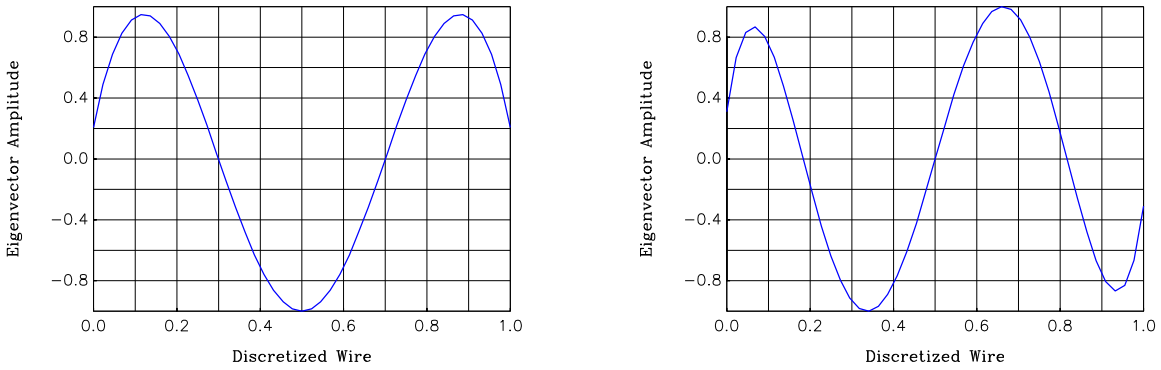

(c) (d)

Figure 3.2: Third (c) and fourth (d) right eigenvector amplitude on the discretized wire.

a $3\lambda/2$- and 2λ-resonance current densities respectively.
Modes obtained as solutions complied fully with the expectations of natural inherent modes.

Chapter 4

Radiation Properties of Mobile Phones Chassis

Results obtained in this chapter have been object of a publication [12]. This chapter gives more details and emphasizes some aspects of results presented and not really elucidated in the published paper.

To provide an insight into the coupling mechanism between antenna element and chassis, we pursue in the same idea as already mentioned in previous chapters. Namely by considering chassis and antenna element as two distintive entities and investigate the radiation properties of the chassis on its own. In this chapter we numerically investigate the resonance frequency and radiation quality factor of mobibe phones chassis by making use of the theory of characteristic modes for conducting bodies. Simulations are performed for *Bar-Types* and *Folder-Types* mobile phones as application examples, where in an initial phase, chassis in generic geometries are considered to be perfectly conducting.

4.1 Chassis Eigenresonant Modes and frequencies

The theory of characteristic modes is governed by equation (3.1) where $\boldsymbol{J}_{\mathrm{s},n}$ and $\lambda_n(\omega)$ completely determine the n^{th} characteristic mode. Its associated radiated power can be obtained by making use of the Poynting's theorem as follows:

$$\langle \boldsymbol{J}_{\mathrm{s},n}{}^*, \widehat{\mathbf{Z}}\boldsymbol{J}_{\mathrm{s},n}\rangle = \iint\limits_S \boldsymbol{E}_n \times \boldsymbol{H}_n{}^* \cdot \,\mathrm{d}s + \mathrm{j}\omega \iiint\limits_V \left(\mu \boldsymbol{H}_n \cdot \boldsymbol{H}_n{}^* - \epsilon \boldsymbol{E}_n \cdot \boldsymbol{E}_n{}^*\right) \mathrm{d}v \quad (4.1)$$

where $\boldsymbol{E}_n$ and $\boldsymbol{H}_n$ are electrical and magnetic fields respectively generated by $\boldsymbol{J}_{\mathrm{s},n}$ and S a surface chosen coincident with the surface of the chassis and insiding the volume V.

$$(1 + \mathrm{j}\lambda_n)\langle \boldsymbol{J}_{\mathrm{s},n}{}^*, \widehat{\mathbf{R}}\boldsymbol{J}_{\mathrm{s},n}\rangle = 2P_n + 4\mathrm{j}\omega\left(\langle W_{\mathrm{mag},n}\rangle - \langle W_{\mathrm{el},n}\rangle\right) \quad (4.2)$$

where $\langle W_{\mathrm{mag},n} \rangle$ and $\langle W_{\mathrm{el},n} \rangle$ are modal time averages of the stored magnetic and electric field energies respectively. This leads by identifying the real and imaginary parts in (4.2) to

$$\lambda_n = 2\omega \frac{\langle W_{\mathrm{mag},n} \rangle - \langle W_{\mathrm{el},n} \rangle}{P_n} \tag{4.3}$$

It can be drawn from this expression of $\lambda_n(\omega)$ that frequencies ω_0 for which $\lambda_n(\omega_0) \approx 0$ are *eigenresonant frequencies* and their corresponding eigenvectors are *eigenresonant modes* of the chassis, since at those frequencies the time average stored magnetic and electric energy are equal ($\langle W_{\mathrm{mag},n} \rangle = \langle W_{\mathrm{el},n} \rangle$). These chassis eigenresonant frequencies can also be referred to as chassis resonant frequencies since as we will later see their corresponding eigenresonant modes dominate the overall radiation properties.
The numerical evaluation of eigenresonant frequencies and corresponding resonant modes involves first the choice of a frequency range of interest. This range should contain a rough estimation of the resonant frequency of the conducting body under study (here the mobile phones chassis). Otherwise equation (3.4) might be unstable with results providing no physical interpretation.

4.2 Numerical Evaluation of Chassis Radiation Properties

Simulations can be performed with MoM based electromagnetic sofwares. Simulations performed in the scope of this work are done with the CONCEPT II software [27], which gives an easy access to the impedance matrix, key solution for the determination of characteristic modes.
The numerical evaluation of chassis radiation properties includes in a first time three main steps.

- In the first step, the chassis generic geometry model is designed and simulated in the MoM based electromagnetic software environment at a frequency of interest. Plane waves are used for excitation to prevent from an eventual influence of the source location on the expected results.

- In the second step, the system or impedance matrix generated by the simulation in the previous step is extracted and placed at the disposal of the generalized eigenvalues solver developed and presented in the previous chapter.

- The third step consists in the computation of characteristic modes and results interpretation. For the latter, solutions of interest are returned into the MOM based electromagnetic sofware environment for different representations.

Evaluation of radiation properties requires a family of frequencies in an interested range. For each single frequency in the family, previous steps in the indicated order are to be performed. Out of results obtained resonance frequencies can be easily identified. A much more complicated task is the evaluation of the radiation quality factor therefore one establishes a relation between frequencies and eigenvalues by correlating eigenvectors at adjacent frequencies.

4.3 Chassis Modal Radiation Quality Factor

The chassis bandwidth contribution in the overall bandwith of the mobile device is of high interest. Evaluation of the bandwidth is performed here through the radiation quality factor, which is its inverse.
The radiation quality factor Q_{rad} of a system is defined [28] to be 2π times the ratio of the maximum energy stored to the total energy lost per period. A generally accepted definition of the *radiation quality factor* for antennas can be expressed as follows:

$$Q_{\mathrm{rad}} = 2\omega \frac{\max(\langle W_{\mathrm{mag}} \rangle, \langle W_{\mathrm{el}} \rangle)}{P_{\mathrm{rad}}} \tag{4.4}$$

where $\langle W_{\mathrm{mag}} \rangle$ and $\langle W_{\mathrm{el}} \rangle$ are time averages of the stored magnetic and electric field energies respectively, ω denotes the radian frequency and P_{rad} the radiated power.

Considering the chassis of a device in mobile communication as part of the antenna, it is of high interest to evaluate its radiation quality factor on its own. This makes possible to know its contribution in the overall radiation quality factor of the device. Obviously, the radiation quality factor of the chassis is determined by that of modes governing its radiation, which are modes close to or at resonances. Since the n^{th} mode is completely determined by the knowledge of its eigenvalue λ_n and eigenvector $\boldsymbol{J}_{\mathrm{s},n}$, a familiar definition of the radiation quality factor based on the *steepness of the phase about resonance* [29] pages 42-44,

$$Q_{\mathrm{s},n} = \omega_n \left| \frac{\mathrm{d}\lambda_n}{\mathrm{d}\omega} \right|_{\omega=\omega_n} \tag{4.5}$$

is arrived at by taking the derivative of the eigenvalue with respect to the frequency.
In fact, as stated in [29] for a resonator, a comparative inspection shows that the expression of the n^{th} eigenvalue $\lambda_n(\omega)$ as specified in (4.3) represents the radiation quality factor based on the *phase angle*. The definition of the radiation quality factor based on the *steepness of the phase about resonance* [29] involves the derivative of the radiation quality factor based on the phase angle.
Application of the relation between both definitions of the radiation quality factor clearly justifies the above equation (4.5), applied here in the context of chassis resonant modes.

Although the quality factor calculated according to definitions (4.4) or (4.5), respectively are not identical, a useful interrelation exists.

To estabilised the relation between (4.4) and (4.5), the approach presented here is similar to that proposed in [30]. It is assumed in what follows, that the calculations are confined in the complex frequency plane, where $\tilde{s} = \alpha + \mathrm{j}\omega$ defined a complex frequency. Assuming the n^{th} chassis mode generated by a source fed by a transmission line, (4.1) can be rewritten in the complex plane as follows:

$$\frac{1}{2}\check{V}(\tilde{s})\check{I}^{*}(\tilde{s}) = \check{P}_n + 2\mathrm{j}\omega\left(\langle\check{W}_{\mathrm{mag},n}\rangle - \langle\check{W}_{\mathrm{el},n}\rangle\right) + 2\alpha\left(\langle\check{W}_{\mathrm{mag},n}\rangle + \langle\check{W}_{\mathrm{el},n}\rangle\right) \tag{4.6}$$

where the symbol $\check{}$ embellishes the quantities in the complex plane to distinguish them from the corresponding quantities in the frequency domaine. Dividing (4.6) by $|I(\tilde{s})|^2$ one obtains the complex impedance

$$\check{Z}_n(\tilde{s}) = \check{R}_n(\alpha,\omega) + \mathrm{j}\check{X}_n(\alpha,\omega) \tag{4.7}$$

where

$$\check{R}_n(\alpha,\omega) = \frac{2\check{P}_n + 4\alpha\left(\langle\check{W}_{\mathrm{mag},n}\rangle + \langle\check{W}_{\mathrm{el},n}\rangle\right)}{|I(\tilde{s})|^2} \tag{4.8}$$

and

$$\check{X}_n(\alpha,\omega) = \frac{4\omega\left(\langle\check{W}_{\mathrm{mag},n}\rangle - \langle\check{W}_{\mathrm{el},n}\rangle\right)}{|I(\tilde{s})|^2} \tag{4.9}$$

In the following, α is assumed to be sufficiently small in such a way that $I(\tilde{s}) \approx I$ which is independent of α. The complex impedance is an analytic function, thus its real and imaginary parts satisfy the Cauchy-Riemann conditions,

$$\frac{\partial\check{R}_n(\alpha,\omega)}{\partial\alpha} = \frac{\partial\check{X}_n(\alpha,\omega)}{\partial\omega} \tag{4.10}$$

and

$$\frac{\partial\check{X}_n(\alpha,\omega)}{\partial\omega} = -\frac{\partial\check{X}_n(\alpha,\omega)}{\partial\alpha} \tag{4.11}$$

One obtains from (4.10)

$$\frac{\partial X_n}{\partial\omega} = \frac{\partial\check{X}_n(\alpha,\omega)}{\partial\omega}\bigg|_{\alpha=0} = 4\frac{\langle W_{\mathrm{mag},n}\rangle + \langle W_{\mathrm{el},n}\rangle}{|I|^2} \tag{4.12}$$

which is the **Foster reactance theorem** for antennas. Solving (4.12) and (4.9) (under the condition $\alpha = 0$) as an equation system with respect to $\langle W_{\mathrm{mag},n} \rangle$ and $\langle W_{\mathrm{el},n} \rangle$ yields

$$\begin{aligned} \langle W_{\mathrm{mag},n} \rangle &= \frac{|I|^2}{8} \left(\frac{\partial X_n}{\partial \omega} + \frac{X_n}{\omega} \right) \\ \langle W_{\mathrm{el},n} \rangle &= \frac{|I|^2}{8} \left(\frac{\partial X_n}{\partial \omega} - \frac{X_n}{\omega} \right) \end{aligned} \tag{4.13}$$

By making use of (4.13), the radiation quality factor as introduced in (4.4) can be expressed for the n^{th} mode as follows:

$$Q_{\mathrm{rad},n} = \frac{|I|^2}{4} \frac{\left(\omega \frac{\partial X_n}{\partial \omega} \pm X_n \right)}{P_n} = \frac{1}{2} \left(\omega \frac{\mathrm{d}\lambda_n}{\mathrm{d}\omega} \pm \lambda_n \right) \tag{4.14}$$

For modes at resonance ($\lambda_n(\omega_n) = 0$) one obtains from (4.14) and (4.5) the interrelation

$$|Q_{\mathrm{rad},n}| = \frac{1}{2} \omega_n \left| \frac{\mathrm{d}\lambda_n}{\mathrm{d}\omega} \right|_{\omega=\omega_n} = \frac{1}{2} Q_{\mathrm{s},n} \tag{4.15}$$

The numerical evaluation of a modal radiation quality factor $Q_{\mathrm{s},n}$ is associated to the evaluation of its slope in a frequency region of interest. In the present case we are interested in resonant frequency regions. These regions can be localized from the simulations perfomed in section 4.1 since for a familly of frequency samples corresponding eigenvalues have been computed. A root-finding algorithm is then applied on these regions to accurately determine the resonance frequency and furthermore evaluate the radiation quality factor. An appropriate algorithm for this purpose is the well-known *secant method* [31] which simultaneously evaluates the root and the slope at the root's position.

4.4 Application Examples

4.4.1 Bar-Type Phone Structure

For the so-called Bar-Type or Monoblock mobile devices widely spread on the market, the Printed Circuit Board (PCB) considered as the ground plane has a rectangular form. A perfectly conductive metallic rectangular board is thus considered as model for simulation. The battery and other parts of the housing are ignored and its dimensions are $100\,\mathrm{mm} \times 40\,\mathrm{mm}$. Fig. 4.1 shows the frequency dependence of the eigenvalues λ_n with magnitude less than 10 in the frequency range from $820\,\mathrm{MHz}$ to $4820\,\mathrm{MHz}$. The graphs are constructed based on the correlation between eigenvectors at adjacent frequency samples

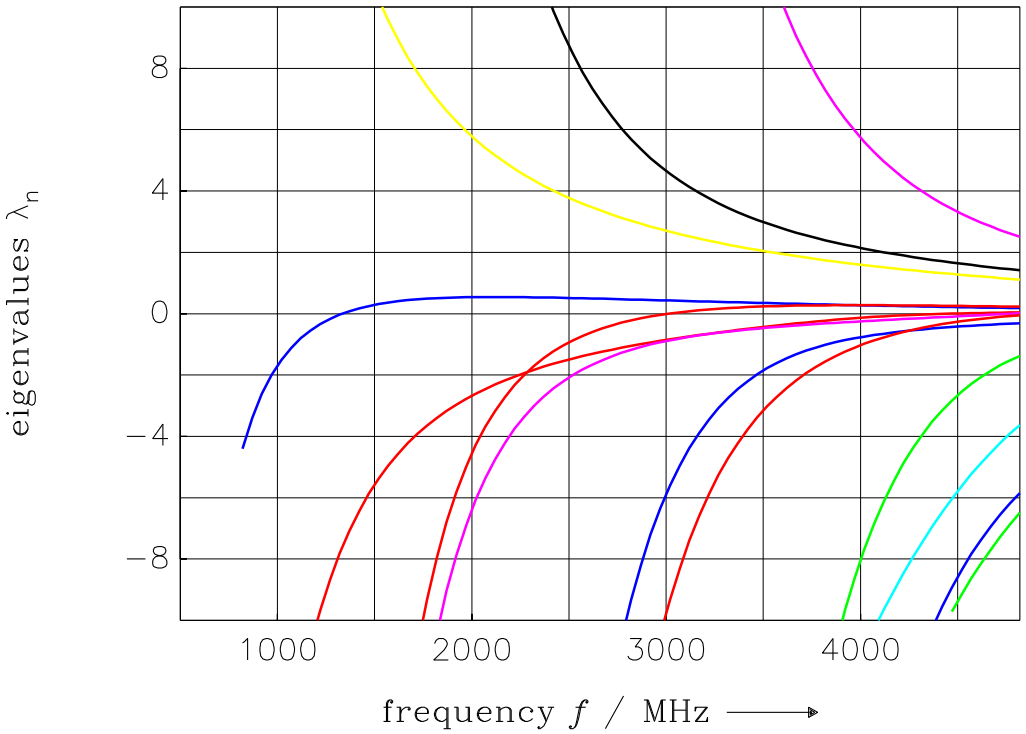

Figure 4.1: Frequency dependence of the first few eigenvalues for a $100\,\mathrm{mm} \times 40\,\mathrm{mm}$ board.

as previously mentioned. According to the discussion in section 4.1, eigenresonant modes are of high interest. Four resonances ($\lambda_n(\omega) = 0$) can be observed in the given frequency range.

Entries (A-D) in Table 4.1 show resonance frequencies and radiation quality factors at resonances according to equation 4.15. λ_1 and λ_2 represents the eigenvalues respectively, of the second and third order modes and should specify the degree of their contributions to the averall radiation properties. The corresponding modes are refered to as (A) $\rightarrow$ (D) in the sequel. The associated current densities are shown in Fig. 4.2, where the colors are associated to the current magnitude (red and green represent respectively, maximum and minimum) and the direction of the arrows related to the phase. (A) and (B) represents a half-wavelength and a wavelength resonance around the major axis respectively. Obvious similarities between the first (a), the second (b) order current mode shown in Fig. 3.1 for a simple wire and the eigensolutions (A) and (B) respectively, should be observed. (A) and (B) are dipole modes with respect to the major axis, which dominate at their respective frequencies the radiation properties. This can be easily observed on their radiation patterns,

label	$f_0/\,\mathrm{MHz}$	$Q_{\mathrm{rad},0}$	λ_1	λ_2
(A)	1334	2.9	-7.60	13.80
(B)	3012	2.4	0.42	-0.83
(C)	4455	0.7	-0.10	0.22
(D)	4780	1.5	0.04	-0.07

Table 4.1: The first 4 characteristic mode resonances, their corresponding radiation quality factors together with the 2^{nd} and 3^{th} order modes eigenvalues.

which once more show similarities with that of a dipole. (C) shows a half-wavelength resonance and clearly represents a dipole mode around the minor axis with an average half-wave current path length of $34\,\mathrm{mm}$.
(D) is a superposition of half-wavelength resonances around the major and minor axis and the average half-wave current path length is evaluated at $31\,\mathrm{mm}$. This mode represents a quadrupole mode.
According to Fig. 4.1 a vertical straight through a given frequency intersects the eigenvalues at different points representing orthogonal eigenmodes. We refer this orthogonality to as *vertical orthogonality*. The question arising from observations of radiation patterns at different resonance frequencies is that of their orthogonality. This can be refered to as *horizontal orthogonality*, since patterns orthogonality shall be investigated at different resonance frequencies. This question, which might be high interesting in the perspective of multiband antenna design on small plate-forms based on characteristic modes, is not handled in the scope of this work and certainly will be a topic for future research.
It is interesting to notice in Fig. 4.1 that the low order eigensolutions change only very slowly with respect to the frequency and can in fact be considered almost constant along each graph. The availability of four orthogonal modes with eigenvalues of magnitude less than or around 2 in the $2.4\,\mathrm{GHz}$ ISM band is an interesting observation for the design of MIMO antenna systems on the mobile phones.

4.4.2 Folder-Type Phone Structure

Folder-Type mobile Phones or Clam-Shell phones are widespread in the market. For the analysis of the radiation properties of its chassis, two cases are to be considered: the open and closed states of the device. As already done in the previous section, a perfectly conducting chassis is assumed in the simulations. We first investigate the resonant characteristic

(A)

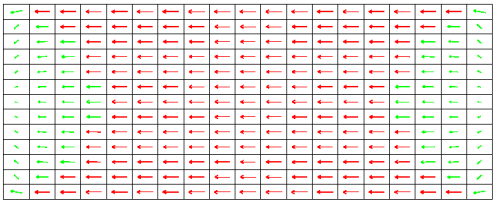

(B)

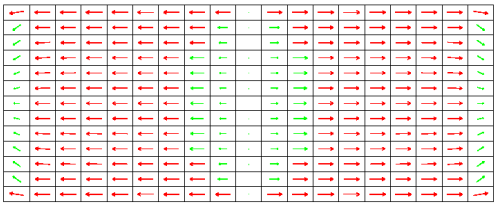

(C)

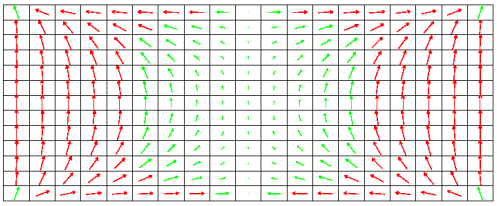

(D)

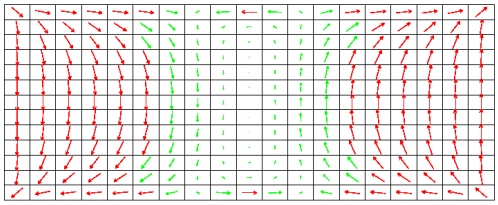

Figure 4.2: Surface current densities for characteristic mode resonances at frequencies as indicated in Table 4.1.

modes in open state.

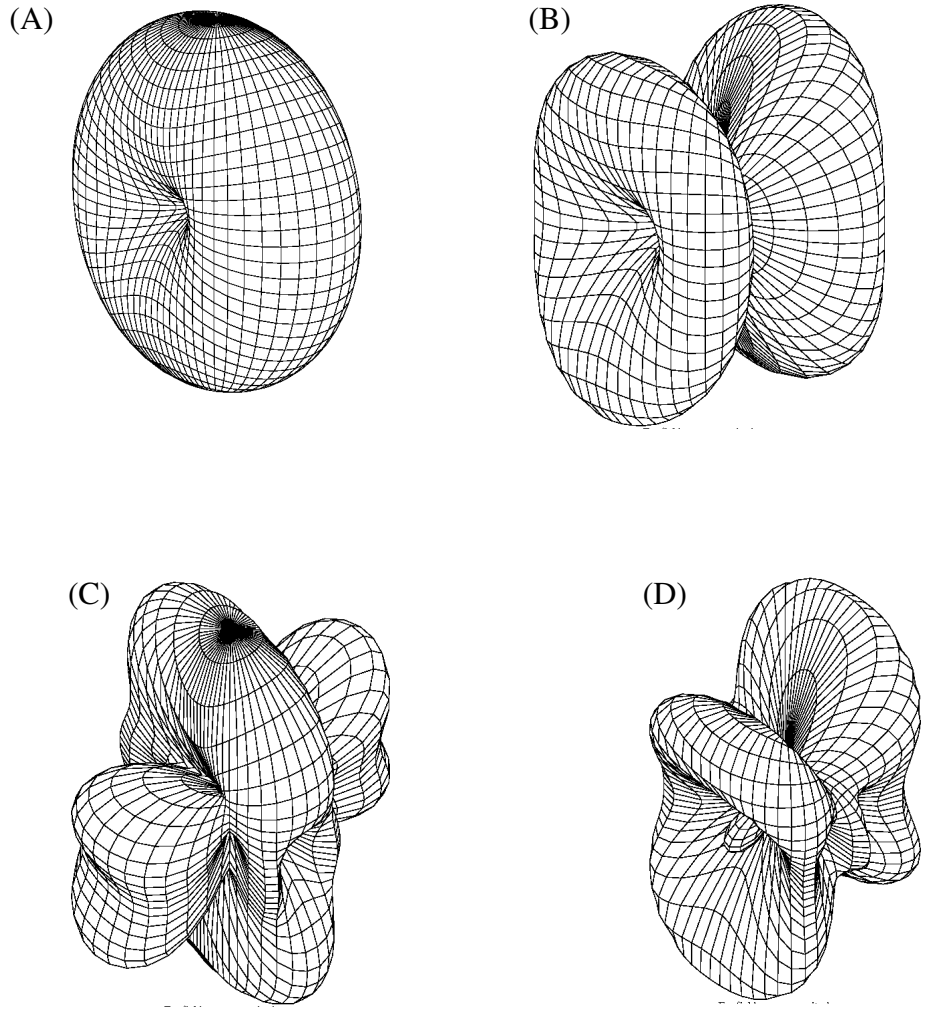

Figure 4.3: Radiation Patterns for Characteristic Mode Resonances According to Fig. 4.2

Clam-Shell Phone in Opened State

The base part is modeled as a $70\,\mathrm{mm} \times 40\,\mathrm{mm}$ and the flip part as a $50\,\mathrm{mm} \times 40\,\mathrm{mm}$ metallic plate connected to the base by a conductive plate with height $15\,\mathrm{mm}$. Fig. 4.4 shows the frequency dependence of the eigenvalues λ_n with magnitude less than 10 in the frequency range from $820\,\mathrm{MHz}$ to $4820\,\mathrm{MHz}$. The graphs as already mentioned are constructed based on the correlation between eigenvectors at adjacent frequency samples.

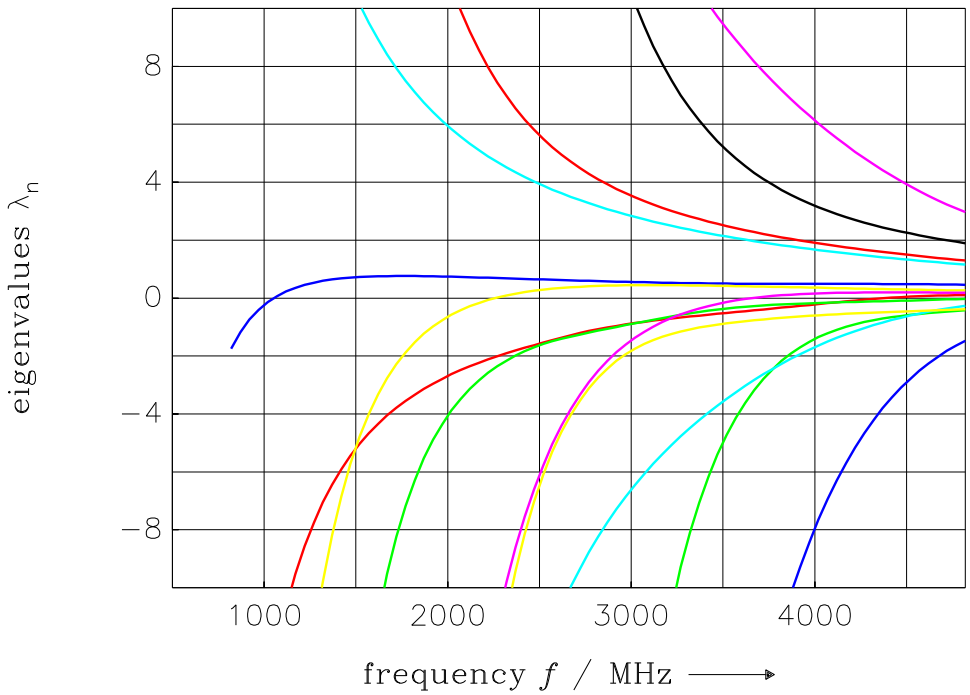

Figure 4.4: Frequency dependence of the first few eigenvalues for a folder type phone in open state.

Four resonances ($\lambda_n(\omega) = 0$) are observed in the given frequency range, which are tabulated in Table 4.2. Entries (E-H) show resonance frequencies, radiation quality factors as

label	f_0/ MHz	$Q_{\mathrm{rad},0}$	λ_1	λ_2
(E)	1052	3.69	-12.49	22.72
(F)	2257	3.36	0.69	-2.03
(G)	3661	2.75	-0.28	0.40
(H)	4384	1.74	-0.10	0.19

Table 4.2: The first 4 characteristic mode resonances, their corresponding radiation quality factors together with the 2^{nd} and 3^{th} order eigenvalues for a folder type phone in open state.

well as second and third order eigenvalues. The associated current densities are represented in Fig. 4.5
(E) is easily identified as a half-wave resonance mode with respect to the major axis. Inspection of λ_1 and λ_2 shows a great domination of this dipole mode. Remark that its resonance frequency is closed to the operating range of GSM 900. With an appropriate mechanism this frequency can be tuned into interested range.
(F) is identified as a full-wave resonance mode with respect to the major axis. Low values of λ_1 and λ_2 indicate very good radiation characteristics for modes of 2^{nd} and 3^{th} order. Observe that the mode of order 2 is almost resonant. One should take benefit from these properties for the design of multiple antennas systems. (G) and (H) show a $3/2$-wave resonance along the major axis and a half-wave resonance with respect to the minor, respectively. An interesting observation is the 2^{nd} and 3^{th} order eigenvalues which are approximately zero in both cases. This means that those modes can be potentially as well excited as the resonant ones at their respective frequencies and shall exhibit almost equivalent radiation characteristics.
The characteristic radiation patterns corresponding to resonance modes shown in Fig. 4.5 are represented in Fig. 4.6

4.4.3 Clam-Shell Phone in Closed State

Simulations for clam-shell phone in closed state are performed with a perfectly conductive chassis having the same dimensions as in the opened state. Fig. 4.7 shows the frequency dependence of the eigenvalues λ_n with magnitude less than 10 in the frequency range from $820\,\mathrm{MHz}$ to $4820\,\mathrm{MHz}$.
Four resonances ($\lambda_n(\omega) = 0$) are observed in the given frequency range, which are confined in Table 4.3.
The first resonance (I) is easily identified as that of a shorted quater-wave parallel plate resonator which explains its high radiation quality factor. The current density (J) represents a half wave dipole mode resonance about the major axis. It has a remarkably low quality factor, indicating that this structure permits large bandwidth over the DCS, PCS and UMTS bands. The transverse half-wave resonance (K) again yields poor radiation, due to counter-oriented currents on the base and flip part. (L) also represents a transverse resonance with counter-oriented current on the base and flip, which consequently yields poor radiation as indicated in the table.
Entries (I-L) represent resonance frequencies, radiation quality factor as well as the second and third order eigenvalues. The associated current densities are given in Fig. 4.8. The second and third order modes are approximately resonant since the corresponding eigenvalues are close to zero. This means that these modes at their respective frequencies can be as well

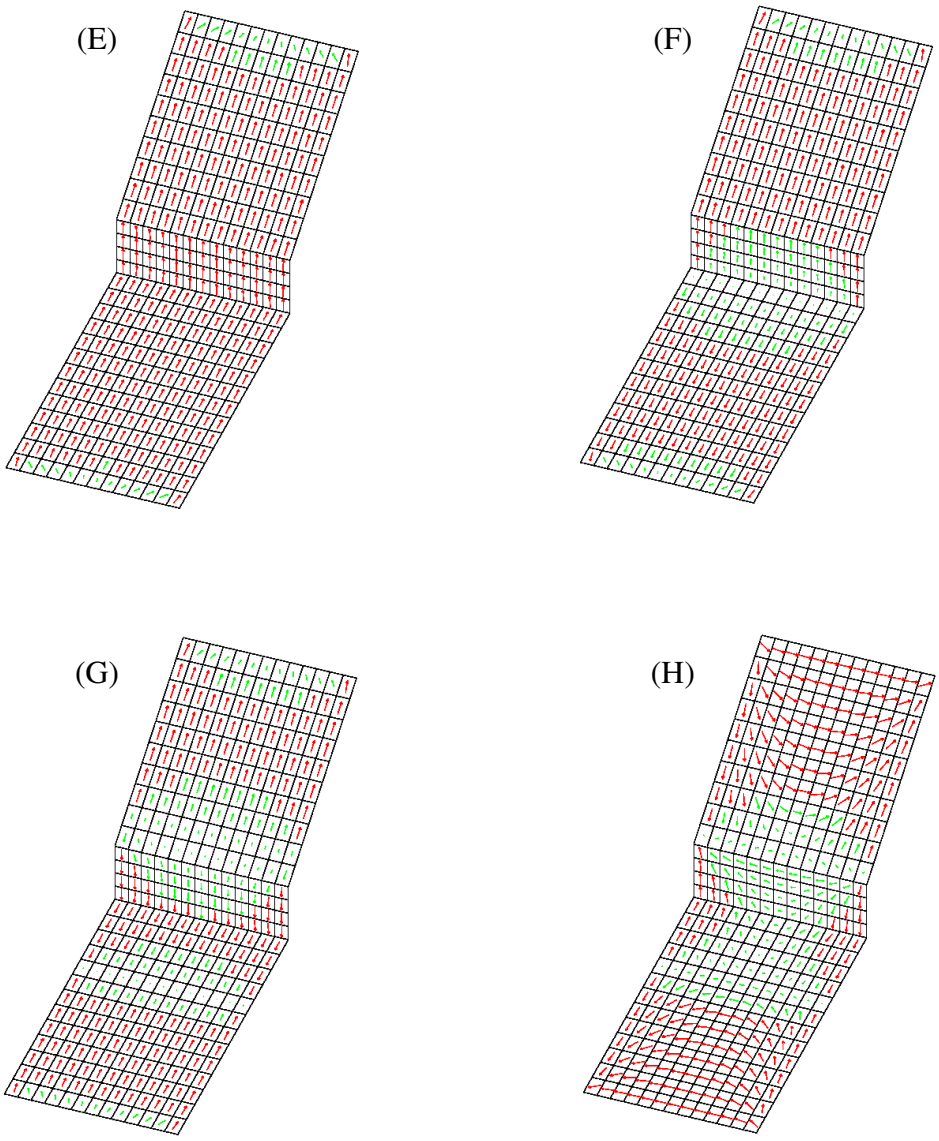

Figure 4.5: Surface current densities for characteristic mode resonances at frequencies as indicated in Table 4.2.

excited as resonant ones. One could take advantage from these to design highly perfomant

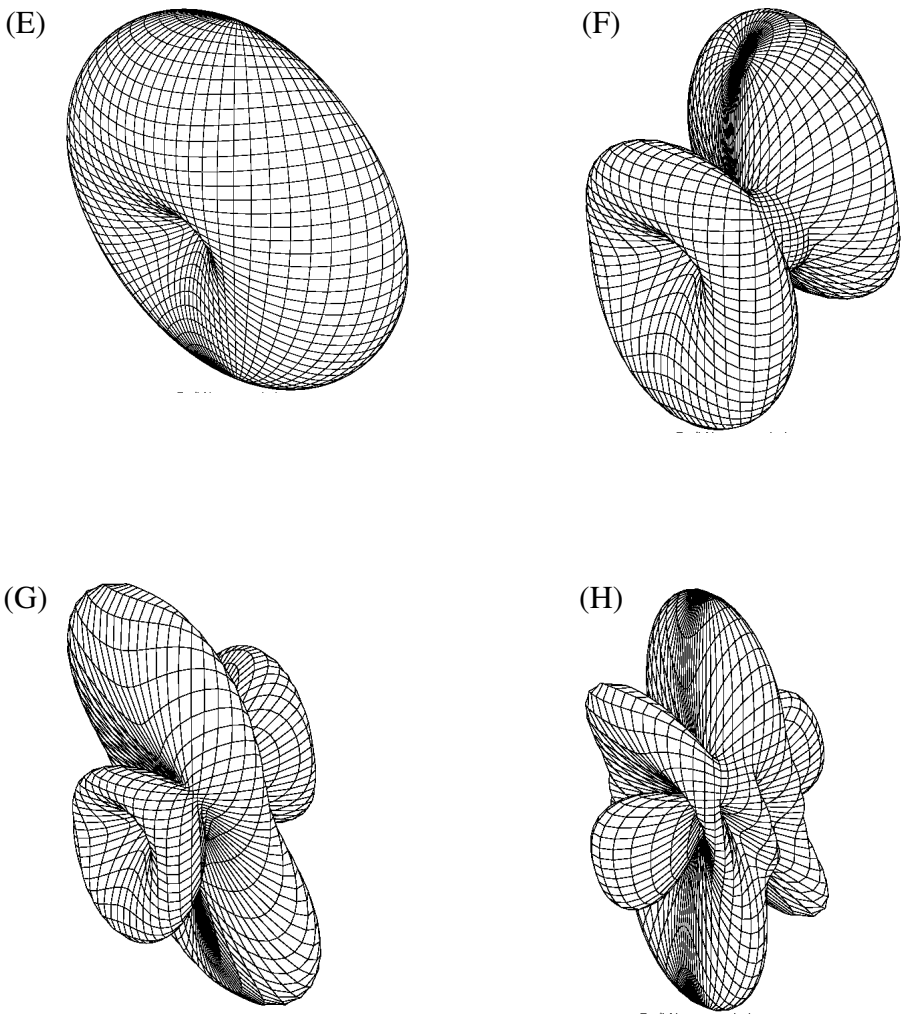

Figure 4.6: Radiation Patterns for Characteristic Mode Resonances According to Fig. 4.5.

multiple antennas systems.
The radiation patterns corresponding to the current densities (I) , (J), (K) and (L) as shown in Fig. 4.8 are presented in Fig. 4.9

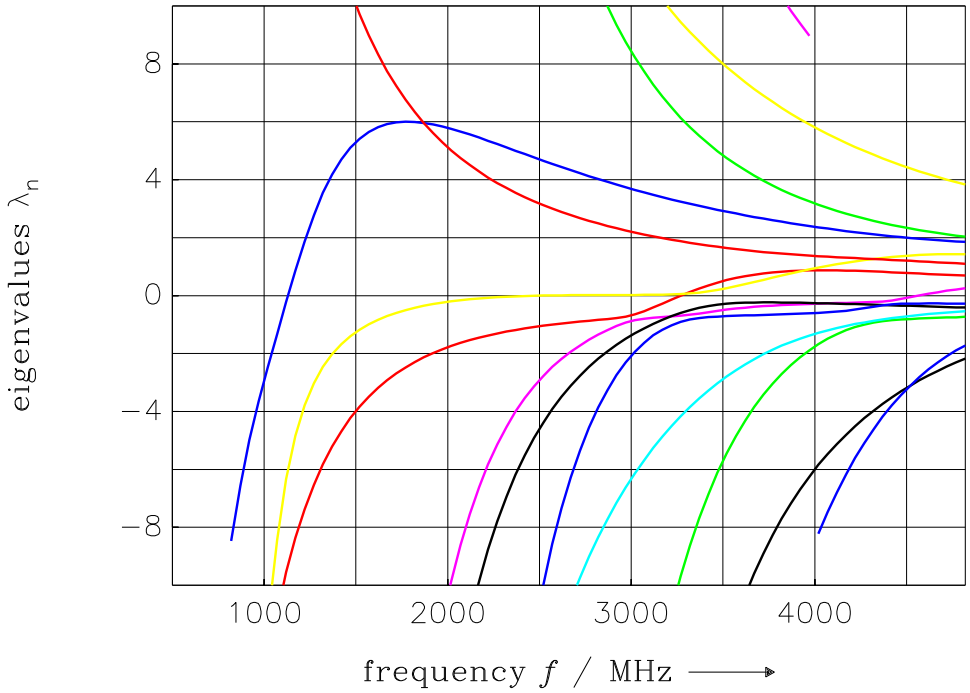

Figure 4.7: Frequency dependence of the first few eigenvalues for a folder type phone in closed state.

label	f_0/ MHz	$Q_{\mathrm{rad},0}$	λ_1	λ_2
(I)	1131	24.08	-5.96	-9.27
(J)	2508	0.32	-1.05	-2.86
(K)	3272	8.38	0.06	-0.59
(L)	4567	5.13	-0.27	-0.36

Table 4.3: The first 4 characteristic mode resonances, their corresponding radiation quality factors together with the 2^{nd} and 3^{th} order eigenvalues for a mobile phone in closed state.

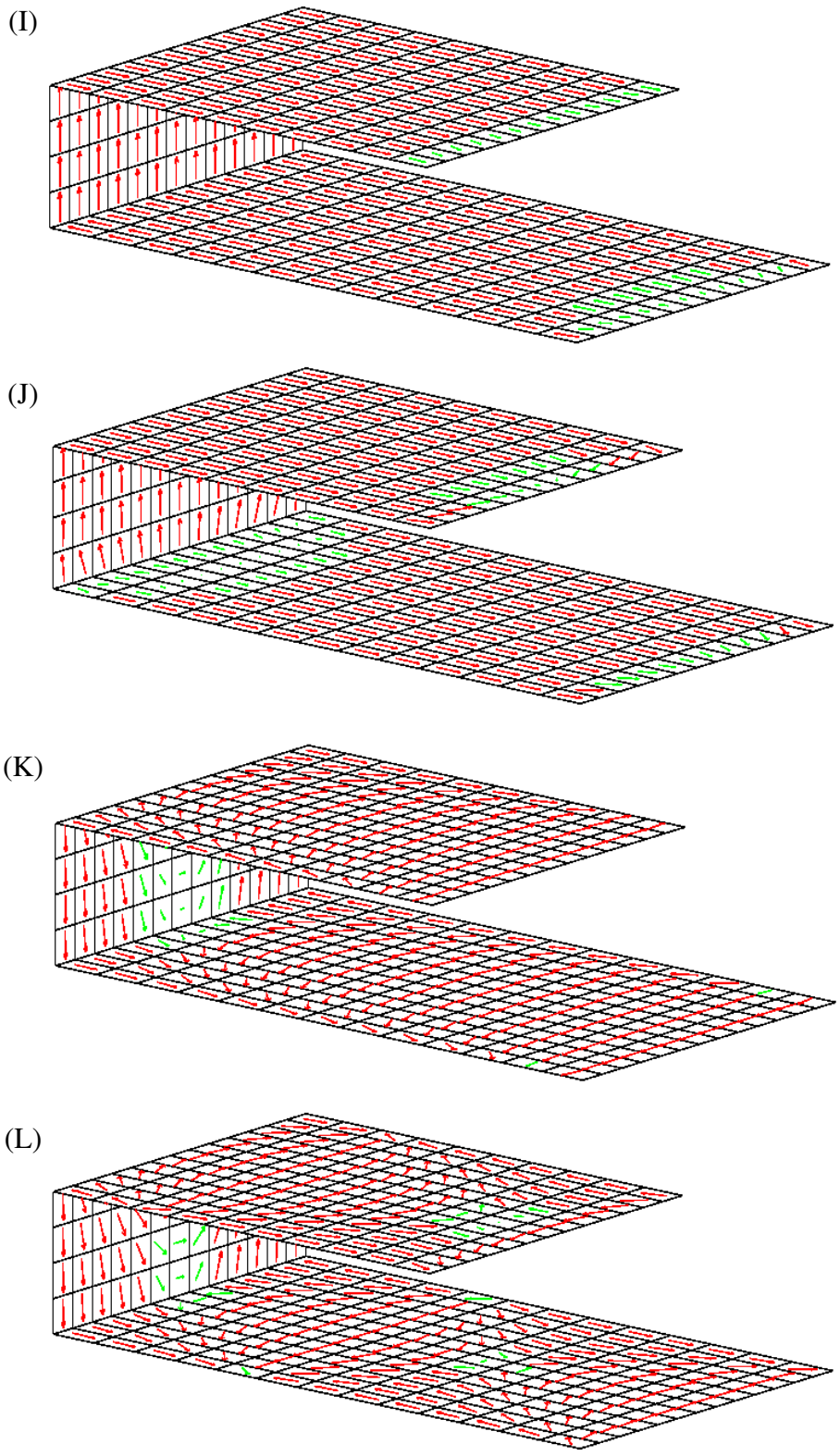

Figure 4.8: Surface current densities for characteristic mode resonances at frequencies as indicated in Table 4.3.

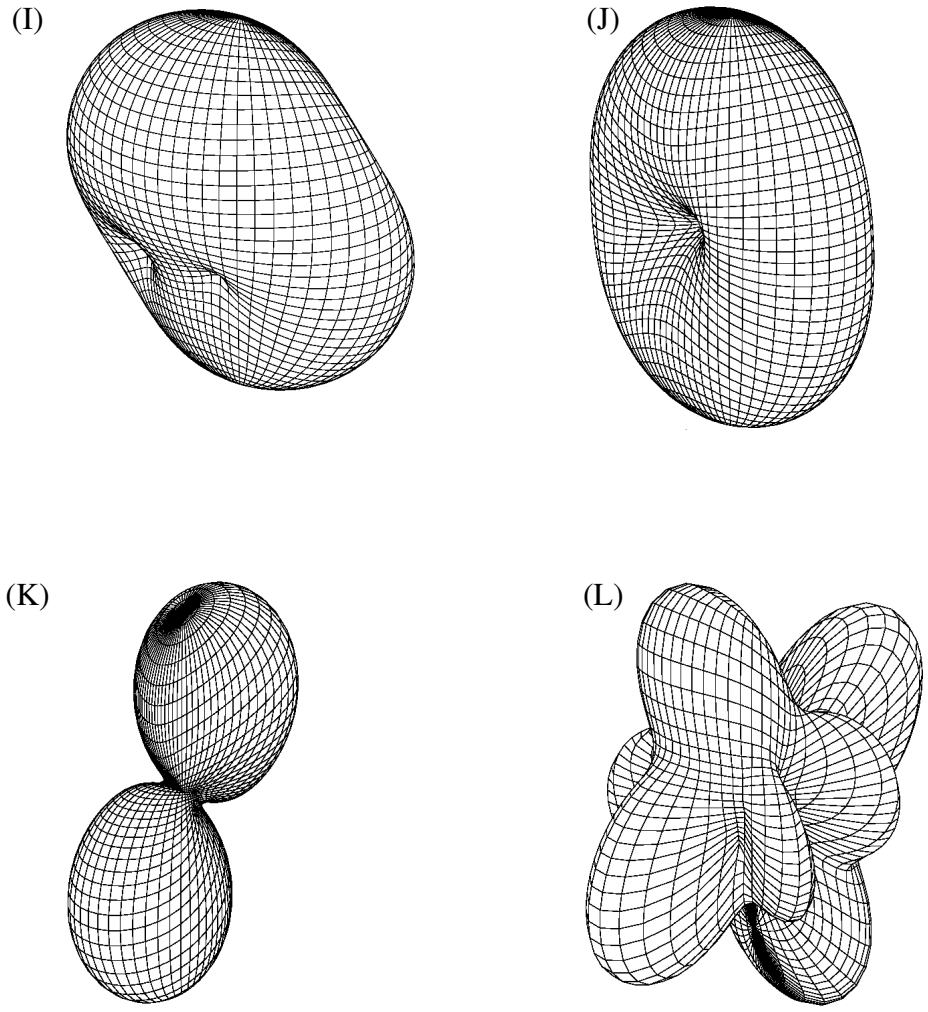

Figure 4.9: Radiation Patterns for Characteristic Mode Resonances According to Fig. 4.8.

Chapter 5

Antenna-Chassis Coupling

Results presented in this chapter have been object of a publication [32]. Further details on published results are provided in this chapter to clearly elucidate some aspects neglected in the paper.

5.1 Modal Decomposition of Current Densities

An electric external field $\boldsymbol{E}^{\mathrm{ex}}$ induces on a conducting body an electric current density $\boldsymbol{J}_{\mathrm{s}}$, which is conceived as a superposition of electrical characteristic modes $\boldsymbol{J}_{\mathrm{s},n}$

$$\boldsymbol{J}_{\mathrm{s}} = \sum_m \alpha_m \boldsymbol{J}_{\mathrm{s},m} \tag{5.1}$$

where α_n are coefficients to be determined and should describe the degree of excitation of the mode $\boldsymbol{J}_{\mathrm{s},n}$ by the external field. Computing the following product by making use of the linearity of the operator $\widehat{\mathbf{Z}}$ and the modal orthogonality relations yields,

$$\begin{aligned}
\langle \boldsymbol{J}_{\mathrm{s},n}, \widehat{\mathbf{Z}}\boldsymbol{J}_{\mathrm{s}} \rangle &= \sum_m \alpha_m \langle \boldsymbol{J}_{\mathrm{s},n}, \widehat{\mathbf{Z}}\boldsymbol{J}_{\mathrm{s},m} \rangle \\
&= \sum_m \alpha_m \left(\langle \boldsymbol{J}_{\mathrm{s},n}, \widehat{\mathbf{R}}\boldsymbol{J}_{\mathrm{s},m} \rangle + \mathrm{j} \langle \boldsymbol{J}_{\mathrm{s},n}, \widehat{\mathbf{X}}\boldsymbol{J}_{\mathrm{s},m} \rangle \right) \\
&= \sum_m \alpha_m \langle \boldsymbol{J}_{\mathrm{s},n}, \widehat{\mathbf{R}}\boldsymbol{J}_{\mathrm{s},m} \rangle (1 + \mathrm{j}\lambda_m) \\
&= 2\alpha_n P_n (1 + \mathrm{j}\lambda_n)
\end{aligned} \tag{5.2}$$

where $P_n = \frac{1}{2}\langle \boldsymbol{J}_{\mathrm{s},n}, \widehat{\mathbf{R}}\boldsymbol{J}_{\mathrm{s},n}\rangle$ is the power radiated by the n^{th} mode. Substitution of the boundary condition relation $\widehat{\mathbf{Z}}\boldsymbol{J}_{\mathrm{s}} = \boldsymbol{E}^{\mathrm{ex}}_{\tan}$ in (5.2) yields for (5.1)

$$\boldsymbol{J}_{\mathrm{s}} = \sum_m \frac{\langle \boldsymbol{J}_{\mathrm{s},m}, \boldsymbol{E}^{\mathrm{ex}}_{\tan}\rangle}{(1+\mathrm{j}\lambda_m)2P_m}\boldsymbol{J}_{\mathrm{s},m} \tag{5.3}$$

Inspection of (5.3) suggests that, for an effective excitation of the m^{th} mode, a maximization of the m^{th} modal expansion coefficient is required. This logically implies the maximization of the nominator term $\langle \boldsymbol{J}_{\mathrm{s},m}, \boldsymbol{E}^{\mathrm{ex}}_{\tan}\rangle$ also called *excitation coefficient*[14] and the minimization of the denominator term $1+\mathrm{j}\lambda_m$. The minimization of the denominator obviously leads to $\lambda_m(\omega) = 0$, which has the meaningful interpretation that the most effective chassis excitation is achieved with resonant modes or modes next to resonances.
(5.3) clearly exhibits that modes with eigenvalues equal to or approximately zero potentialy dominate the overall radiation properties whereas modes with large eigenvalues only have a nonsignificant contribution. However, bringing a chassis mode to resonance at a given operating frequency might require a modification of the chassis geometry. Observations from investigations of radiation properties of Bar-Type mobile phones chassis with dimension ($100\,\mathrm{mm} \times 40\,\mathrm{mm}$) in the previous chapter, have revealed the appearance of the first resonant mode at $1334\,\mathrm{MHz}$. The use of the chassis to boost the antenna performances in this case is neither favorable for GSM 900 nor for GSM 1800. This situation can be overcame by implementing some tuning mechanism upon the chassis to switch its resonance frequency into the interested operating ranges. This can be achieved by changing its electrical length in such a way that it complies to our requirements. The next section deals with the maximization of the numerator.

5.2 Optimal Antenna Location on Mobile Phones Chassis

5.2.1 Capacitive Coupling

The reaction term $\langle \boldsymbol{J}_{\mathrm{s},m}, \boldsymbol{E}^{\mathrm{ex}}_{\tan}\rangle$ in the numerator of (5.3) describes the coupling between an exciting field $\boldsymbol{E}^{\mathrm{ex}}_{\tan}$ and the m^{th} characteristic mode. For a coupler (nominal antenna element) located somewhere in the vicinity of the chassis and generating an impressed field $\boldsymbol{E}^{\mathrm{ex}}_{\tan}$, this reaction can be also interpreted as a strength with which the mode $\boldsymbol{J}_{\mathrm{s},m}$ is excited on the chassis. The goal to achieve here is to maximize this term by optimum placement and design the nominal antenna element under the usual restriction of a limited antenna volume.
Aplication of the reciprocity theorem combined with the Cauchy-Schwarz inequality to the

reaction term yields,

$$|\langle \boldsymbol{J}_{\mathrm{s},m}, \boldsymbol{E}^{\mathrm{ex}}_{\tan}\rangle| = |\langle \boldsymbol{E}_m, \boldsymbol{J}^{\mathrm{ex}}\rangle| \leq \|\boldsymbol{E}_m\|\|\boldsymbol{J}^{\mathrm{ex}}\| \tag{5.4}$$

where $\boldsymbol{E}_m$ and $\boldsymbol{J}^{\mathrm{ex}}$ denote respectively, the modal characteristic field generated by $\boldsymbol{J}_{\mathrm{s},m}$ and the current density on the coupler and $\|f\| = \sqrt{\langle f, f\rangle}$. In (5.4) equality is achieved i.e. the excitation coefficient reaches its maximum attainable value if $\boldsymbol{E}_m$ and $\boldsymbol{J}_{\mathrm{s},m}$ are in the same direction.
The reaction $\langle \boldsymbol{J}_{\mathrm{s},m}, \boldsymbol{E}^{\mathrm{ex}}_{\tan}\rangle$ reaches its maximum if

- $\boldsymbol{J}_{\mathrm{s},m}$ and $\boldsymbol{E}^{\mathrm{ex}}_{\tan}$ are maximal and
- $\boldsymbol{J}_{\mathrm{s},m}$ and $\boldsymbol{E}^{\mathrm{ex}}_{\tan}$ are oriented in the same direction

This clearly means that for an effective excitation of the m^{th} mode by means of an impressed electric field over a small region on the chassis, the exciting surface current density muss be located about the maximum of the modal characteristic field $\boldsymbol{E}_m$ and furthermore aligned with it.
From the above analysis, it is then possible to investiage the optimal antenna location for an effective excitation of a given characteristic mode. For an optimal coupling between the nominal antenna element and the chassis at a given frequency, the optimal location of the coupler shall be investigated for the dominant chassis mode i.e mode with eigenvalues closed to zero.

5.2.2 Application to Bar-Type Phones

The investigation of the optimal placement of a capacitive coupler directly on top of the chassis, contributes considerably to the solution of the volume consumption problem for antenna developement in handheld devices. According to results contained in Table 4.1, the electric characteristic field strength for resonant modes have been represented. Fig. 5.1 shows the electric field strength generated by the first (A), second (B), third (C) and fourth (D) resonant characteristic mode as presented in Fig. 4.2 respectively, evaluated in a plane surface having the dimensions of the board extended by $10\,\mathrm{mm}$ at each side, parallel and $5\,\mathrm{mm}$ above the board. It clearly displays the potential optimal locations depicted in red for a capacitive coupler corresponding to the maxima of the resonant characteristic fields. Another aspect to be stretched is the fact that Fig. 5.1 does not represent the field polarization for a much accurate positioning of the exciter. It should be emphasized that at $5\,\mathrm{mm}$ height the field is predominantly vertical polarized with respect to the chassis.

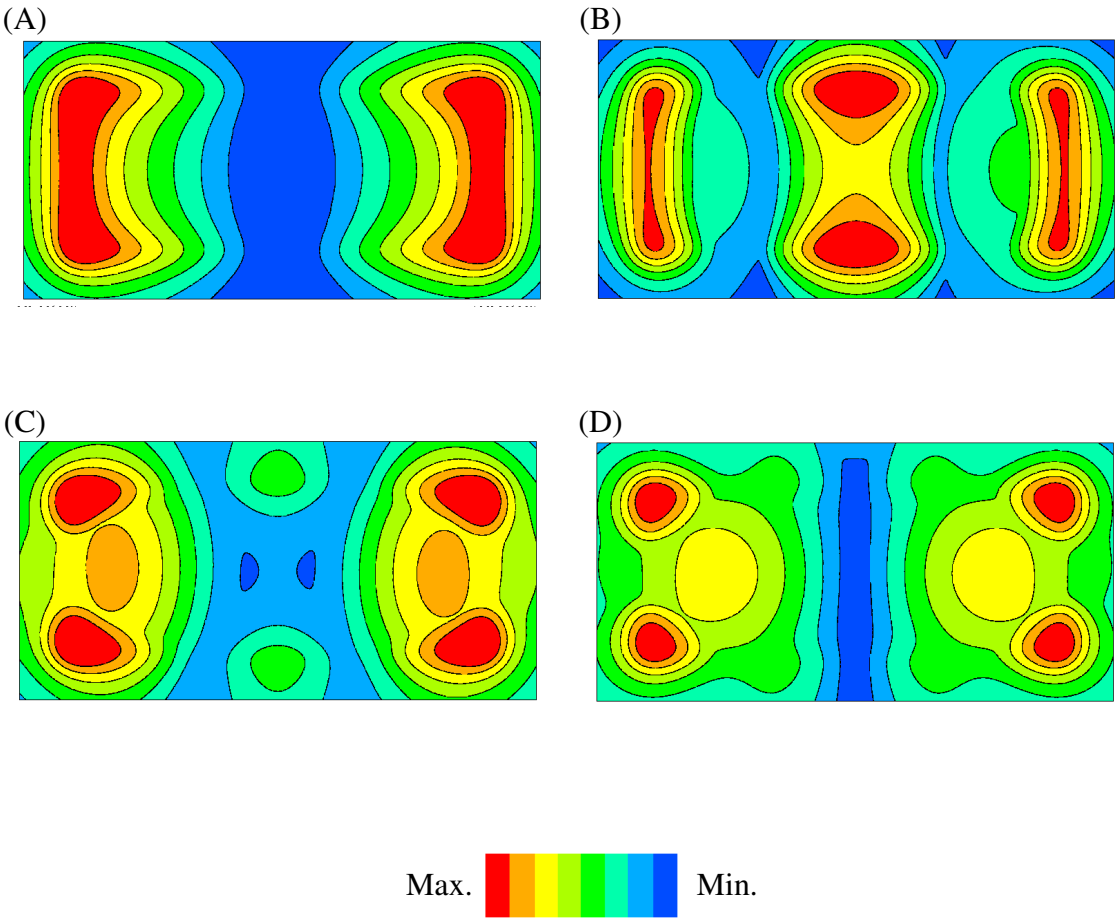

Figure 5.1: Electric field magnitude of first four characteristic mode resonances at frequencies (A) 1.33, (B) 3.01 , (C) 4.45 and (D) 4.78 GHz, evaluated on a plane 5 mm above the chassis.

5.2.3 Application to Folder-Type Phones

Folder-Type Opened State

Table 4.2 summarizes the radiation properties of a folder-type mobile phone in opened state modeled as plates with dimensions $70\,\mathrm{mm} \times 40\,\mathrm{mm}$ and $50\,\mathrm{mm} \times 40\,\mathrm{mm}$ for the base and flip part respectively. Fig. 5.2 represents the electric field strength of the first four resonant characteristic modes (Fig. 4.5) evaluated on a plane in a cross section along the major

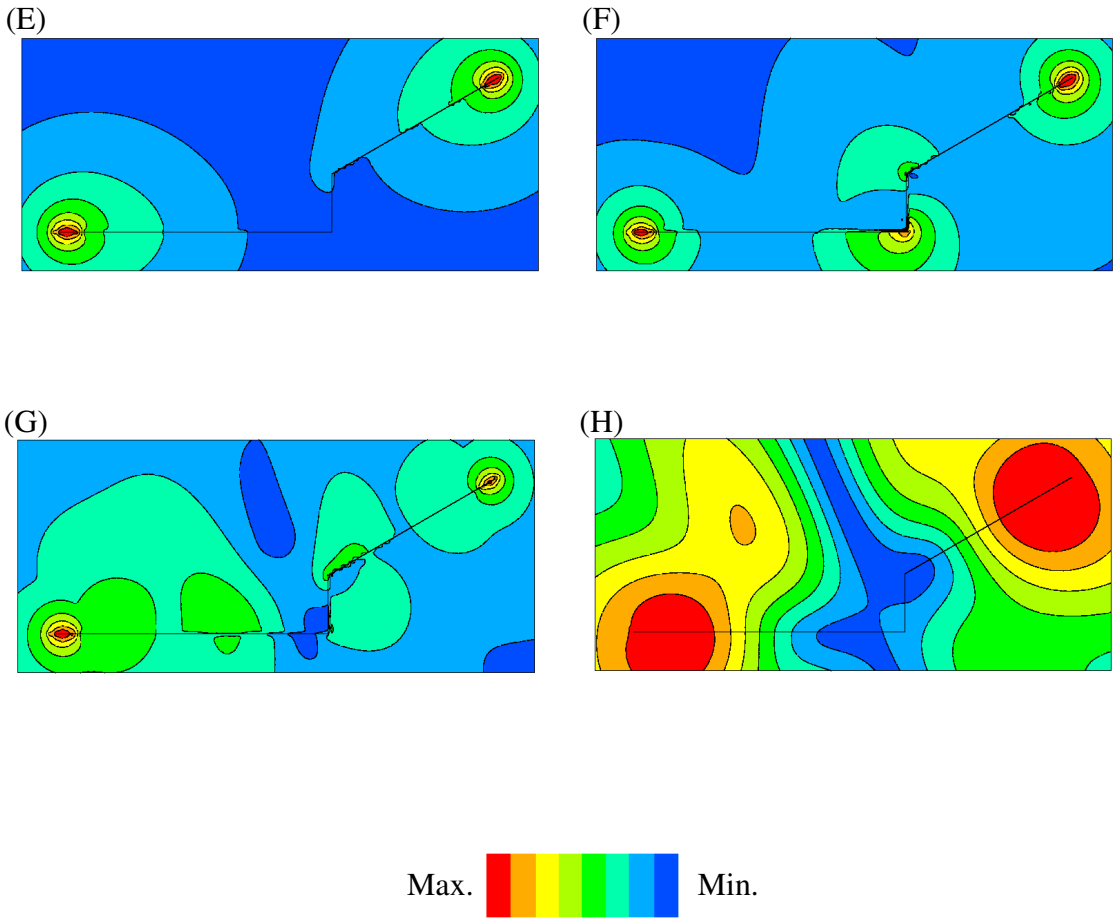

Figure 5.2: Electric field magnitude of the first four characteristic mode resonances at frequencies (E) 1.05, (F) 2.26, (G) 3.66 and (H) $4.38\,\mathrm{GHz}$, evaluated on a plane in a cross section along the major symmetry axis.

symmetry axis. It can be clearly observed for the lowest resonance that the characteristic field reaches its maximum (depicted in red) at the outer short edges of the flip and base part. To expose more details on the electric field behaviour, the modal electric field has been evaluated on segments located in the region of the chassis next to the outer short edges and paralel to them, confined in planes $5\,\mathrm{mm}$ above and parallel to the flip as well as to the base part, and shifted $2\,\mathrm{mm}$ from the short edges inside the open phone. Fig. 5.3

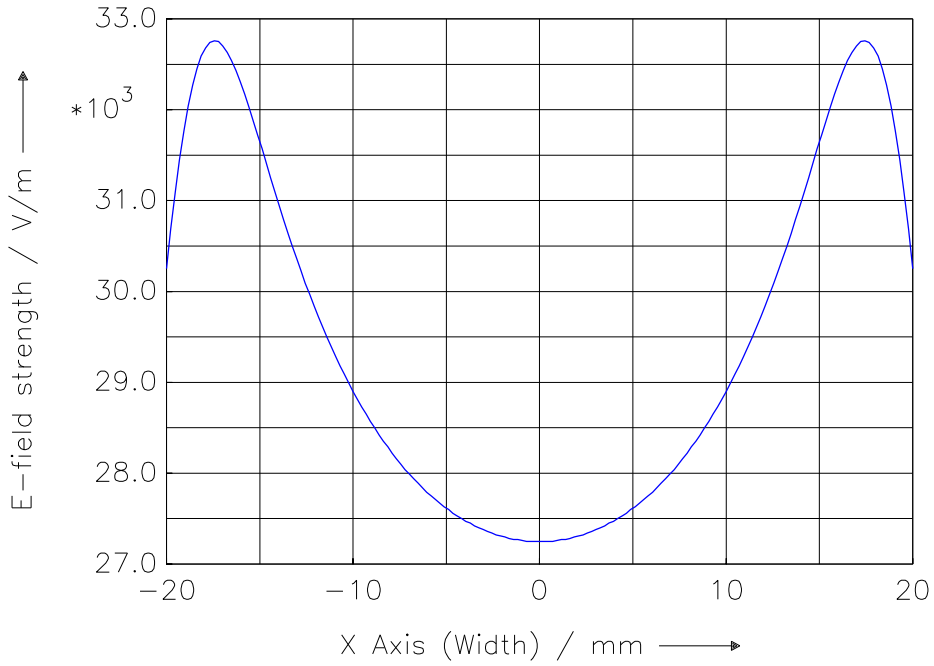

Figure 5.3: First resonant (1.05 GHz) characteristic field magnitude evaluated on segments next to the outer short edges of a folder type open phone.

shows that the optimal placement of the coupler above the chassis is situated in the corners. Analogous representations can be performed for the same positions at different frequencies to accurately determined the optimal placement of the antenna.

Folder-Type Closed State

The radiation properties of a folder type mobile phone in closed state are summarized for the first four resonances in Table 4.3, where the dimensions as specified in the previous case have not been changed. Fig. 5.8 shows the electric field strength distribution for the first four characteristic mode resonances, evaluated on a plane in a cross section along the major symmetry axis. Regions of interest are depicted in red and specify the optimal location for a capacitive coupler. It should be pointed out that in most of the cases, the optimal location is in the vicinity of the short edges.

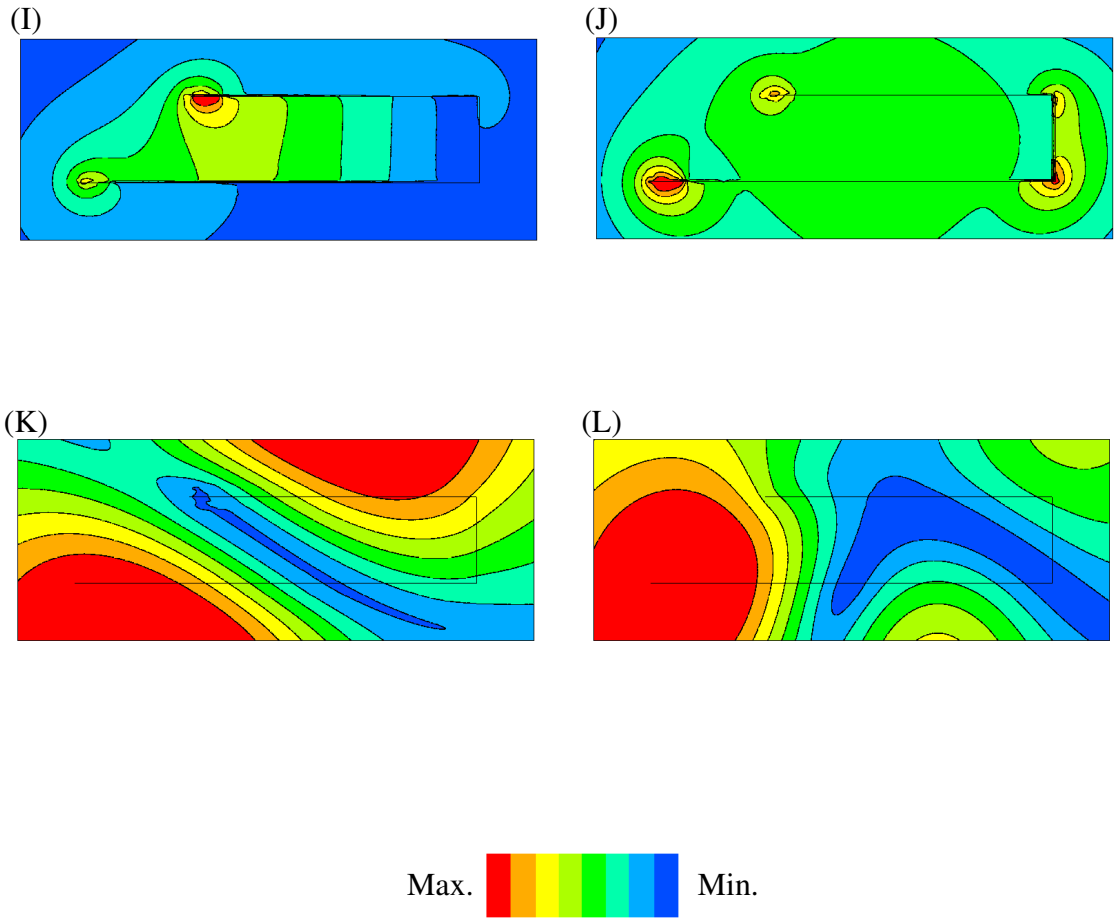

Figure 5.4: Electric field magnitude of the first four characteristic mode resonances at frequencies (I) 1.13, (J) 2.51, (K) 3.27 and (L) 4.57 GHz, evaluated on a plane in a cross section along the major symmetry axis.

5.2.4 Magnetic Coupling

As previously done for a capacitive coupling, relations and conditions for an optimal magnetic coupling between the nominal antenna element and the chassis can be established by making use of the symmetry or duality relations between electric and magnetic quantities.

Denoting by $\boldsymbol{H}^{\mathrm{ex}}$ and $\boldsymbol{M}_{\mathrm{s}}$ respectively, an external exciting magnetic field and the corresponding induced magnetic current on a conducting body, the dual relation to equation 5.5 gives,

$$\boldsymbol{M}_{\mathrm{s}} = \sum_{m} \frac{\langle \boldsymbol{M}_{\mathrm{s},m}, \boldsymbol{H}^{\mathrm{ex}}_{\mathrm{tan}} \rangle}{(1 + \mathrm{j}\lambda_m) 2 P_m} \boldsymbol{M}_{\mathrm{s},m} \tag{5.5}$$

where $\boldsymbol{M}_{\mathrm{s},m}$ is the m^{th} magnetic characteristic mode, $P_m = \frac{1}{2}\langle \boldsymbol{M}_{\mathrm{s},m}, \widehat{\mathbf{R}} \boldsymbol{M}_{\mathrm{s},m} \rangle$ and $\boldsymbol{H}^{\mathrm{ex}}_{\mathrm{tan}}$ the tangential component of the exciting field.
The reaction term $\langle \boldsymbol{M}_{\mathrm{s},m}, \boldsymbol{H}^{\mathrm{ex}}_{\mathrm{tan}} \rangle$ describes the coupling between the exciting magnetic field and the m^{th} magnetic characteristic mode. It can be also interpreted as the strength deployed by the coupler to excite the m^{th} characteristic mode. For a magnetic coupler located in the vicinity of the chassis and generating the magnetic field $\boldsymbol{H}^{\mathrm{ex}}_{\mathrm{tan}}$, an optimal coupling is reached if the reaction is maximum. As already demonstrated for an electrical coupler in section 5.2.1, this is achieved if:

- $\boldsymbol{M}_{\mathrm{s},m}$ and $\boldsymbol{H}^{\mathrm{ex}}_{\mathrm{tan}}$ are maximal and
- $\boldsymbol{M}_{\mathrm{s},m}$ and $\boldsymbol{H}^{\mathrm{ex}}_{\mathrm{tan}}$ are oriented in the same direction

In other words, for an effective excitation of the m^{th} mode by means of an impressed magnetic field over a small region on the chassis, the exciting magnetic surface current density muss be located about the maximum of the modal characteristic field $\boldsymbol{H}_m$ and furthermore aligned with it.

5.2.5 Application to Bar-Type Phones

Investigation of the optimal placement of a magnetic coupler directly on top of the chassis explores the possibilities of effectively exciting the dominant characteristic modes at a given frequency. It also contributes to the solution of the volume consumption problem for antenna development in handheld devices, since it accurately indicates the location of the antenna element on the chassis. Fig. 5.5 shows the magnetic field strength generated by the first (A), the second (B), the third (C) and the fourth (D) resonant mode as specified in the entries of Table 4.1, evaluated in a plane surface having the dimensions of the board extented by $10\,\mathrm{mm}$ at each side, parallel and $5\,\mathrm{mm}$ above the board. The potential optimal locations are depicted in red for magnetic exciters. It should be stretched that at $5\,\mathrm{mm}$ the magnetic field is predominantly horizontal polarized.

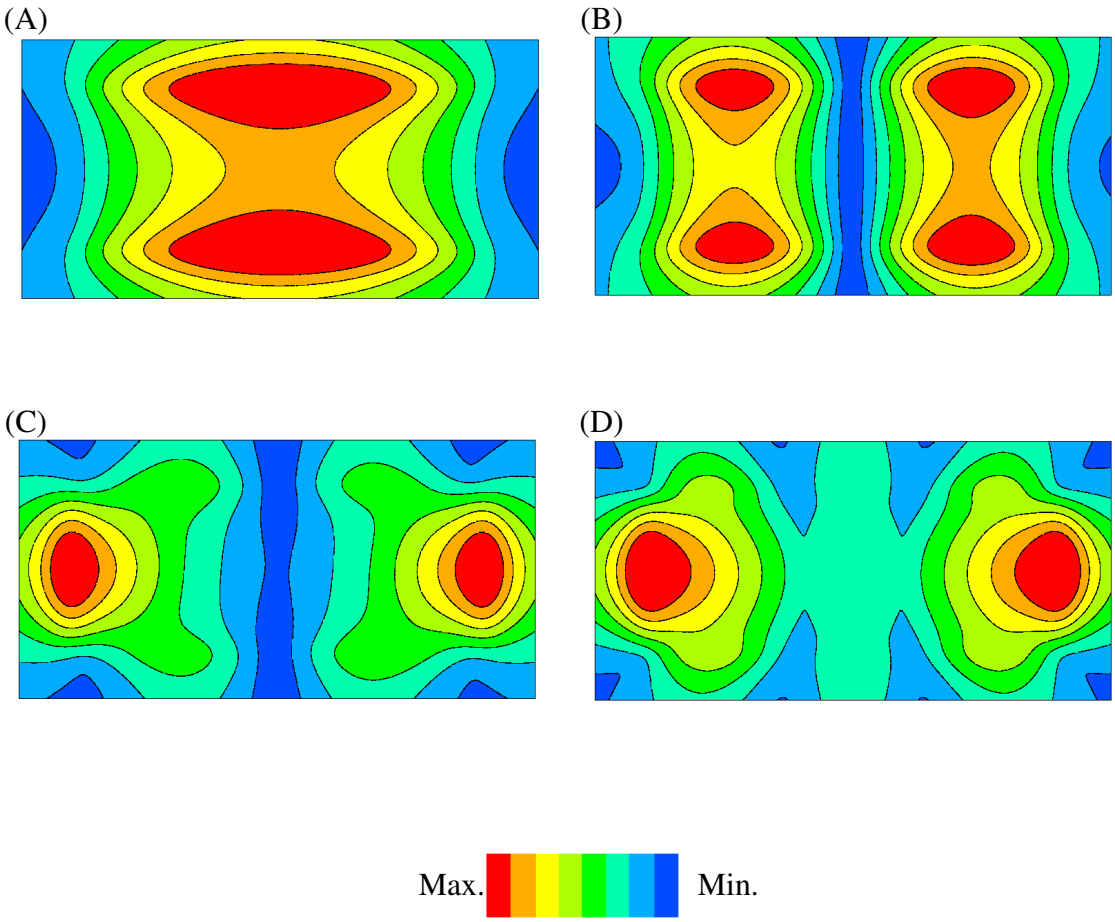

Figure 5.5: Magnetic field strength of the first four characteristic mode resonances at frequencies (A) 1.33, (B) 3.01 , (C) 4.45 and (D) 4.78 GHz, evaluated on a plane 5 mm above the chassis.

5.2.6 Folder-Type Phone Structure

Folder-Type Opened State

Complying with the entries in Table 4.2, investigation for the optimal location of the magnetic exciter have been performed. Fig. 5.6 shows the magnetic field strength of the first four characteristic mode resonances at frequencies (E) 1.05, (F) 2.26, (G) 3.66 and (H) 4.38 GHz, evaluated on a plane situated in the cross section along the major symmetry

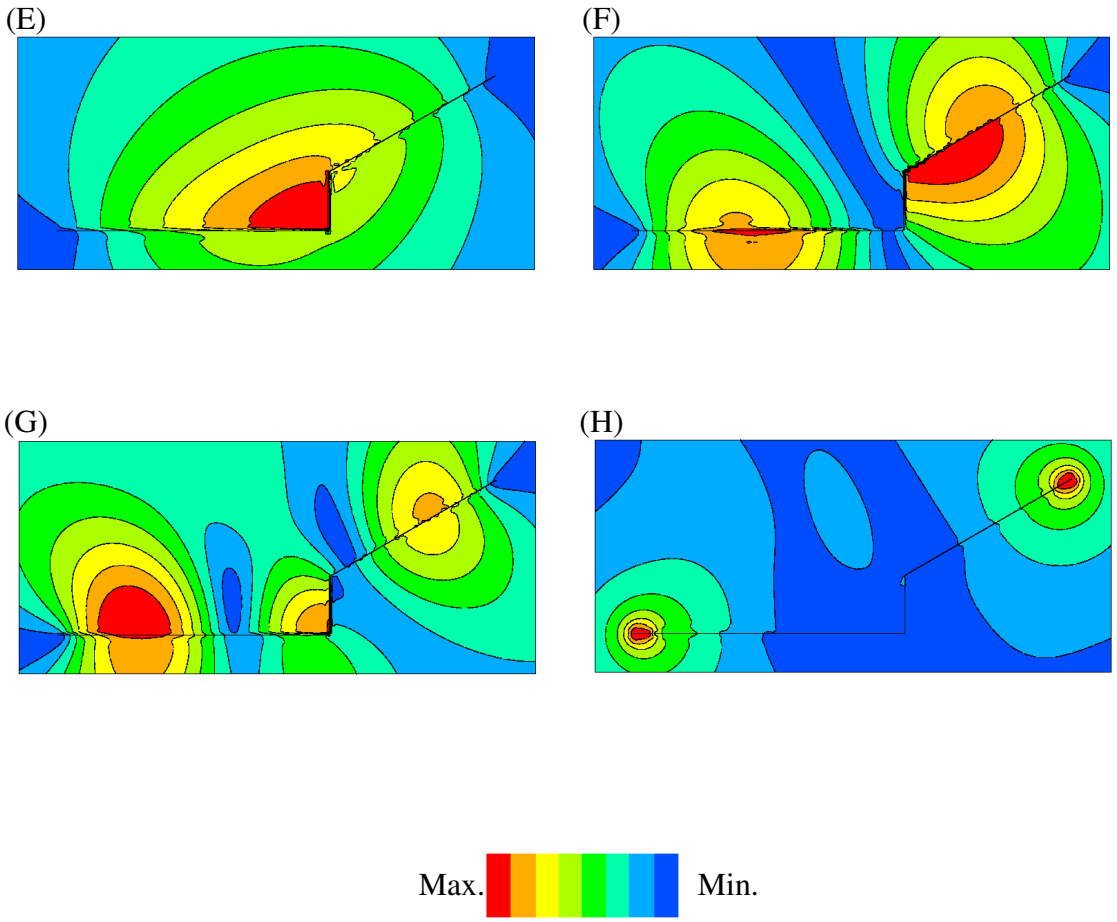

Figure 5.6: Magnetic field strength of the first four characteristic mode resonances at frequencies (E) 1.05, (F) 2.26, (G) 3.66 and (H) 4.38 GHz, evaluated on a plane in a cross section along the major symmetry axis.

axis. It can be easily observed for the lowest resonant mode that the characteristic field reaches its maximum (depicted in red) at the junction between the base and the connection plate. For more details, the magnetic field distribution in that region, has been evaluated on a segment 10 mm parallel and distant from the junction with the base and included inside the bissector plane of the base and the connection plate. This clearly shows that the optimal location for a magnetic coupler at 1.05 GHz is at the edges of the junction between the base

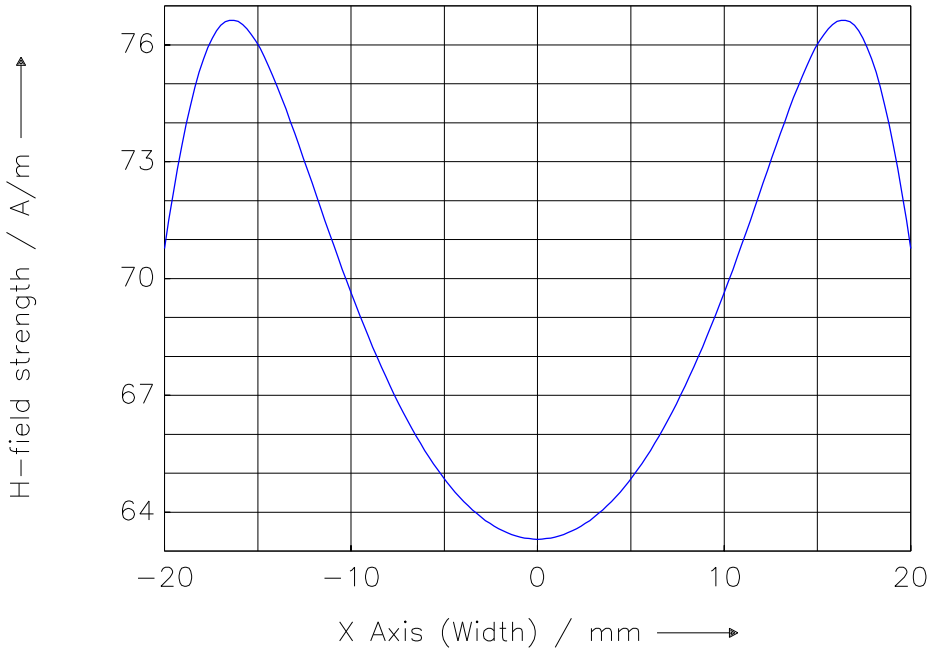

Figure 5.7: First magnetic resonant (1.05 GHz) characteristic field magnitude evaluated on a segment next to the junction between the base and the connection plane.

and the connection plate.

Folder-Type Closed State

At resonance frequencies specified in Table 4.3, the optimal location of magnetic exciters are investigated for folder type mobile phones in closed state. Fig. 5.8 represents the magnetic field strength of the first resonant characteristic modes evaluated on a plane in a cross section along the major symmetry axis. As already mentioned in the last sections, not only the field strength of the characteristic field should be taken in consideration, but also the polarization of the exciter. Potential optimal locations are depicted in red and the field should be prodominantly vertical polarized.

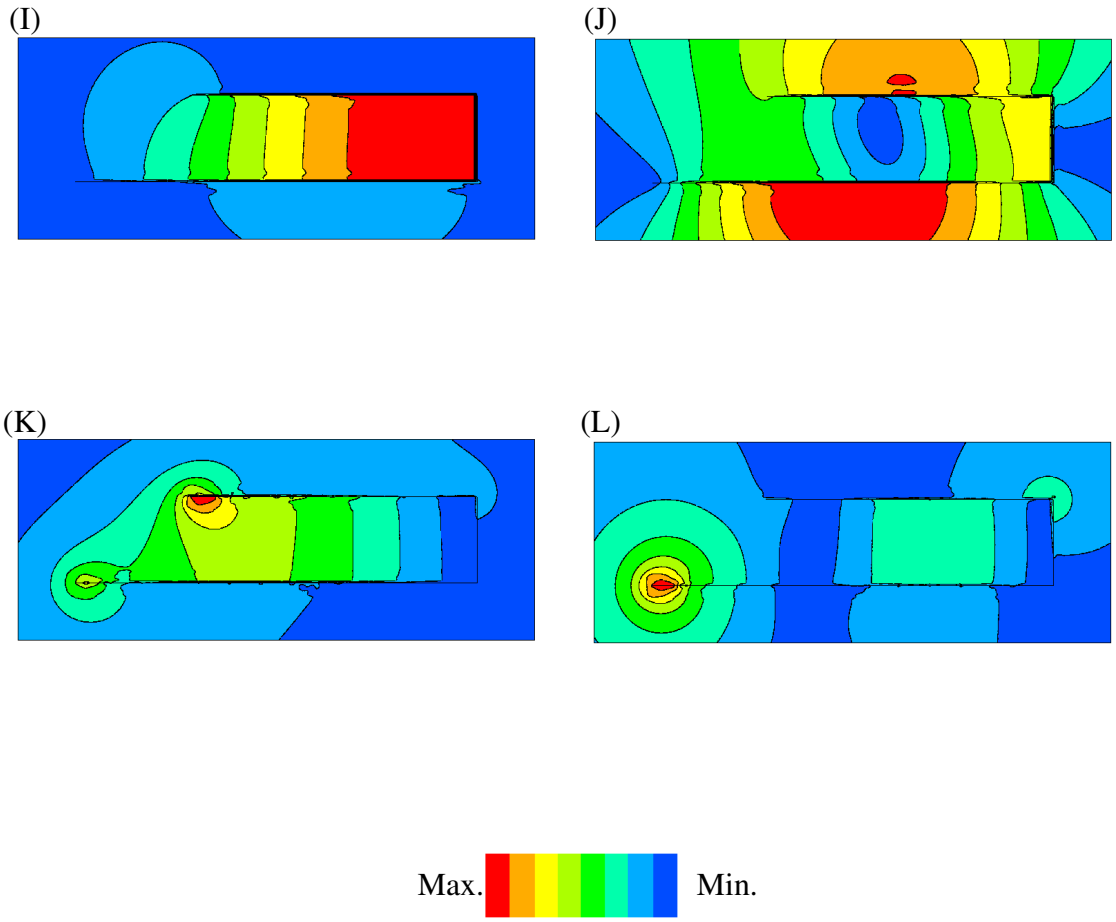

Figure 5.8: Magnetic field magnitude of the first four characteristic mode resonances at frequencies (I) 1.13, (J) 2.51, (K) 3.27 and (L) 4.57 GHz, evaluated on a plane in a cross section along the major symmetry axis.

5.2.7 Experimental Results of Field Evaluation

For verification purposes, measurements have been performed in the case of a $100\,\mathrm{mm} \times 40\,\mathrm{mm}$ rectangular metallic chassis for a bar-type phone. In this experiment a network analyser which port 1 is connected to a probe placed not far from one of the short edges of the chassis for its excitation. A second probe connected to port 2 placed at around $5\,\mathrm{mm}$ above the

chassis is moved exactly on the major axis at points equidistant of $5\,\mathrm{mm}$ starting from the middle of one of the short edges. Fig. 5.9 show the side and top views of the measurement installation. The field strength evaluated at different positions on the chassis in terms of

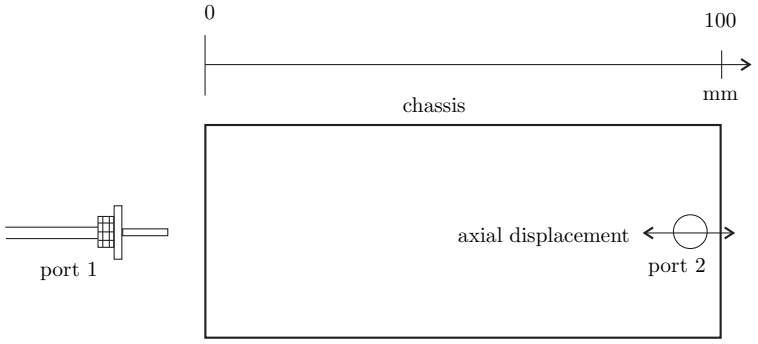

Measurement Installation (Top View)

(A)

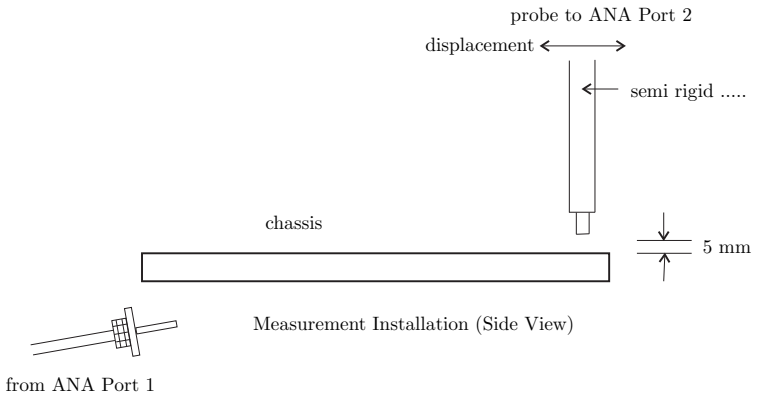

Measurement Installation (Side View)

(B)

Figure 5.9: Top (A) and side (B) views of the measurement installation.

logarithm of the magnitude of the scattering parameter S_{21} at the first resonance frequency $1.33\,\mathrm{GHz}$ is shown in Fig. (5.10) A.
The magnitude of the field strengh shows an asymmetry at different short edges. The edge with high field magnitudes reflects the presence of the excitation probe which clearly increases the field strength. Due to the asymmetry of the chassis, the expected decrease to minus infinity of the field strength is not observed in the middle of the major axis. In the middle of the short edges the field strength has been measured in the frequency range between $0.5\,\mathrm{GHz}$ and $3\,\mathrm{GHz}$. Fig. (5.10) B shows the field strength obtained at different

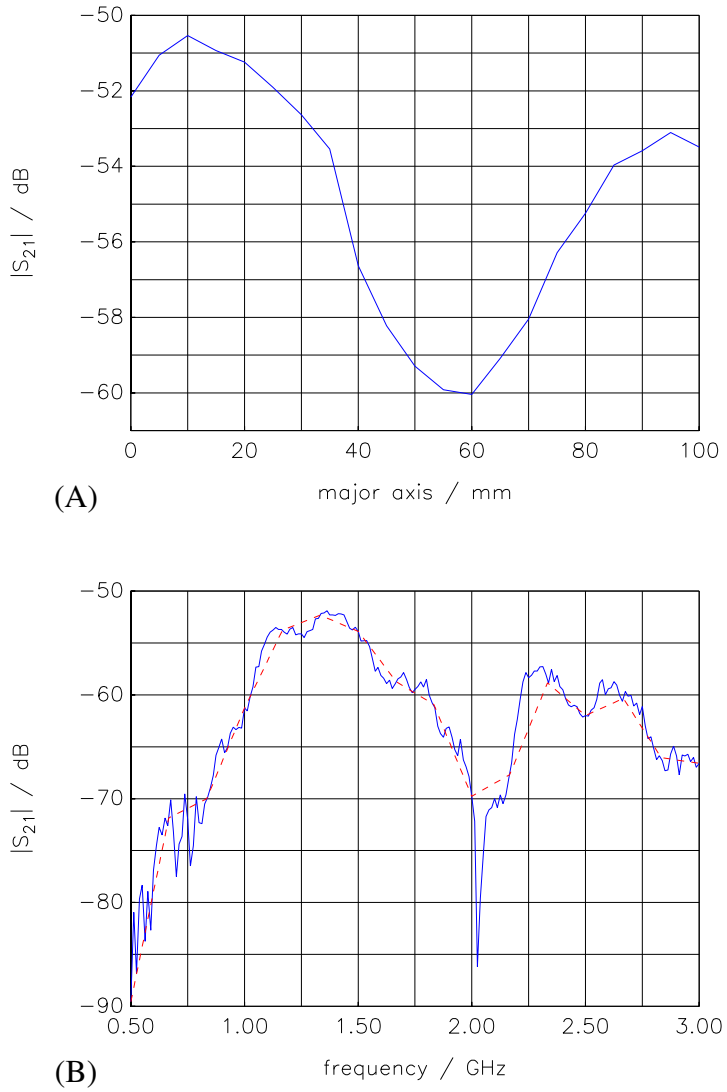

Figure 5.10: (A) Field strength measured in the major axis at $5\,\mathrm{mm}$ above the chassis. (B) Field strength measured in the frequency range between $0.5\,\mathrm{GHz}$ and $3\,\mathrm{GHz}$ at the middle of one of the short edges.

frequencies. Depicted in blue is the field strength at different frequencies and in red an approximation of the blue curve obtained by making use of the spline fitting method. This measurements present a maximum field strength at frequency $1.33\,\mathrm{GHz}$ which corresponds

to the frequency of the first resonant characteristic mode as observed with simulation results contained in table 4.1. Due to the irregularity of the curve representing the measurements as shown in blue in Fig. (5.10) B, evaluation of the $3\,\mathrm{dB}$-relative bandwidth is performed with respect to the fitted curve (in red) around the resonance frequency. It gives a radiation quality factor of 2.53 which is not so far from the simulated result 2.9 .

5.3 Approximate Evaluation of the Coupling Factor

5.3.1 Capacitive Coupling

In the proposed evaluation, the approximation of the reaction term in the numerator of (5.5) assumes the electrical characteristic field to be stationary in the region where it reaches its maximum. $\boldsymbol{E}_m$ is thus considered as the gradient of an electric scalar potential denoted by φ_m and expressed as $\boldsymbol{E}_m \approx -\nabla\varphi_m$, with $\varphi_m = 0$ on the surface of the chassis. By making use of the reciprocity theorem the reaction term can also be rewritten in the form

$$\langle \boldsymbol{J}_{\mathrm{s},m}, \boldsymbol{E}^{\mathrm{ex}}_{\tan} \rangle = \oiint_S \boldsymbol{J}_{\mathrm{s},m} \boldsymbol{E}^{\mathrm{ex}}_{\tan}\,\mathrm{d}S = \iiint_V \boldsymbol{E}_m \boldsymbol{J}^{\mathrm{ex}}\,\mathrm{d}V \tag{5.6}$$

where as already mentioned $\boldsymbol{E}_m$ represents the characteristic field generated by $\boldsymbol{J}_{\mathrm{s},m}$ a modal current density. Substitution of this expresssion in (5.6) yields

$$\iiint_V \boldsymbol{E}_m \boldsymbol{J}^{\mathrm{ex}}\,\mathrm{d}V \approx -\iiint_V \boldsymbol{J}^{\mathrm{ex}} \nabla\varphi_m\,\mathrm{d}V. \tag{5.7}$$

Applying the following identity

$$\nabla \cdot \psi\boldsymbol{A} = \boldsymbol{A} \cdot \nabla\psi + \psi\nabla \cdot \boldsymbol{A} \tag{5.8}$$

combined with the divergence theorem on the right hand side of (5.7), one obtains

$$\begin{aligned} -\iiint_V \boldsymbol{J}^{\mathrm{ex}} \nabla\varphi_m\,\mathrm{d}V &= -\iiint_V \nabla \cdot (\varphi_m \boldsymbol{J}^{\mathrm{ex}})\,\mathrm{d}V + \iiint_V \varphi_m \nabla \cdot \boldsymbol{J}^{\mathrm{ex}}\,\mathrm{d}V \\ &= \oint_S \varphi_n \boldsymbol{J}^{\mathrm{ex}} \cdot \boldsymbol{n}\,\mathrm{d}S + \iiint_V \varphi_n \nabla \cdot \boldsymbol{J}^{\mathrm{ex}}\,\mathrm{d}V \\ &= \iiint_V \varphi_n \nabla \cdot \boldsymbol{J}^{\mathrm{ex}}\,\mathrm{d}V \end{aligned} \tag{5.9}$$

where $\boldsymbol{n}$ in the second line of (5.9) represents the outward normal to the surface S insiding the volume V and is obviously orthogonal to the surface current density $\boldsymbol{J}^{\mathrm{ex}}$ on the exciter.

According to the charge conservation law, $\boldsymbol{J}^{\mathrm{ex}}$ can be expressed as follows

$$\nabla \cdot \boldsymbol{J}^{\mathrm{ex}} = -\mathrm{j}\omega\rho^{\mathrm{ex}} \tag{5.10}$$

where ρ^{ex} denotes the electric charge density on the exciter. Replacing (5.10) in (5.9) leads to

$$\begin{aligned} -\iiint_V \boldsymbol{J}^{\mathrm{ex}} \nabla\varphi_m \,\mathrm{d}V &= \iiint_V \varphi_m \nabla\cdot\boldsymbol{J}^{\mathrm{ex}} \,\mathrm{d}V \\ &\approx -\mathrm{j}\omega\overline{\varphi_m} \iiint_V \rho^{\mathrm{ex}} \,\mathrm{d}V \\ &= -\mathrm{j}\omega\overline{\varphi_m} Q^{\mathrm{ex}} = -\overline{\varphi_m} i^{\mathrm{ex}} \end{aligned} \tag{5.11}$$

where $\overline{\varphi_m}$ denotes an average of φ_m over the coupler with respect to the charge density ρ^{ex}, Q^{ex} the total charge and i^{ex} the associated current into the coupler.
Considering a capacitive coupling patch whose shape conforms to one of the (local) equi-potential surfaces, $\overline{\varphi_m}$ is then just the potential associated with the equi-potential surface and remains constant when the patch is moved within the equi-potential surface. An example of equi-potential sufaces is shown in Fig. (5.11b) at the short edge of a Bar-Type phone for the first resonant characteristic mode. It then obvious that under the constraint of constant radiated power
The chassis total radiated power is obtained by making use of the modal pattern orthogonality as

$$\begin{aligned} P_{\mathrm{rad}} &= \langle \boldsymbol{J}_{\mathrm{s}}{}^{*}, \widehat{\mathbf{R}}\boldsymbol{J}_{\mathrm{s}} \rangle = 2\sum_m |\alpha_m|^2 P_m \\ &= \sum_m \frac{|\langle \boldsymbol{J}_{\mathrm{s},m}, \boldsymbol{E}^{\mathrm{ex}}_{\tan}\rangle|^2}{2\,|1+\mathrm{j}\lambda_m|^2 P_m} \end{aligned} \tag{5.12}$$

where $P_m = \frac{1}{2}\langle \boldsymbol{J}_{\mathrm{s},m}, \widehat{\mathbf{R}}\boldsymbol{J}_{\mathrm{s},m}\rangle$ represents the radiated power generated by the m^{th} mode. It is immediately obvious from (5.12) that only modes near resonance can make a significant contribution to the total radiated power. Rewriting the terms on the right hand side of (5.12) using the approximation (5.11) tells that the total radiated power is approximately given by

$$\begin{aligned} P_{\mathrm{rad}} &\approx \sum_m \frac{1}{|1+\mathrm{j}\lambda_m|^2} \cdot \frac{1}{2}\frac{|\overline{\varphi_m}|^2}{P_m} |i^{\mathrm{ex}}|^2 \\ &= \sum_m \frac{1}{|1+\mathrm{j}\lambda_m|^2} \cdot \frac{1}{2} R_{\mathrm{rad},m} |i^{\mathrm{ex}}|^2 \end{aligned} \tag{5.13}$$

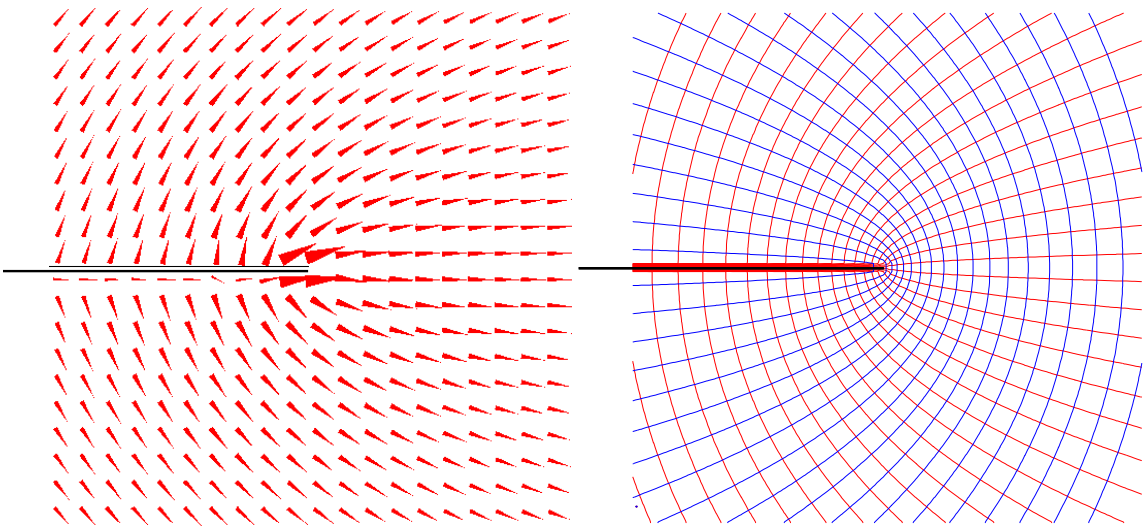

(a) (b)

Figure 5.11: Electric field near short edge of a $100 \times 40\,\mathrm{mm}$ plate at lowest resonant characteristic mode (a) compared to gradient field approximation by conformal mapping $\zeta = z^2$ (b).

Considering the example of Bar-Type mobile phone as recapitulated in Table 4.1, at the first resonance ($1334\,\mathrm{MHz}$) (5.13) becomes

$$P_{\mathrm{rad}} \approx \frac{1}{2} R_{\mathrm{rad},0} \left| i^{\mathrm{ex}} \right|^2 \tag{5.14}$$

this means the radiation resistance of the coupler and thereby bandwidths are maximized. It then obvious that under the constraint of constant radiated power and fixed current into the coupling patch, placement in front of the short edge leads to minimum distance from the PCB and thereby smallest volume consumption.
At the third and fourth resonances, the second and third order modes are also almost resonant and (5.13) becomes in those cases

$$P_{\mathrm{rad}} \approx \frac{1}{2} \left(R_{\mathrm{rad},0} + R_{\mathrm{rad},1} + R_{\mathrm{rad},2} \right) \left| i^{\mathrm{ex}} \right|^2 \tag{5.15}$$

since λ_1 and λ_2 are almost 0.

5.3.2 Magnetic Coupling

Due to the duality relations between electric and magnetic fields, from equations established in the previous section, approximation relations for a magnetic coupler can be easily developed. $\boldsymbol{H}_m$ is the gradient of a magnetic scalar potential denoted $\varphi_{\mathrm{m},m}$ and expressed as $\boldsymbol{H}_m = -\nabla\varphi_{\mathrm{m},m}$. One obtains as evaluation of the reaction term in the nominator of (5.5)

$$\langle \boldsymbol{M}_{\mathrm{s},m}, \boldsymbol{H}^{\mathrm{ex}}_{\tan}\rangle = \iiint_V \boldsymbol{H}_m \boldsymbol{M}^{\mathrm{ex}}\,\mathrm{d}V = -\iiint_V \boldsymbol{M}^{\mathrm{ex}}\nabla\varphi_{\mathrm{m},m}\,\mathrm{d}V \tag{5.16}$$

where $\boldsymbol{M}^{\mathrm{ex}}$ is the current density on the exciter and $\boldsymbol{H}_m$ the magnetic modal characteristic field generated by $\boldsymbol{M}_{\mathrm{s},m}$.
Analogous to (5.9), one obtains

$$-\iiint_V \boldsymbol{M}^{\mathrm{ex}}\nabla\varphi_{\mathrm{m},m}\,\mathrm{d}V = \iiint_V \varphi_{\mathrm{m},m}\nabla\cdot\boldsymbol{M}^{\mathrm{ex}}\,\mathrm{d}V \tag{5.17}$$

By applying the charge conservation's law, where $\rho^{\mathrm{m}}_{\mathrm{ex}}$ denotes the magnetic charge density on the exciter, $\overline{\varphi_{\mathrm{m},m}}$ an average of the magnetic scalar potential $\varphi_{\mathrm{m},m}$, $\Phi^{\mathrm{m}}_{\mathrm{ex}}$ the magnetic flux and $u^{\mathrm{m}}_{\mathrm{ex}}$ the electrical potential, (5.17) yields

$$\begin{aligned}
-\iiint_V \boldsymbol{M}^{\mathrm{ex}}\nabla\varphi_{\mathrm{m},m}\,\mathrm{d}V &= \iiint_V \varphi_{\mathrm{m},m}\nabla\cdot\boldsymbol{M}^{\mathrm{ex}}\,\mathrm{d}V \\
&\approx -\mathrm{j}\omega\overline{\varphi_{\mathrm{m},m}}\iiint_V \rho^{\mathrm{m}}_{\mathrm{ex}}\,\mathrm{d}V \\
&= -\mathrm{j}\omega\overline{\varphi_{\mathrm{m},m}}\Phi^{\mathrm{m}}_{\mathrm{ex}} \\
&= -\mathrm{j}\overline{\varphi_{\mathrm{m},m}}u^{\mathrm{m}}_{\mathrm{ex}}
\end{aligned} \tag{5.18}$$

The chassis total radiated power can be derived by making use of the pattern orthogonality

$$\begin{aligned}
P_{\mathrm{rad}} &= \langle \boldsymbol{M}_{\mathrm{s}}{}^{*}, \widehat{\mathbf{R}}\boldsymbol{M}_{\mathrm{s}}\rangle = 2\sum_m |\alpha_m|^2 P_m \\
&= \sum_m \frac{|\langle \boldsymbol{M}_{\mathrm{s},m}, \boldsymbol{H}^{\mathrm{ex}}_{\tan}\rangle|^2}{2\,|1+\mathrm{j}\lambda_m|^2 P_m}
\end{aligned} \tag{5.19}$$

Substituting the approximation relation (5.18) in (5.19) leads to

$$\begin{aligned}
P_{\mathrm{rad}} &\approx \sum_n \frac{1}{|1+\mathrm{j}\lambda_m|^2}\cdot\frac{1}{2}\frac{|\overline{\varphi_{\mathrm{m},m}}|^2}{P_m}\,|u^{\mathrm{m}}_{\mathrm{ex}}|^2 \\
&= \sum_m \frac{1}{|1+\mathrm{j}\lambda_m|^2}\cdot\frac{1}{2}G_m\,|u^{\mathrm{m}}_{\mathrm{ex}}|^2
\end{aligned} \tag{5.20}$$

where G_m represents the *radiation conductance* of the coupler for the m^{th} mode.

Chapter 6

A Simplified Method for Chassis Radiation Properties Analysis

This chapter contains results obtained in the frame of a master thesis with topic "Investigation of resonant modes on the chassis of handheld wireless terminal".
Essential results obtained in this chapter have been published in [11]. Here we provide details and develop further some aspects of that publication.

As observed in previous chapters, the concept of characteristic modes and resonant mode analysis is a powerful analytical tool. It is currently not supported by commercial CEM software packages and therefore impractical in everyday design work.

6.1 Simplified Analysis

A lot of useful information about resonance modes can nevertheless be collected by means of the simple hands-on approach outlined below. Focus is on the far-field radiation properties of a small radiator in free space.

6.1.1 Radiated fields in the far-field approximation

The radiated fields due to the current density $\boldsymbol{J}_{\mathrm{s}}(\boldsymbol{r}')$ on the chassis of a mobile device in the far-field approximation in free-space [33] chap. 13, page 471 are given by:

$$\boldsymbol{E}(\boldsymbol{r}) = \mathrm{j}\omega\mu_0 \frac{e^{-\mathrm{j}kr}}{4\pi r}(\boldsymbol{k} \times (\boldsymbol{k} \times \boldsymbol{F}(\boldsymbol{k}))) \tag{6.1}$$

$$\boldsymbol{H}(\boldsymbol{r}) = -jk \frac{e^{-\mathrm{j}kr}}{4\pi r}(\boldsymbol{k} \times \boldsymbol{F}(\boldsymbol{k})) \tag{6.2}$$

where r denotes the distance to the observation point $\boldsymbol{r}$, $\boldsymbol{r}'$ the source point and the radiation vector

$$\boldsymbol{F}(\boldsymbol{k}) = \int_{\boldsymbol{r}' \in S} \boldsymbol{J}_{\mathrm{s}}(\boldsymbol{r}') e^{j\boldsymbol{k}\cdot\boldsymbol{r}'} \,\mathrm{d}S \tag{6.3}$$

where $\boldsymbol{k} = k\boldsymbol{r}/r$ represents the wave vector with orientation towards the observation point. The radiated power density into the $\boldsymbol{k}$ direction is given by

$$S(\boldsymbol{k}) = \frac{Z_0}{32\pi^2 r^2} \left|\boldsymbol{k} \times \boldsymbol{F}(\boldsymbol{k})\right|^2 \tag{6.4}$$

and is proportional to the square of the normal to the $\boldsymbol{k}$ componant of the radiation vector. If the device is electrically small (diameter $< \lambda_0/\pi$), the radiation vector can typically with acceptable error be approximate by its first two moments.
The approach proposed here to arrive at expressions of the first and second moments is a multipole expansion of the exponential term in (6.3) about the origin. One obtains

$$e^{\mathrm{j}\boldsymbol{k}\cdot\boldsymbol{r}'} \approx 1 + \mathrm{j}\boldsymbol{k}\cdot\boldsymbol{r}' - \frac{1}{2}(\boldsymbol{k}\cdot\boldsymbol{r}')^2 + \cdots + \tag{6.5}$$

In the first approximation, solely the first term in the expansion series is considered. The radiation vector $\boldsymbol{F}(\boldsymbol{k})$ is then approximated by the *first order moment* expressed as follows:

$$\boldsymbol{F}_0(\boldsymbol{k}) = \int_{\boldsymbol{r}' \in S} \boldsymbol{J}_{\mathrm{s}}(\boldsymbol{r}') \,\mathrm{d}S = -\mathrm{j}\omega\boldsymbol{p} \tag{6.6}$$

where $\boldsymbol{p}$ denotes the *electric dipole moment* of the current distribution as indicated in [34]. The *second order moment* takes in consideration only the second term in the expansion series and is expressed as :

$$\boldsymbol{F}_1(\boldsymbol{k}) = \mathrm{j} \int_{\boldsymbol{r}' \in S} \boldsymbol{J}_{\mathrm{s}}(\boldsymbol{r}')(\boldsymbol{k}\cdot\boldsymbol{r}') \,\mathrm{d}S \tag{6.7}$$

This can also be rewritten by making use of the vector identity

$$\boldsymbol{V}(\boldsymbol{U}\cdot\boldsymbol{W}) = \boldsymbol{U}\times(\boldsymbol{V}\times\boldsymbol{W}) + \boldsymbol{W}(\boldsymbol{U}\cdot\boldsymbol{V})$$

as follows

$$\begin{aligned} 2\boldsymbol{F}_1(\boldsymbol{k}) &= \mathrm{j}\int_{\boldsymbol{r}'\in S} (\boldsymbol{r}' \times \boldsymbol{J}_{\mathrm{s}}(\boldsymbol{r}')) \times \boldsymbol{k} \,\mathrm{d}S + \mathrm{j}\int_{\boldsymbol{r}'\in S} \boldsymbol{r}'(\boldsymbol{J}_{\mathrm{s}}(\boldsymbol{r}')\cdot\boldsymbol{k} \,\mathrm{d}S + \mathrm{j}\int_{\boldsymbol{r}'\in S} \boldsymbol{J}_{\mathrm{s}}(\boldsymbol{r}')(\boldsymbol{r}'\cdot\boldsymbol{k}) \,\mathrm{d}S \\ &= \int_{\boldsymbol{r}'\in S} (\boldsymbol{r}' \times \boldsymbol{J}_{\mathrm{s}}(\boldsymbol{r}')) \,\mathrm{d}S \times \mathrm{j}\boldsymbol{k} + \int_{\boldsymbol{r}'\in S} (\boldsymbol{r}'\boldsymbol{J}_{\mathrm{s}}^{\top}(\boldsymbol{r}') + \boldsymbol{J}_{\mathrm{s}}(\boldsymbol{r}')\boldsymbol{r}'^{\top}) \,\mathrm{d}S \cdot \mathrm{j}\boldsymbol{k} \\ &= 2\boldsymbol{m} \times \mathrm{j}\boldsymbol{k} - \omega\boldsymbol{Q}\boldsymbol{k} \end{aligned} \tag{6.8}$$

And the final expression

$$\boldsymbol{F}_1(\boldsymbol{k}) = \mathrm{j}\boldsymbol{m} \times \boldsymbol{k} - \frac{\omega}{2}\boldsymbol{Q}\boldsymbol{k} \tag{6.9}$$

where

$$\boldsymbol{m} = \frac{1}{2}\int_{\boldsymbol{r}'\in S} (\boldsymbol{r}' \times \boldsymbol{J}_\mathrm{s}(\boldsymbol{r}'))\,\mathrm{d}S \tag{6.10}$$

is the *magnetic dipole moment* and

$$\boldsymbol{Q} = \frac{1}{\mathrm{j}\omega}\int_{\boldsymbol{r}'\in S} (\boldsymbol{r}'\boldsymbol{J}_\mathrm{s}^\top(\boldsymbol{r}') + \boldsymbol{J}_\mathrm{s}(\boldsymbol{r}')\boldsymbol{r}'^\top)\,\mathrm{d}S \tag{6.11}$$

represents the *electric quadrupole moment*.
It should be mentioned that in (6.11) $\boldsymbol{r}'$ and $\boldsymbol{J}_\mathrm{s}$ are column vectors and $\boldsymbol{r}'^\top$, $\boldsymbol{J}_\mathrm{s}^\top$ are row vectors.
In as much as these moments approximate the current density distribution in the device, chassis mode resonances can be analyzed in terms of frequency dependence of these quantities. Moreover, each moment corresponds to a readily visualized "generic mode" with a well known radiation pattern. To investigate the properties of the chassis, undisturbed by the frequency dependence of the exciting antenna element, a generic excitation must be applied. Plane wave excitation is the method of choice and mostly sufficient to excite the subset of modes which is of the interest for the far-field properties, although it muss be kept in mind that resonant modes which are orthogonal to a constant field remain hidden. Provided that the electromagnetic analysis software used supports file output of calculated current densities, the numerical evaluation of (6.6)-(6.11) amounts to a straightforward data post-processing step. In the present work IE3D and NEC2 were used, the latter becaused its well documented text based interface largely facilitates batch processing for large set of variable geometrical parameters. The only point which must be taken care of is the dependence of (6.9) on the choice of the origin of the coordinate system. Shifting the origin along the $\boldsymbol{k}$-direction affects not only the phase but also the magnitude of (6.9). The physically meaningful choice of origin is the one which minimizes $|\boldsymbol{F}_1(\boldsymbol{k})|$. In this case $\boldsymbol{F}_1(\boldsymbol{k})$ is orthogonal to $\boldsymbol{F}_0$. The proper result can directly be obtained by orthogonalisation.
The second order moment as specified in (6.7) can be expressed in a new coordinates system follows

$$\begin{aligned}
\boldsymbol{F}_1^O(\boldsymbol{k}) &= \mathrm{j}\int_{\boldsymbol{r}'\in V} \boldsymbol{J}_\mathrm{s}(\boldsymbol{r}')(\boldsymbol{k}\cdot\overrightarrow{OA} + \boldsymbol{k}\cdot\overrightarrow{AM})\,\mathrm{d}V \\
&= \mathrm{j}\boldsymbol{k}\cdot\overrightarrow{OA}\int_{\boldsymbol{r}'\in V} \boldsymbol{J}_\mathrm{s}(\boldsymbol{r}')\,\mathrm{d}V + \mathrm{j}\int_{\boldsymbol{r}'\in V} \boldsymbol{J}_\mathrm{s}(\boldsymbol{r}')(\boldsymbol{k}\cdot\overrightarrow{AM})\,\mathrm{d}V \\
&= \mathrm{j}(\boldsymbol{k}\cdot\overrightarrow{OA})\boldsymbol{F}_0(\boldsymbol{k}) + \boldsymbol{F}_1^A(\boldsymbol{k})
\end{aligned} \tag{6.12}$$

where O represents the origin of the original coordinates system and A the origin of the new one. For an invariant $\boldsymbol{F}_1(\boldsymbol{k})$, the coefficient $\alpha = \boldsymbol{k} \cdot \overrightarrow{OA}$ should be zero or determined such that the magnitude $|\boldsymbol{F}_1(\boldsymbol{k})|$ is minimized.
This is traduced by

$$|\boldsymbol{F}_1(\boldsymbol{k}) - \mathrm{j}\alpha \boldsymbol{F}_0(\boldsymbol{k})| \longrightarrow min$$

and implies

$$\alpha = \frac{\mathrm{Im}\{\boldsymbol{F}_0 \boldsymbol{F}_1{}^*\}}{|\boldsymbol{F}_0(\boldsymbol{k})|^2}$$

which leads to the following assignment irrespective of the original choice of origin.

$$\boldsymbol{F}_1(\boldsymbol{k}) \leftarrow \boldsymbol{F}_1(\boldsymbol{k}) + \mathrm{j}\frac{\mathrm{Im}\{\boldsymbol{F}_0 \boldsymbol{F}_1{}^*\}}{|\boldsymbol{F}_0(\boldsymbol{k})|^2}\boldsymbol{F}_0(\boldsymbol{k}) \tag{6.13}$$

6.2 Application to Bar-Type Phone Chassis

From the geometrical form of the chassis in this case of mobile phones which is similar to a dipole, it is obvious that for the analysis of its radiation properties the first order moment (electrical dipole moment) is much more appropriate. A perfectly conducting rectangular board is considered and simulations are performed for different widths w and lengths l. Fig. 6.1 illustrates the approach investigated in previous sections for a simple rectangular board of length l and width $w < l$. For these simulations, plane wave polarized in the broadside (z-direction) at frequencies near the halfwavelength resonance has been used.
To easily have a feeling of the radiation properties, we define two parameters from the *first order moment* graphs as displayed in Fig. 6.1 namely, the *resonance frequency* and the *radiation quality factor*.
The resonance frequency corresponds to the frequency which produces the maximum in magnitude of the first order moment.
The radiation quality factor is related to the $3\,\mathrm{dB}$ relative bandwidth around the resonance frequency.

Fig. 6.2 clearly shows the effects of the board dimensions on the resonance frequency. For small width-to-length ratios, the board almost have the structure of a wire and by neglecting the width the obtained resonance frequency is approximately $c_0/2l$ and otherwise $c_0/2(l + w)$. Fig.6.3 shows the $3\,\mathrm{dB}$ relative bandwidth dependence on the dimensions of the rectangular. It outlines the growth of the width with the bandwidth, which is not a surprising.
The frequency dependence of the dipole mode exposed by $\boldsymbol{F}_{0,z}$ is in excellent agreement

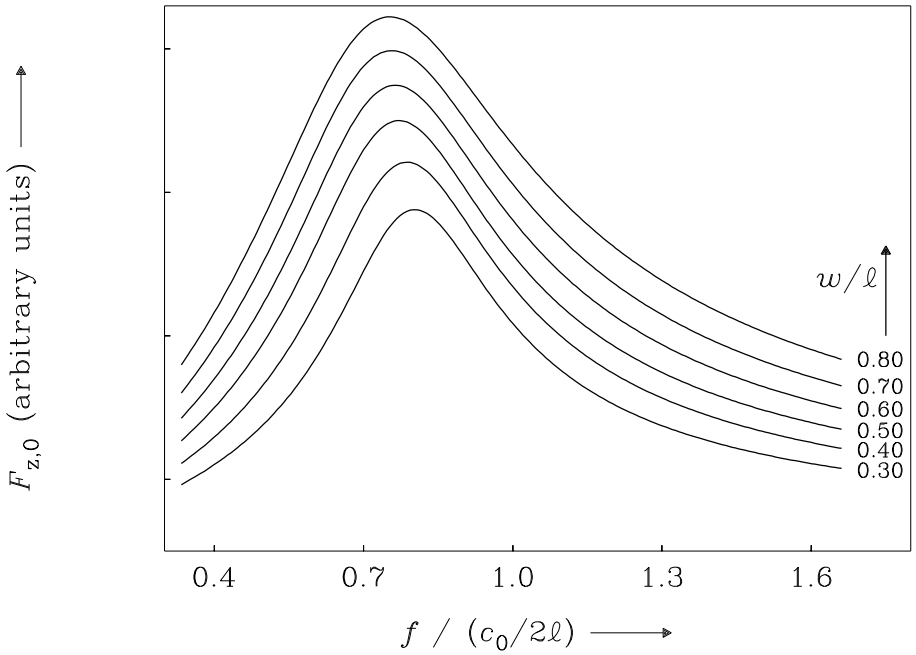

Figure 6.1: Frequency dependence of the co-polarized component $\boldsymbol{F}_{0,z}$ of (6.6) for a rectangular board with dimensions l (along z) and $w < l$.

with the resonator model

$$\boldsymbol{F}_{0,z} = \frac{A}{1 + \mathrm{j}Q\left(\frac{f}{f_0} - \frac{f_0}{f}\right)} \tag{6.14}$$

A least square fit of (6.14) to the post-processed results delivers the resonance frequency of the mode, its radiation quality factor Q and a relative amplitude of excitation. To obtain these results it is sufficient to perform the calculations for a few frequency points only. Note that the resonance frequency f_0 and the frequency f_{max}, where (6.4) attains its maximum are not the same but related via

$$f_{max} = \frac{Q}{\sqrt{Q^2 - \frac{1}{2}}} f_0 \tag{6.15}$$

6.2.1 Electrical Length Extension

Knowing that utilization of a resonant chassis mode greatly facilates excitation of spatially extended current distribution it is of high interest to investigate the tuning of chassis modes. The case of a bar-type structure intended for multiband operation in the GSM850, GSM900

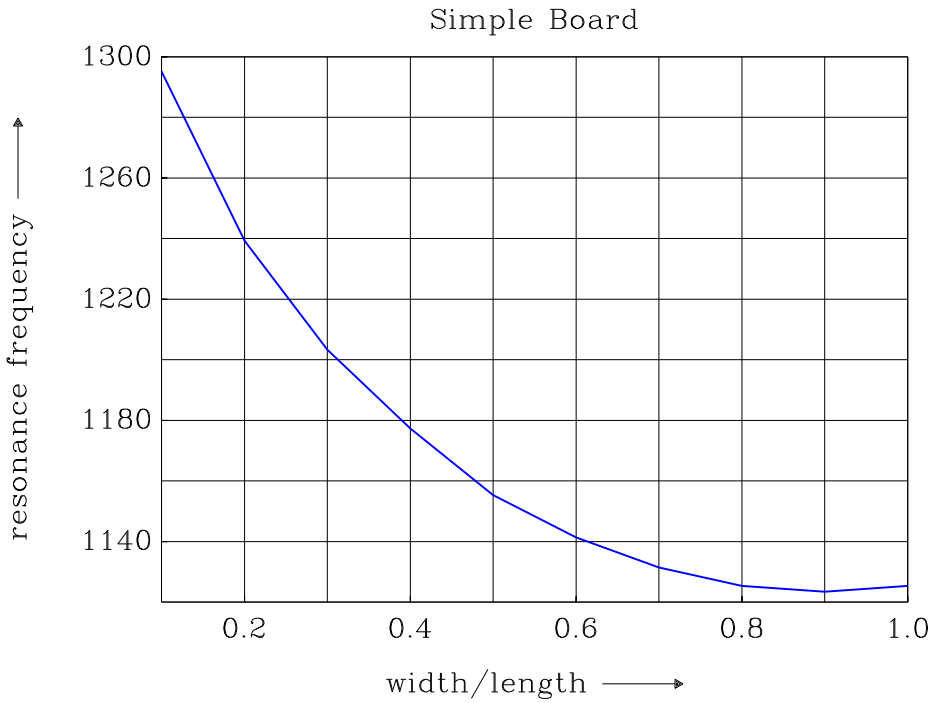

Figure 6.2: Resonance frequency dependence on the dimensions length (l) and width (w) of a rectangular board.

"low-band" and in the DCS1800 and PCS1900 bands "high-band" is considered. From data produce for the graphs in Fig. 6.1, the chassis resonance frequency for the ratio 0.4 lies at $1140\,\mathrm{MHz}$. This means that the chassis is too short for an optimal low-band performance (resonance) and too long for an optimal high-band performance (resonance). The new approach presented permits optimization of radiation properties in two bands by simultaneous extension and reduction of electrical lengths with respct to the two bands. Note, however, that optimization of free-space radiation properties muss be traded off against compliance with SAR limits, and aspect which is ignored here because of simplicity.
The electrical length of a chassis can be extended by capacitive or inductive loading. For a capacitively loaded loaded structure according to Fig. for instance, electrical length (with respect to the first resonance) was found to be approximated within $\approx 2\%$ error by

$$\frac{\ell_{\text{eff}}}{\ell} \approx 0.96 + 0.4234\left(\frac{w}{\ell}\right)^{0.3034} + 0.3926\frac{a}{\ell} + 1.4574\frac{h}{\ell} + 2.5143\frac{ah}{\ell^2} - 0.2581\frac{(a+h)w}{\ell^2} \quad (6.16)$$

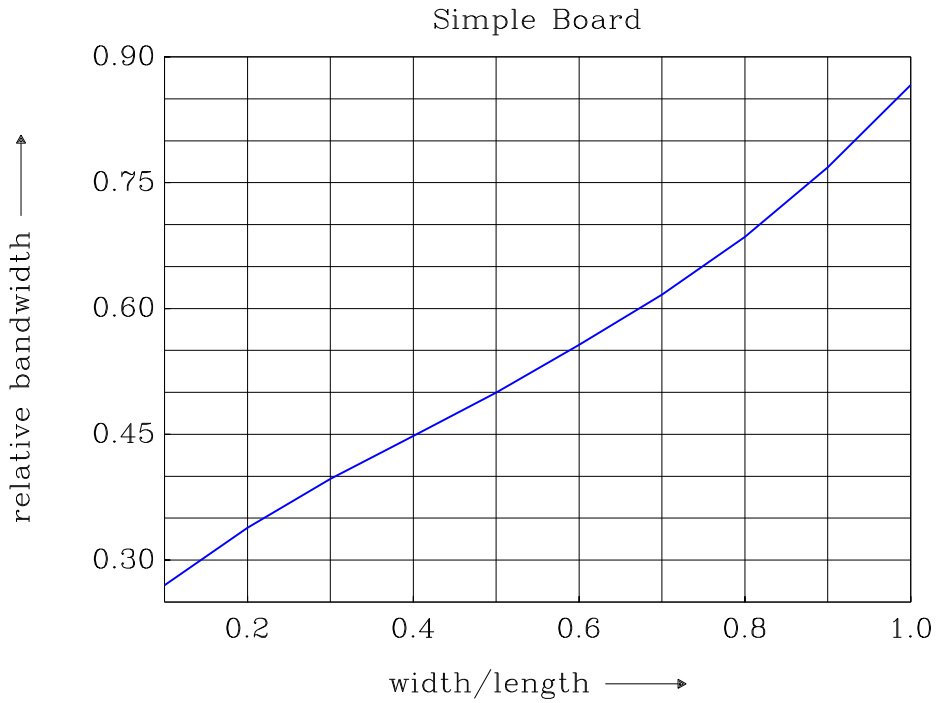

Figure 6.3: Relative 3dB bandwidth dependence on the dimensions length (l) and width (w) of a rectangular board.

within the parameter range $0.3 \leq w/\ell \leq 0.8$, $0.04 \leq h/\ell \leq 0.2$ and $0 \leq a/\ell \leq 0.2$. Fig. 6.4b shows the effects for $l = 100\,\mathrm{mm}$ and $a = 15\,\mathrm{mm}$. Capacitive loading is seen to be an effective means to lower the dipole type resonance, e.g. by more than 20% with respect to an unloaded board for $h = 16\,\mathrm{mm}$ and $w = 40\,\mathrm{mm}$. Its excitation by means of a small antenna element is hereby enhanced although the radiation quality factor is the same time increased from approximately 2.2 to 3.

6.2.2 Dual Band Chassis Mode Tuning

Simultaneous tuning of two different chassis resonances is illustrated in Figs. 6.5 and 6.6 . A $100\,\mathrm{mm} \times 40\,\mathrm{mm}$ board is capacitively loaded at both ends, but at one end, the load is designed as a wave trap for the DCS and PCS bands. The wave trap acts as a resonant quarter-wave slot resonator in high-band, thereby impressing a current density zero at its open ends. A dipole-type resonance is observed along the the part of the board uncovered by the wave traps. The slot has a total length of $45\,\mathrm{mm}$ in this example whereof $35\,\mathrm{mm}$ are parallel to the long edges of the board. Since currents along the slot mostly compensate, the radiation from the part of the board covered by the wave traps is small in high-band

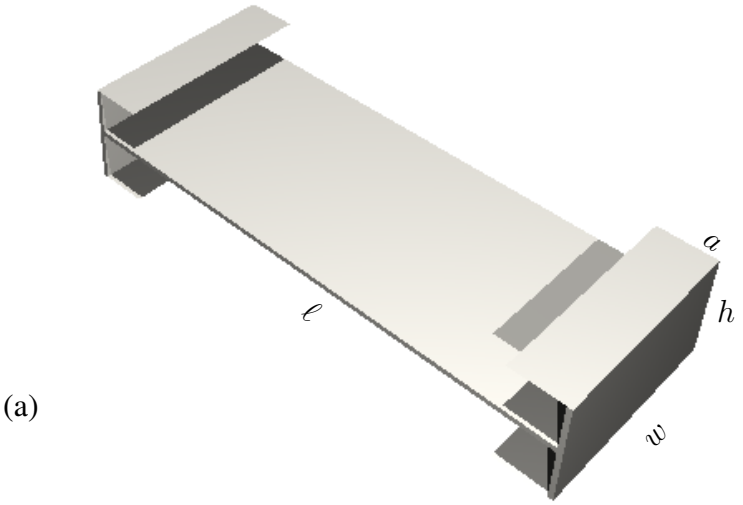

(a)

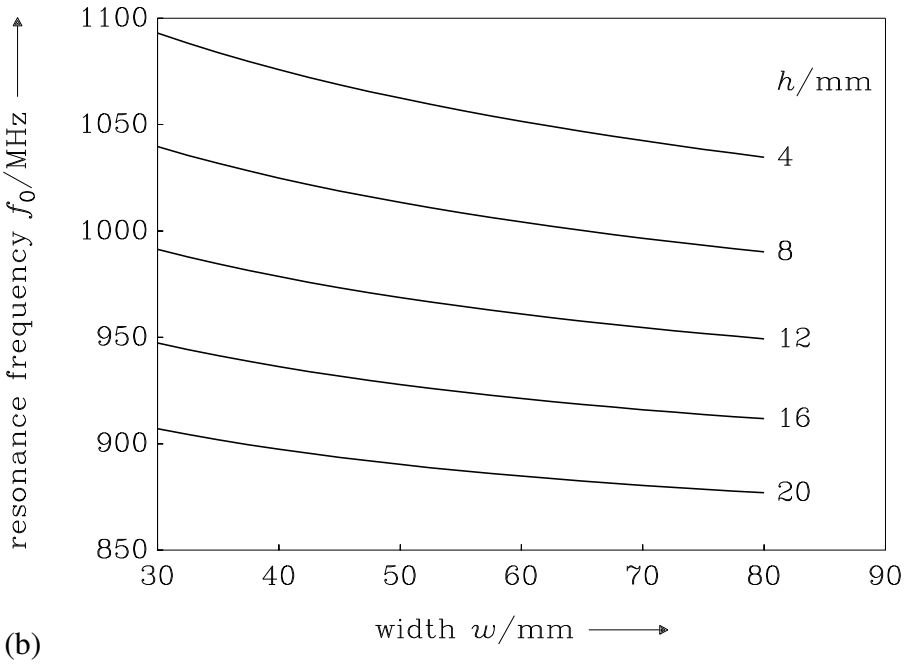

(b)

Figure 6.4: Capacitive loading: (a) structure example, (b) design chart for resonance tuning ($\ell = 100\,\mathrm{mm}$, $a = 15\,\mathrm{mm}$).

and an almost perfect dipole is observed both bands. Fig. 6.6 displays the first moment of

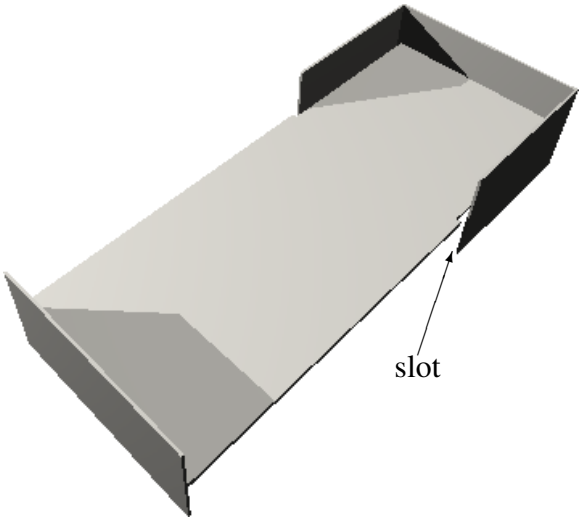

(a)

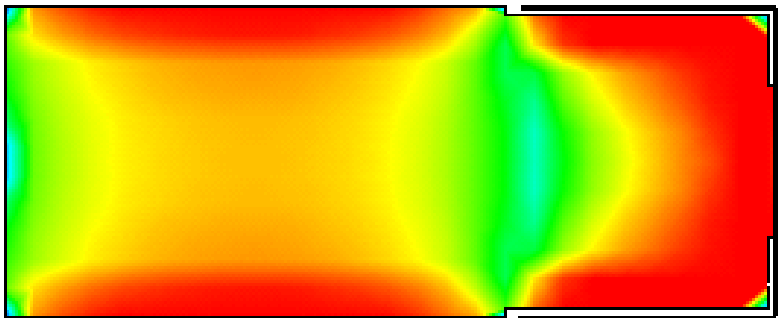

(b)

Figure 6.5: Electrical length reduction and pattern shaping by resonant screen: (a) structure, (b) current density at 1780 MHz.

the radiation vector (6.6) along the long axis of the structure, clearly exhibiting the dual-resonant behaviour.

6.3 Application to Folder-Type Phone Chassis

To illustrate the versatility of the approach presented in section 6.1 for investigation of not only electric dipole type but also magnetic dipole type resonances and their mutual

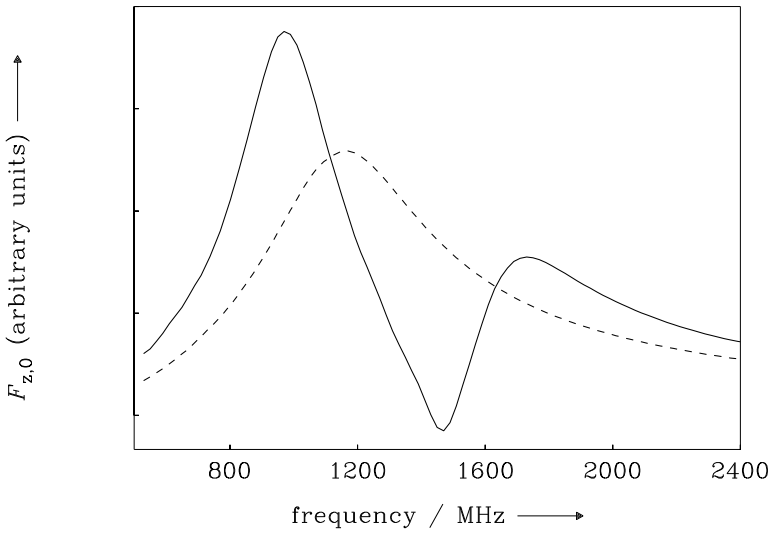

Figure 6.6: Dual-resonant behaviour of $F_{z,0}$ according to (6.6) for the structure given in Fig. 6.5. Dashed line corresponds to unloaded board.

coupling, a generic folder-type phone chassis is considered. Two cases of study should be considered for a puposeful and accurate investigation of the radiation properties: the open and closed state. In both cases, a perfectly conducting metallic plate is assumed for simulations. We first investigate the radiation properties in the closed state.

6.3.1 Folder-Type Chassis in Closed State

(Fig. 6.7) shows the closed state of the structure.
For analysis, magnitudes of different components of the first (6.6) and second (6.7) order moment are presented. Fig. 6.8 depicts the magnitude of the x-components of the first F_0 and second F_1 order moment and of the radiation vector F, which represents all the moments. Comparison of Fx with individual moments provides the deviation and gives some hints about the effectiveness of the method. A sharp peak (blue curve) of the magnetic dipole moment $F_{1,x}$ at $1.1\,\mathrm{GHz}$, due to the asymmetry of the structure is visible and represents the quarter-wave parallel plate mode resonance. A comparasion with results obtained by making use of the theory of characteristic modes, which shows the first resonance at $1.13\,\mathrm{GHz}$ confirms the results obtained here. One should also observe an excitation of a strong electric dipole moment which dominates the radiation since a comparasion between

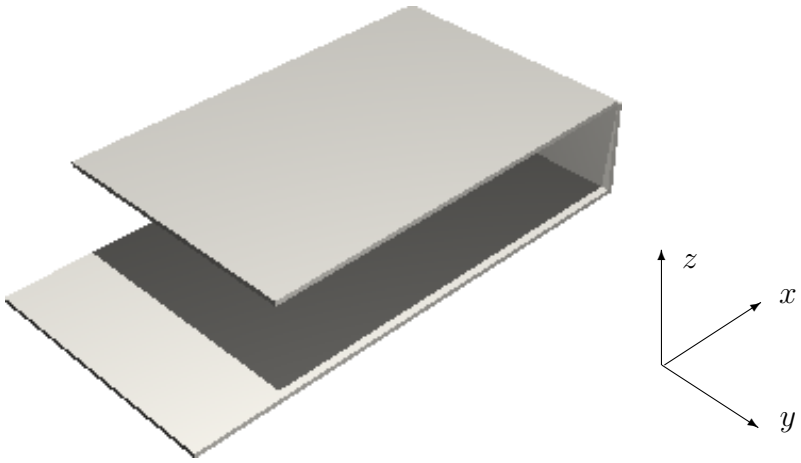

Figure 6.7: Generic closed folder type structure: lower board $70 \times 35\,\mathrm{mm}^2$, upper board $50 \times 35\,\mathrm{mm}^2$, height $15\,\mathrm{mm}$.

$|F_{0,x}|$ and $|F_x|$ shows an unsignificant deviation in almost the whole frequency range.

Fig. 6.9 diplays the magnitude of the y-component of the radiation vector $|F_y|$ which includes all moments as well as the magnitudes of the associated first and second order moment. Its inspection confirms not only the first resonance already mentioned in the analysis of the x-components but also exhibits another magnetic resonance at approximately $3.2\,\mathrm{GHz}$. This is in agreement with the result obtained from characteristic modes. One should also specify a strong excitation of the electrical dipole moment in the frequency range around $1.5\,\mathrm{GHz}$.

Fig. 6.10 displays the magnitude $|F_z|$ of the z-component of the radiation vector as well as the magnitudes $|F_{0,z}|$ and $|F_{1,z}|$ of the first and second order moment respectively. The electric and magnetic fields are orthogonal to the z direction which is the direction of polarization of the excitation field and explains the remarkable decrease in magnitudes of different moments. The magnetic moment has almost completely vanished and the electric dipole moment which presents no deviation from $|F_z|$ and exhibits a resonance at around $1.1\,\mathrm{GHz}$ dominates the radiation.

A comparison with results obtained by making use of the characteristic modes indicates the absence of the third and fourth resonances in the results of the approach presented here. It should be emphasized that results obtained with the approach presented in this chapter are dependent on the polarization of the excitation field.

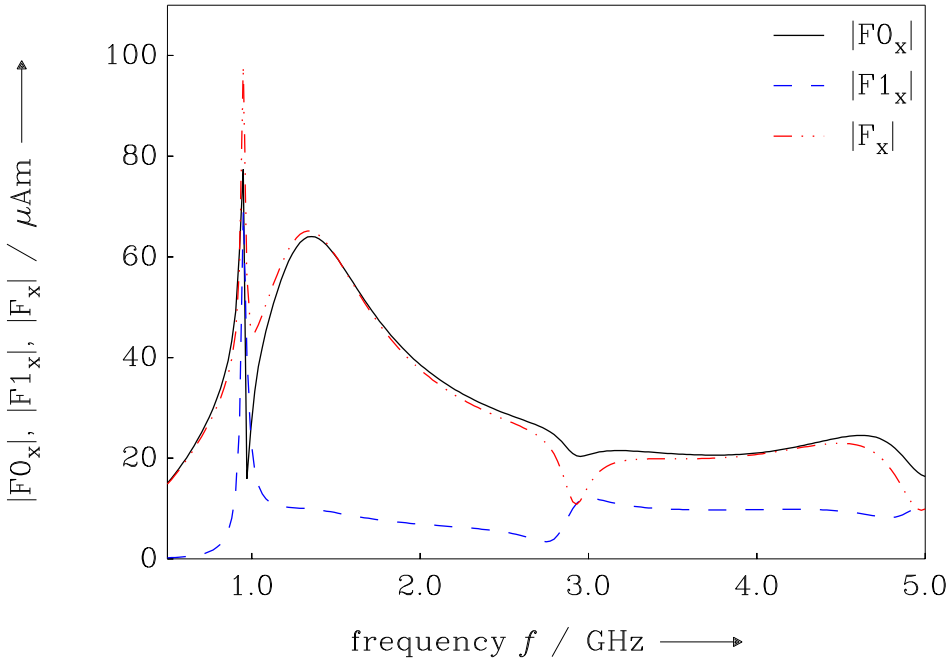

Figure 6.8: Moments $|F_{0,x}|$ (black), $|F_{1,x}|$ (blue) and $|F_x|$ (red) for structure according to Fig. 6.7 under broad-side z-polarized plane wave illumination for $\boldsymbol{k}$ along x–direction.

6.3.2 Folder-Type Chassis in Open State

Fig. 6.11 shows a generic model of a folder type mobile phone in open state. As before a perfectly conducting chassis is assumed with dimensions of flip and base part as previously specified in the closed state case. For radiation properties analysis, the first(6.6) and second (6.7) order moment have been investigated although the chassis geometry is closed to that of a dipole. For each moment, magnitudes of different components are presented.

Fig. 6.12 shows the magnitudes of the x-component of the first and second order moment. Plane wave chosen for illumination is z-polarized and $\boldsymbol{k}$ oriented along the x-direction. A strong electrical dipole moment is observed and reaches its maximum at around $850\,\mathrm{MHz}$ which represents a resonance. This is a bit shifted from the resonance at $1052\,\mathrm{MHz}$ obtained with the theory of characteristic modes. Maxima of the first and second moments

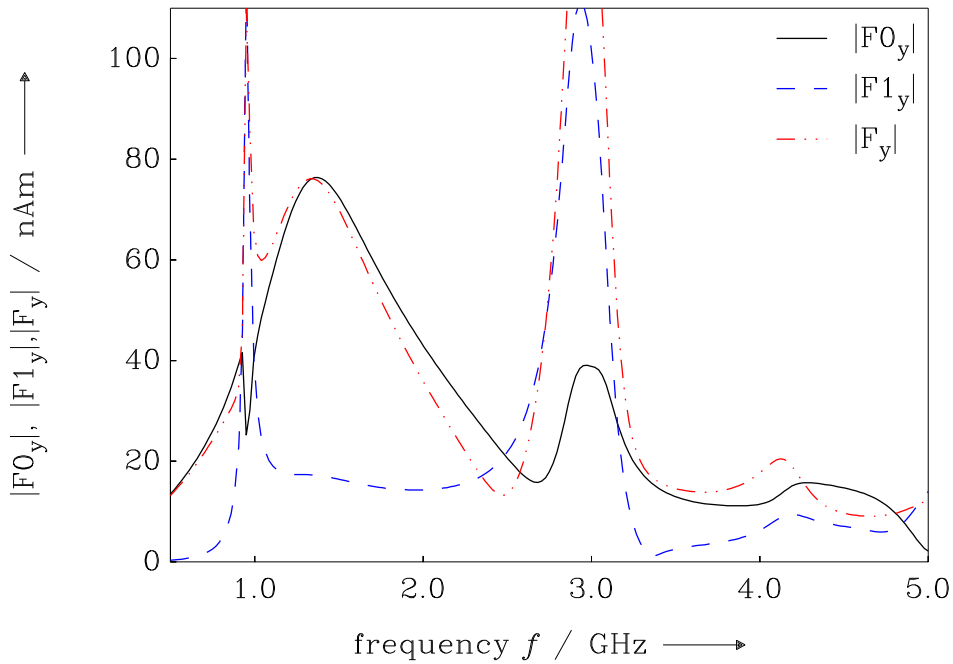

Figure 6.9: Moments $|F_{0,y}|$ (black), $|F_{1,y}|$ (blue) and $|F_y|$ (red) for structure according to Fig. 6.7 under broad-side z-polarized plane wave illumination for $\boldsymbol{k}$ along x–direction.

are observed at around $2.2\,\mathrm{GHz}$ representing another resonance. Comparison with the result from the theory of characteristic modes shows a λ-resonance with respect to the major axis at that frequency.

The magnitude of the y-component of the radiation vector in terms of first and second order moment is not represented as figure because they are almost zero. The radiation vector with $\boldsymbol{k}$ in the y-direction completely vanishes is explained by the fact that the electric excitation field is transverse to the y-direction and causes its coefficients to be almost zero. This clearly means that no current has been excited in the direction tranverse to the major axis.

Fig. 6.13 represents the magnitudes of the z-component of the radiation vector in terms of first and second order moment. The magnitude of the first order moment shows a maximum at around $850\,\mathrm{MHz}$ which represents a resonance. Refering to the analysis provided by the

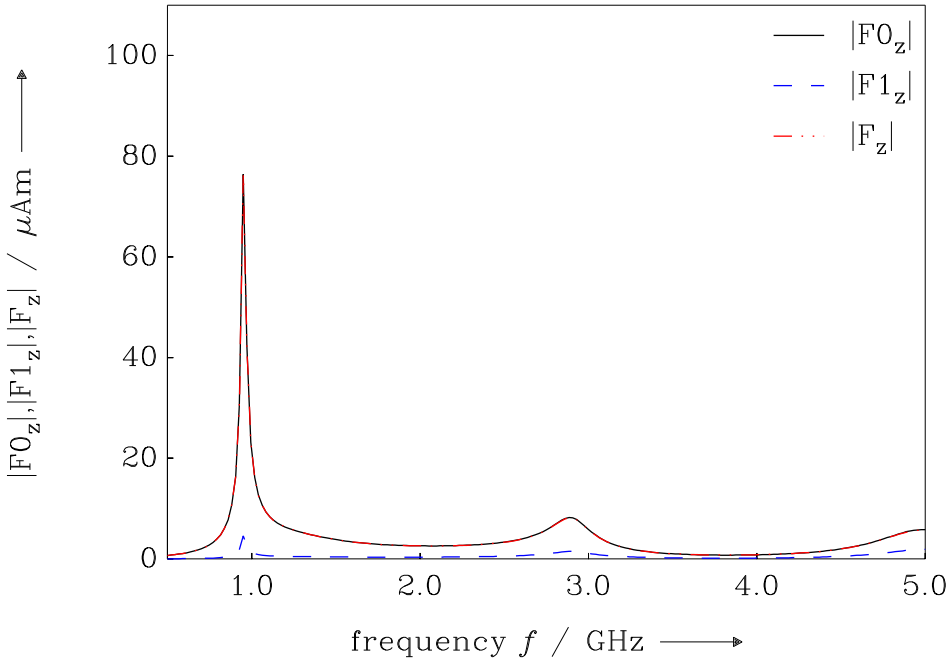

Figure 6.10: Moments $|F_{0,z}|$ (black), $|F_{1,z}|$ (blue) and $|F_z|$ (red) for structure according to Fig. 6.7 under z-polarized plane wave illumination for $\boldsymbol{k}$ along z–direction.

theory of characteristic, this corresponds to the λ-resonance around the major axis. A minimum of the same quantity is observed at around $2.2\,\mathrm{GHz}$ and as already mentioned in the analysis of $\boldsymbol{F}_x$, this resonance corresponds to the $\lambda/2$-resonance. The magnitude of the second order moment does not show any particularities and its values are relatively unsignificant.

6.4 Conclusion

Analysis of chassis radiation properties by making use of this simplified method yields results closed to those obtained with the theory of characteristic modes. It has the drawback that its results depend on the polarization of the excitation field and provide only results in the direction of polarization. This is clearly observed in examples handled in previous

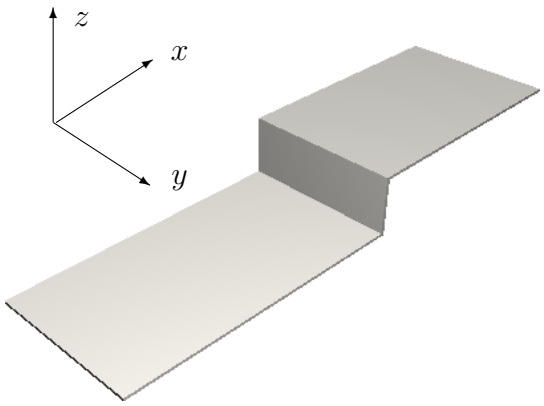

Figure 6.11: Generic open folder type structure: lower board $70 \times 35\,\mathrm{mm}^2$, upper board $50 \times 35\,\mathrm{mm}^2$, height $15\,\mathrm{mm}$.

sections. In all cases of mobile phone chassis simulated, the electrical excitation field is polarized in the direction of the major axis and only resonances with respect to that axis have been obtained. In fact, in the above simulated frequency range, the theory of characteristic modes shows up four resonance frequencies instead of two with the simplified method. The two extra resonance frequencies are related to the minor axis and are obviously invisible with the simplified method. It has the advantage, that it can be easily implemented by post-processing output data from CEM software packages.

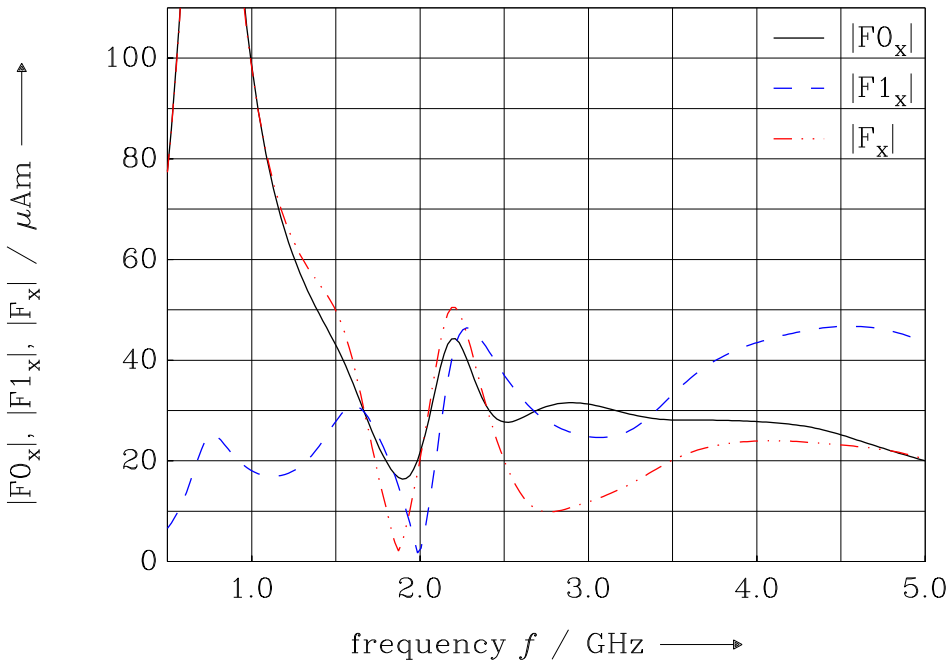

Figure 6.12: Moments $|F_{0,x}|$ (black), $|F_{1,x}|$ (blue) and $|F_x|$ (red) for structure according to Fig. 6.11 under z-polarized plane wave illumination for $\boldsymbol{k}$ along x–direction.

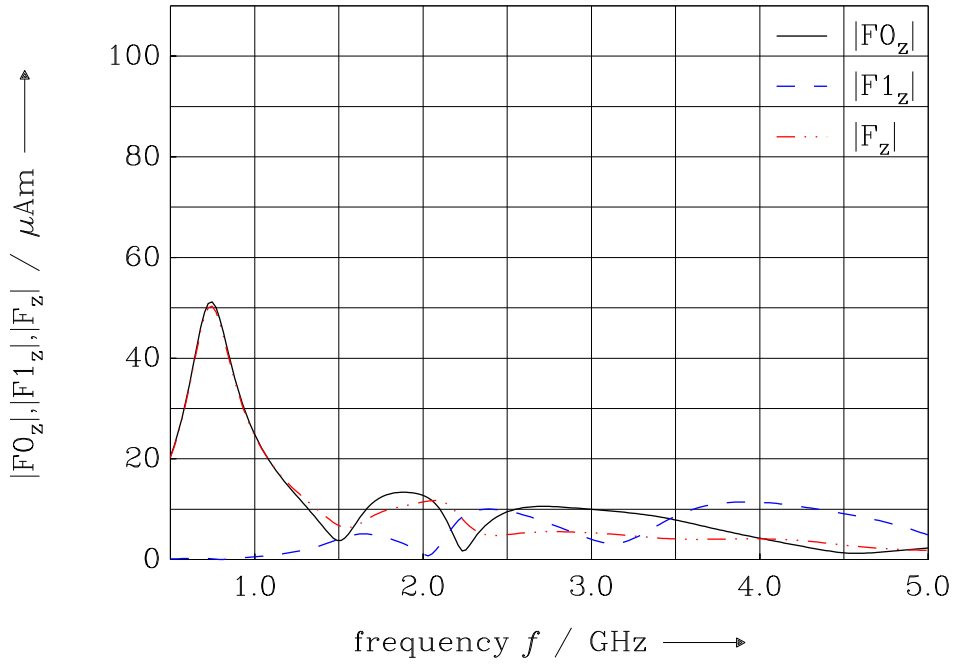

Figure 6.13: Moments $|F_{0,z}|$ (black), $|F_{1,z}|$ (blue) and $|F_z|$ (red) for structure according to Fig. 6.11 under z-polarized plane wave illumination for $\boldsymbol{k}$ along z–direction.

Chapter 7

Conclusions

THIS DISSERTATION has explored the interaction between an electrically small antenna element and the conductive chassis of a handheld radio device, such as mobile phone on which it is mounted. The antenna-chassis coupling problem, which has so far mainly been handled in terms of equivalent circuits is here discussed on a field theoretical level. A new concept for the solution of the problem has been introduced, which separately considers chassis and antenna element as two distinctive entities and investigates the radiation characteristics of the chassis on its own by making use of the theory of characteristic modes. From this point of view, an optimal design and location of the antenna element can be obtained through the knowledge of the chassis radiation properties. In this case the antenna element is only used as exciter or coupler for the chassis.

For the evaluation of characteristic modes on the surface of conducting chassis, an algorithm and a corresponding software have been developed. Analysis of radiation characteristics for a bar-type (monoblock) phone widely spread on the market with dimension $100\,\mathrm{mm} \times 40\,\mathrm{mm}$ exhibits its first resonance characteristic mode corresponding to the $\lambda/2$ dipole mode with respect to the major axis at $1.33\,\mathrm{GHz}$. As it can be observed this insight clearly means that the chassis is to short for operating with GSM800 and very large to operate for GSM1800. For an antenna developer, an effective solution operating at low- as well as high-band requires a simultaneous extension and reduction of the chassis electrical length. A solution to this problem was proposed in the last chapter of this thesis.
Once the radiation characteristics of the chassis have been determined, a future challenge will be to modified whenever necessary the geometry of the chassis to comply with the given requirements and therefore improve the radiation performance.
The theory of characteristic modes considers a current density induced on the surface of a conducting body by an external field as a linear superposition of characteristic modes. In the frame of this work, the maximization of the excitation coefficient which measures the reaction of the excitation field on a given characteristic mode, provides the optimal

location of the coupler on the chassis to effectively excite that given mode. In this work, focus has been on the optimization of the coupling between antenna element and chassis. This requires an effective excitation of a chassis resonant characteristic mode. However, this does not consider the user interaction and SAR minimization. For future research, a characteristic mode should be found which is a trade-off between optimal coupling and SAR reduction.

A great feature of characteristic modes is their patterns orthogonality. Analysis in the case of bar-type phones shows at around $2.4\,\mathrm{GHz}$ ISM band the availability of three characteristic modes almost resonant. This means the potential of the effectiveness for their excitation is very high. This observation is very interesting for the design of MIMO antenna systems on mobile phones.

Actual CEM softwares don't have the characteristic modes solver at their disposition. To circumvent such a problem, a simplified method for the evaluation of radiation properties is propsosed. Comparison of results from the simplified method with simulation results obtained by applying the theory of characteristic mode shows concordances. The drawback of the simplified method lies in the fact that its results depend on the nature excitation.

Appendix A

Algorithms for Matrix Decomposition

A.1 Definition and Notations

The *generalized eigenvalues* of a matrix pair $(\boldsymbol{A}, \boldsymbol{B}) \in \mathbb{R}^{n\times n} \times \mathbb{R}^{n\times n}$ are the roots (α, β) of the bivariate polynomial $\det(\beta\boldsymbol{A} - \alpha\boldsymbol{B})$.
The set of all eigenvalues (α, β) is denoted by $\lambda(\boldsymbol{A}, \boldsymbol{B})$.
A non zero vector $\boldsymbol{x} \in \mathbb{C}^n$ is called a *right generalized eigenvector* of $(\boldsymbol{A}, \boldsymbol{B})$
if $\beta\boldsymbol{A}\boldsymbol{x} = \alpha\boldsymbol{B}\boldsymbol{x}$ for some $(\alpha, \beta) \in \lambda(\boldsymbol{A}, \boldsymbol{B})$.
Correspondingly, a nonzero vector $\boldsymbol{z} \in \mathbb{C}^{n\times n}$ satisfying $\beta\boldsymbol{z}^H\boldsymbol{A} = \alpha\boldsymbol{z}^H\boldsymbol{B}$ is called a *left generalized eigenvector*.
A k-dimensional subspace $\mathcal{X}$ is called a *right deflating subspace* of $(\boldsymbol{A}, \boldsymbol{B})$
if $\boldsymbol{A}\mathcal{X}$ and $\boldsymbol{B}\mathcal{X}$ are contained in a subspace $\mathcal{Y}$ of dimension k. The regularity of $(\boldsymbol{A}, \boldsymbol{B})$ implies that such a subspace $\mathcal{Y}$ is uniquely defined; we call $\mathcal{Y}$ a *left deflating subspace* and $(\mathcal{X}, \mathcal{Y})$ a *pair of deflating subspace*. It is important to remark that $\mathcal{Y}$, despite its name, is generally not spanned by a left eigenvectors.

Definition Hessenberg-Triangular Form

A matrix pair $(\boldsymbol{A}, \boldsymbol{B})$ is said to be in *Hessenberg-triangular form* if $\boldsymbol{A}$ is an upper Hessenberg matrix and $\boldsymbol{B}$ is a nonsingular upper triangular matrix.

Theorem A.1.1
$\mathcal{X}$ and $\mathcal{Y}$ are defined as above. If the columns of $\boldsymbol{X}$ and $\boldsymbol{Y}$ form bases for $\mathcal{X}$ and $\mathcal{Y}$, respectively, then there exists a uniquely defined matrix pair $(\boldsymbol{A}_{11}, \boldsymbol{B}_{11})$ satisfying

$$\boldsymbol{A}\boldsymbol{X} = \boldsymbol{Y}\boldsymbol{A}_{11},\ \boldsymbol{B}\boldsymbol{X} = \boldsymbol{Y}\boldsymbol{B}_{11}$$

The *Generalized Block Schur Decomposition* is a direct consequence of the previous theorem (A.1.1).

Corollary A.1.1 (Generalized Block Schur Decomposition)
Let $(\mathcal{X}, \mathcal{Y})$ be a pair of deflating subspaces and let the columns of $\boldsymbol{X}, \boldsymbol{X}^{\perp}, \boldsymbol{Y}, \boldsymbol{Y}^{\perp}$ form orthonormal bases of $\mathcal{X}, \mathcal{X}^{\perp}, \mathcal{Y}, \mathcal{Y}^{\perp}$ respectively. Then $\boldsymbol{U} = \left[\boldsymbol{X}, \boldsymbol{X}^{\perp}\right]$ and $\boldsymbol{V} = \left[\boldsymbol{Y}, \boldsymbol{Y}^{\perp}\right]$ are unitary matrices with

$$\boldsymbol{U}^{H} \cdot (\boldsymbol{A}, \boldsymbol{B}) \cdot \boldsymbol{V} = \left(\begin{bmatrix} \boldsymbol{A}_{11} & \boldsymbol{A}_{12} \\ 0 & \boldsymbol{A}_{22} \end{bmatrix}, \begin{bmatrix} \boldsymbol{B}_{11} & \boldsymbol{B}_{12} \\ 0 & \boldsymbol{B}_{22} \end{bmatrix} \right) \tag{A.1}$$

and

$$\lambda(\boldsymbol{A}, \boldsymbol{B}) = \lambda(\boldsymbol{A}_{11}, \boldsymbol{B}_{11}) \cup \lambda(\boldsymbol{A}_{22}, \boldsymbol{B}_{22}) \tag{A.2}$$

The key idea implemented here for computing the generalized eigenvalues and eigenvectors is based on the above meaningful decomposition. In this context a useful application of the above decomposition shows that the generalized eigenvalues can be easily obtained. Namely, by chosing a decomposition which provides matrices on the diagonals $\boldsymbol{A}_{11}, \boldsymbol{B}_{11}, \boldsymbol{A}_{22}, \boldsymbol{B}_{22}$ with dimensions less or equal to two. If the matrices blocks on the diagonal are not with dimensions less or equal to two, subsequent decompositions can be applied for further reduction. The following theorem prooves that such a decomposition do exist.

Theorem A.1.2 (Generalized Real Schur Decomposition [35])
*Let $(\boldsymbol{A}, \boldsymbol{B}) \in \mathbb{R}^{n \times n} \times \mathbb{R}^{n \times n}$, then there exist orthogonal matrices $\boldsymbol{Q}$ and $\boldsymbol{Z}$ so that $\boldsymbol{Q}^{T} \cdot (\boldsymbol{A}, \boldsymbol{B}) \cdot \boldsymbol{Z} = (\boldsymbol{S}, \boldsymbol{T})$, where $\boldsymbol{S}$ is in the **real Schur form** and $\boldsymbol{T}$ upper triangular. $\boldsymbol{S}$ is in the real Schur form means:*

$$\boldsymbol{S} = \begin{bmatrix} S_{11} & S_{12} \cdots & S_{1m} \\ 0 & S_{22} \ddots & \vdots \\ \vdots & \ddots \ddots & S_{m-1m} \\ 0 & \cdots 0 & S_{mm} \end{bmatrix}$$

where all diagonal blocks of $\boldsymbol{S}$ are of order one or two.

A.1.1 The QZ Algorithm

The $\boldsymbol{QZ}$ Algorithm is a numerically backward stable method for computing a real generalized Schur decomposition of a pair $(\boldsymbol{A}, \boldsymbol{B})$. It goes back to Moler and Stewart in 1973 [1].

It generates a sequence of orthogonally equivalent matrix pairs

$$(\boldsymbol{A}_0, \boldsymbol{B}_0) \leftarrow (\boldsymbol{A}, \boldsymbol{B}), (\boldsymbol{A}_1, \boldsymbol{B}_1), (\boldsymbol{A}_2, \boldsymbol{B}_2), \cdots,$$

which, under suitable conditions, converges to generalized block Schur form of $(\boldsymbol{A}, \boldsymbol{B})$.

In the following, we show how the initial matrix pair $(\boldsymbol{A}, \boldsymbol{B})$ of the $\boldsymbol{QZ}$ iteration can be reduced to Hessenberg-triangular form. Without loss of generality, we consider in the matrix pair $(\boldsymbol{A}, \boldsymbol{B})$ the matrix $\boldsymbol{B}$ to be upper triangular, since reducing $\boldsymbol{B}$ to upper triangular form is easy. This is simply done by applying the $\boldsymbol{QR}$-decomposition so that $\boldsymbol{B} = \boldsymbol{QR}$. Multiplying $(\boldsymbol{A}, \boldsymbol{B})$ on the left side by $\boldsymbol{Q}^T$ on obtains

$$\boldsymbol{Q}^T \cdot (\boldsymbol{A}, \boldsymbol{B}) = (\boldsymbol{Q}^T \boldsymbol{A}, \boldsymbol{R})$$

where $\boldsymbol{R}$ is an upper triangular matrix.

Reduce a matrix pair to Hessenberg-triangular form using the $\boldsymbol{QZ}$ iteration amounts to the computation of the matrices $\boldsymbol{Q}$ and $\boldsymbol{Z}$ so that

$$\boldsymbol{Q}^T \cdot (\boldsymbol{A}, \boldsymbol{B}) \cdot \boldsymbol{Z} = \left(\begin{bmatrix} \diagdown & \diagdown \\ \diagdown & \diagdown \end{bmatrix}, \begin{bmatrix} \diagdown & \diagdown \\ & \diagdown \end{bmatrix} \right) \tag{A.3}$$

The difficulty of this transformation lies in reducing $\boldsymbol{A}$ to Hessenberg form while keeping the upper triangular form of $\boldsymbol{B}$. This difficulty is circumvented by making use of elementary orthogonal transformations that act on smaller parts of a matrix. Givens elementary rotations are particularly appropriate for such operations.
An $n \times n$ *Givens elementary rotation* has the form

$$\boldsymbol{G}_{ij}(\theta) = \begin{bmatrix} \boldsymbol{I}_{i-1} & & & & \\ & \cos(\theta) & & \sin(\theta) & \\ & & \boldsymbol{I}_{j-i-1} & & \\ & -\sin(\theta) & & \cos(\theta) & \\ & & & & \boldsymbol{I}_{n-j} \end{bmatrix}$$

for an angle $\theta \in [-\frac{\pi}{2}, \frac{\pi}{2})$. The angle θ can always be chosen such that the j^{th} component of $\boldsymbol{G}_{ij}(\theta)\boldsymbol{x} = 0$ for a given vector $\boldsymbol{x} \in \mathbb{R}^{n \times n}$.

A.1.2 Algorithm for Reduction to Hessenberg-triangular form [1]

Input: *A general matrix* $\boldsymbol{A} \in \mathbb{R}^{n\times n}$ *and an upper triangular matrix* $\boldsymbol{B} \in \mathbb{R}^{n\times n}$

Output: *Orthogonal matrices* $\boldsymbol{Q}, \boldsymbol{Z} \in \mathbb{R}^{n}$. *The matrices* $\boldsymbol{A}$ and $\boldsymbol{B}$ are *overwritten with the upper Hessenberg matrix* $\boldsymbol{Q}^T\boldsymbol{A}\boldsymbol{Z}$ *and the upper triangular matrix* $\boldsymbol{Q}^T\boldsymbol{B}\boldsymbol{Z}$, *respectively.*

$\boldsymbol{Q} \leftarrow \boldsymbol{I}_n, \boldsymbol{Z} \leftarrow \boldsymbol{I}_n$
FOR $j = 1, \cdots, n-2$
FOR $i = n-1, n-2, \cdots, j+1$

$\boldsymbol{G} \leftarrow \boldsymbol{G}_{i,i+1}(\boldsymbol{A}\boldsymbol{e}_j)$
$\boldsymbol{A} \leftarrow \boldsymbol{G}\boldsymbol{A},\ \boldsymbol{B} \leftarrow \boldsymbol{G}\boldsymbol{B},\ \boldsymbol{Q} \leftarrow \boldsymbol{Q}\boldsymbol{G}^T$
$\boldsymbol{G} \leftarrow \boldsymbol{G}_{i+1,i}(\boldsymbol{e}_{i+1}^T\boldsymbol{B})$
$\boldsymbol{A} \leftarrow \boldsymbol{G}\boldsymbol{A},\ \boldsymbol{B} \leftarrow \boldsymbol{G}\boldsymbol{B},\ \boldsymbol{Z} \leftarrow \boldsymbol{Z}\boldsymbol{G}^T$

END FOR
END FOR

Appendix B

Linear Operators

In this chapter, linear operators related to the topic treated in this dissertation is presented.

B.1 Symmetric Operators

The symmetric product of two vector functions defined on a domain V, $\boldsymbol{f}$ and $\boldsymbol{g}$ in a vector space of vector functions is defined as

$$\langle \boldsymbol{f}, \boldsymbol{g} \rangle = \int_V \boldsymbol{f} \cdot \boldsymbol{g} \, \mathrm{d}V \tag{B.1}$$

The following product in the complex Hilbert space of square-integrable vector functions L^2

$$\langle \boldsymbol{f}^*, \boldsymbol{g} \rangle = \int_V \boldsymbol{f}^* \cdot \boldsymbol{g} \, \mathrm{d}V \tag{B.2}$$

defines an *inner product*.
An operator $\widehat{\mathbf{T}}$ defined on the space Hilbert of square-integrable vector functions is said to be *symmetric* if for two vector functions $\boldsymbol{f}$ and $\boldsymbol{g}$ the following relation holds

$$\langle \boldsymbol{f}, \widehat{\mathbf{T}}\boldsymbol{g} \rangle = \langle \widehat{\mathbf{T}}\boldsymbol{f}, \boldsymbol{g} \rangle \tag{B.3}$$

B.2 Hermitian Operators

An operator $\widehat{\mathbf{T}}$ on L^2 is said to be *Hermitian* if

$$\langle \boldsymbol{x}^*, \widehat{\mathbf{T}}\boldsymbol{y} \rangle = \langle \left(\widehat{\mathbf{T}}\boldsymbol{x} \right)^*, \boldsymbol{y} \rangle$$

- The eigenvalues of an Hermitian operator are real
  $\boldsymbol{X}_a$ is an eigenfunction of $\widehat{\mathbf{T}}_a$ with eigenvalue a

$$\widehat{\mathbf{T}}_a \boldsymbol{X}_a = a \boldsymbol{X}_a$$

$$\begin{aligned} \langle \boldsymbol{X}_a{}^*, \widehat{\mathbf{T}}_a \boldsymbol{X}_a \rangle &= \langle \left(\widehat{\mathbf{T}}_a \boldsymbol{X}_a \right)^*, \boldsymbol{X}_a \rangle \\ \langle \boldsymbol{X}_a{}^*, a \boldsymbol{X}_a \rangle &= \langle a^* \boldsymbol{X}_a{}^*, \boldsymbol{X}_a \rangle \\ (a - a^*) \langle \boldsymbol{X}_a{}^*, \boldsymbol{X}_a \rangle &= 0 \end{aligned}$$

  Since $\langle \boldsymbol{X}_a{}^*, \boldsymbol{X}_a \rangle \neq 0$ the last equation shows that $a = a^*$

- The eigenvectors of an Hermitian operator are orthogonal
  $\boldsymbol{X}_a$ and $\boldsymbol{X}_b$ are eigenvectors of $\widehat{\mathbf{T}}$ with eigenvalues a and b respectively. ($a \neq b$)

$$\begin{aligned} \langle \boldsymbol{X}_a{}^*, \widehat{\mathbf{T}} \boldsymbol{X}_b \rangle &= \langle \left(\widehat{\mathbf{T}} \boldsymbol{X}_a \right)^*, \boldsymbol{X}_b \rangle \\ \langle \boldsymbol{X}_a{}^*, b \boldsymbol{X}_b \rangle &= \langle a^* \boldsymbol{X}_a{}^*, \boldsymbol{X}_b \rangle \\ b \langle \boldsymbol{X}_a{}^*, \boldsymbol{X}_b \rangle &= a^* \langle \boldsymbol{X}_a{}^*, \boldsymbol{X}_b \rangle \\ (b - a) \langle \boldsymbol{X}_a{}^*, \boldsymbol{X}_b \rangle &= 0 \end{aligned}$$

  It is clear from the last equation that $\langle \boldsymbol{X}_a{}^*, \boldsymbol{X}_b \rangle = 0$ since $a \neq b$

B.3 Radiation Fields and Related Operators

A given distribution of charges and currents localized in some region of space can generate and radiate electromagnetic waves, which propagate to far distance from the source. It is convenient to work with electric and magnetic *potential* rather the $\boldsymbol{E}$ and $\boldsymbol{H}$ fields themselves. The following Maxwell's equations

$$\mathbf{rot}\, \boldsymbol{E} = -\frac{\partial \boldsymbol{B}}{\partial t}\,, \;\; \mathrm{div}\, \boldsymbol{B} = 0 \tag{B.4}$$

imply the existence of the magnetic and electric potentials, $\boldsymbol{A}(\boldsymbol{r}, t)$ and $\varphi(\boldsymbol{r}, t)$ such that the fields $\boldsymbol{E}$ and $\boldsymbol{B}$ can be obtained by

$$\begin{aligned} \boldsymbol{E} &= -\,\mathbf{grad}\, \varphi - \frac{\partial \boldsymbol{A}}{\partial t} \\ \boldsymbol{B} &= \mathbf{rot}\, \boldsymbol{A} \end{aligned} \tag{B.5}$$

Solution of the Mawell's wave equations for the potentials yields

$$\begin{aligned} \boldsymbol{A}(\boldsymbol{r}) &= \mu \int_V \boldsymbol{J}(\boldsymbol{r}')G(\boldsymbol{r},\boldsymbol{r}')\,\mathrm{d}v \\ \varphi(\boldsymbol{r}) &= \frac{-1}{j\omega\epsilon}\int_V \mathrm{div'}\left(\boldsymbol{J}(\boldsymbol{r}')\right)G(\boldsymbol{r},\boldsymbol{r}')\,\mathrm{d}v \end{aligned} \tag{B.6}$$

where $\boldsymbol{r}$ is the field observation point, $\boldsymbol{r}'$ the source point, V the localized volume in which the charge $\rho(\boldsymbol{r}')$ and current $\boldsymbol{J}(\boldsymbol{r}')$ densities are non-zero and $\mathrm{div'}$ the divergence with respect to $\boldsymbol{r}'$.

$$G(\boldsymbol{r},\boldsymbol{r}') = \frac{e^{-jk|\boldsymbol{r}-\boldsymbol{r}'|}}{4\pi|\boldsymbol{r}-\boldsymbol{r}'|}$$

is the Green's function for the Helmholtz equation.
One obtains by inserting B.6 in the expression of the electric field in B.5

$$\boldsymbol{E}(\boldsymbol{J}) = \frac{1}{j\omega\epsilon}\int_V \boldsymbol{J}(\boldsymbol{r}')\cdot\left[\nabla'\nabla' + k^2\right]G(\boldsymbol{r},\boldsymbol{r}')\,\mathrm{d}v \tag{B.7}$$

where ∇' represents the gradient with repect to $\boldsymbol{r}'$, ε, μ and $k = \frac{\omega}{c}$ ($\varepsilon\mu = 1/c^2$) the permittivity, permeability and wave number respectively.
Introducing the linear operator $\widehat{\mathbf{L}}$ from B.6 as follows

$$\widehat{\mathbf{L}}(\boldsymbol{J}) = j\omega\boldsymbol{A}(\boldsymbol{J}) + \mathbf{grad}\,\varphi(\boldsymbol{J}) \tag{B.8}$$

one obtains

$$\widehat{\mathbf{L}}(\boldsymbol{J}) = -\boldsymbol{E}(\boldsymbol{J})$$

$\widehat{\mathbf{L}}$ is *symmetric* but not *Hermitian*.
It can be proven that its real $\mathrm{Re}(\widehat{\mathbf{L}}) = \frac{1}{2}\left(\widehat{\mathbf{L}} + \widehat{\mathbf{L}}^*\right)$ and imaginary $\mathrm{Im}(\widehat{\mathbf{L}}) = \frac{1}{2\mathrm{j}}\left(\widehat{\mathbf{L}} - \widehat{\mathbf{L}}^*\right)$ parts are real and symmetric and thus Hermitian.

Bibliography

[1] C. B. Moler and G. W. Stewart, "An algorithm for generalized matrix eigenvalue problems," *SIAM J. Numer. Anal.*, , no. 10, pp. 241–256, 1973.

[2] H. Morishita, Y. Kim, and K. Fujimoto, "Design Concept of Antennas for Small Mobile Terminals and the Future Perspective," *IEEE Antennas and Propagation Magazine*, vol. 44, no. 5, pp. 30–43, Oct. 2002.

[3] L. J. Chu, "Physical Limitations of Omni-directional Antennas," *Journal of Applied Physics*, vol. 19, pp. 1163–1175, Dec. 1948.

[4] R. E. Collin and S. Rothschild, "Evaluation of Antenna Q," *IEEE Transactions on Antennas and Propagation*, vol. AP-12, no. 1, pp. 23–27, Jan. 1964.

[5] J. S. McLean, "Re-examination of the Fundamental Limits on the Radiation Q of Electrically Small Antennas," *IEEE Transactions on Antennas and Propagation*, vol. 44, no. 5, pp. 672–676, May 1996.

[6] D. Manteuffel, A. Bahr, D. Heberling, and I. Wolff, "Design Considerations for Integrated Mobile Phones Antennas," *in Eleventh International Conference on Antennas and Propagation, Manchester, UK: IEE*, pp. 252–256, Apr. 2001.

[7] O. Kivekäs, J. Ollikainen, T. Lehtiniemi, and P. Vainikainen, "Bandwidth, SAR, and Efficiency of Internal Mobile Phone Antennas," *IEEE Trans. Electromagn. Comput.*, vol. 46, no. 1, pp. 71–86, Feb. 2004.

[8] E. Antoniono-Daviu, M. Cabedo-Fabres, M. Fernando-Bataller, and J. Herranz-Herruzo, "Analysis of the Coupled Chassis-Antenna Modes in Mobile Handsets," *Proc. IEEE Antannas and Propagation Society Int. Symp. Digest. Monterey: IEEE*, June 2004.

[9] E. Antoniono-Daviu, M.Cabedo-Fabres, M. Ferrando-Bataller, and A. Valero-Noguiera, "Resonant Modes in Antenna Handsets," *Joint COST 273/284 Workshop, Gothenburg, Sweden*, June 2004.

[10] P. Vainikainen, O. Kivekäs J. Ollikainen, and I. Kelander, "Resonator-Based Analysis of the Combination of Mobile Handset Antenna and Chassis," *IEEE Transactions on Antennas and Propagation*, vol. 50, no. 10, pp. 1433–1444, Oct. 2002.

[11] W. L. Schroeder, C. Tamgue Famdie, and Klaus Solbach, "Utilisation and Tuning of the Chassis Modes of Handheld Terminal for the Design of Multiband Radiation Characteristics," *in IEE Conference on Wideband and Multi-band Antennas and Arrays, Birmingham, UK*, September 2005.

[12] C. Tamgue Famdie, W. L. Schroeder, and Klaus Solbach, "Numerical Analysis of Characteristic Modes on the Chassis of Mobile Phones," *European Conference on Antenna and Propagation, Nice, France*, November 2006.

[13] Jussi Rahola and Jani Ollikainen, "Optimal Antenna Placement for Mobile Terminals Using Characteristic Mode Analysis," *European Conference on Antenna and Propagation, Nice, France*, November 2006.

[14] Roger F. Harrington and Joseph R. Mautz, "Theory of Characteristic Modes for Conducting Bodies," *IEEE Transactions on Antennas and Propagation*, vol. AP-19, no. 5, pp. 622–628, Sept 1971.

[15] T. Schmid, O. Egger, and N. Kuster, "Automated E-field Scanning system for Dosimetric Assessments," *IEEE Trans. Microw. Theory Techn.*, vol. 44, no. 1, pp. 105–113, Jan. 1996.

[16] N. Kuster, R. Kästle, and T. Schmid, "Dosimetric Evaluation of Handheld Mobile Communications Equipment with Known Precision," *IEICE Trans. Commun.*, vol. E80-B, pp. 645–652, May 1997.

[17] Q. Yu, O.-P Gandhi, M. Aronsson, and D. Wu, "An Automated SAR Measurement System for Compliance Testing of Personal Wireless Devices," *IEEE Trans. Electromagn. Compat.*, vol. 41, no. 3, pp. 234–245, Aug. 1999.

[18] M. Okoniewski, "Advances in Computational Dosimetry," 13^{th} *Int. Conf. Microw. Radar and Wireless Comm., Wroclaw, Poland*, pp. 82–93, 2000.

[19] Robert J. Garbacz and Richard H. Turpin, "A Generalized Expansion for Radiated and Scattered Fields," *IEEE Trans. Antennas Propagat.*, vol. 19, no. 3, pp. 348–358, May 1971.

[20] R. F. Harrington, *Field Computation by Moment Methods*, Macmillan, New York, 1968.

[21] C. T. Tai, "The optimum Directivity of uniformly Spaced Broadside Arrays of Dipoles," *IEEE Trans.*, vol. AP-12, pp. 447–454, July 1964.

[22] A. Bloch, R. D. Medhurst, and S. D. Pool, "A New Approach to the Design of Superdirective Aerial Arrays," *Proc. IEE, London*, vol. 100, pp. 1081–1085, 1951.

[23] K. Dackland and B. $K\mathring{a}$gström, "Blocked algorithms and software for reduction of a regular matrix pair to generalized Schur form.," *ACM Trans. Math. Software*, vol. 25, no. 4, pp. 425–454, 1999.

[24] E. E. Osborne, "On preconditioning of matrices," *Journal of the ACM*, , no. 7, pp. 338–345, 1960.

[25] B. N. Parlett and C. Reinsch., "Balancing a matrix for calculation of eigenvalues and eigenvectors," *Numerische Mathematik*, , no. 13, pp. 315–326, 1969.

[26] E. Anderson et al, *LAPACK User's Guide*, Online: http://www.netlib.org/lapack, 1999.

[27] *CONCEPT II*, Software developed in the Technical University Hamburg-Harburg, by the Department of Theoretical Electrical Engineering, version 7.2 Edition, Juli 1997.

[28] R. E. Collin, "Minimum Q of small antennas," *J. Electromagn. Waves Applicat.*, vol. 12, pp. 1369–1393, 1998.

[29] Zinke Brunswig, *Lehrbuch der Hochfrequenztechnik, Erster Band Hochfrequenzfilter, Leitungen, Antennen*, Springer Verlag, 4. Edition, Juli 1990.

[30] Wen Geyi, Perry Jarmuszewski, and Yihong Qi, "The Foster Reactance Theorem for Antennas and Radiation Q," *IEEE Transactions on Antennas and Propagation*, vol. 48, no. 3, pp. 401–408, Mar. 2000.

[31] B. P.; Teukolsky S. A.; Press, W. H.; Flannery and W. T. Vetterling, "Secant Method, False Position Method, and Ridders' Method," *§9.2 in Numerical Recipes in FORTRAN: The Art of Scientific Computing, 2nd ed. Cambridge,England: Cambridge University Press*, pp. 347–352, 1992.

[32] C. Tamgue Famdie, W. L. Schroeder, and Klaus Solbach, "Optimal Antenna Location on Mobile Phones Chassis Based on the Numerical Analysis of Characteristic Modes," *European Microwave Conference, Accepted for Publication, Munich, Germany*, October 2007.

[33] Sophocles J. Orfanidis, *Electromagnetic Waves and Antennas*, Chapter 13, Rutgers University, www.ece.rutgers.edu/ orfanidi/ewa.

[34] Julius Adams Stratton, *Electromagnetic Theory*, Chapter 3, McGraw-Hill Book Compagny, New York and London, 1941.

[35] G. W. Steward, "On the Sensitivity of the eigenvalue problem $\boldsymbol{Ax} = \lambda \boldsymbol{Bx}$," *SIAM J. Numer. Anal.*, , no. 9, pp. 669–686, 1972.